Convective Turbulent Dust Emission: Process, parameterization, and relevance in the Earth system

Inaugural-Dissertation

zur

Erlangung des Doktorgrades

der Mathematisch-Naturwissenschaftlichen Fakultät

der Universität zu Köln

vorgelegt von

Martina Ruth Klose

aus Schlüchtern

Köln, 2014

Berichterstatter/in:	Prof. Dr. Yaping Shao
	Prof. Dr. Ina Tegen
Tag der mündlichen Prüfung:	06. Oktober 2014

Abstract

Convective turbulence generates localized and intermittent surface shear stress and can effectively entrain dust into the atmosphere. This mechanism is referred to as "Convective Turbulent Dust Emission" (CTDE) and is considered as the most important form of direct aerodynamic dust entrainment. CTDE occurs predominantly at weak mean wind conditions, when the buoyancy production of atmospheric turbulence is most pronounced. CTDE is a stochastic process and does not need to involve the saltation of sand-sized grains. This process is so far not included in dust emission schemes and therefore the significance of CTDE for the global dust budget and its impacts on the Earth system remain largely unknown. Here we develop a new parameterization scheme of CTDE. We couple the scheme to the WRF (Weather Research and Forecasting) model in LES (Large-Eddy Simulation) and regional mode with chemistry (WRF/Chem) and investigate the process and its significance for local and regional scale dust emissions. In the parameterization scheme for regional application, the stochastic nature of the process is considered by describing the aerodynamic lifting forces and inter-particle cohesive forces as probability density functions (pdfs). The lifting force was first described as joint pdf of turbulent horizontal and vertical wind velocities. We then determined the lifting force using a new similarity theory for instantaneous momentum flux, obtained from the LES results. The inter-particle cohesive force was described as lognormal distribution with semi-empirical distribution moments. Correction methods for roughness element and moisture effects were suggested. The CTDE scheme was calibrated and validated against field observations recorded in the Horqin Sandy Land area in China and during the Japan-Australia Dust Experiment (JADE) in Australia. The roughness correction is preliminary and could not be tested due to a lack of data for evaluation. Only fractional cover was therefore accounted for in the model simulations. Coupled to the regional model WRF/Chem, the calibrated dust emission scheme was used to assess the long-term regional contribution of CTDE to the overall dust budget for Australia. We showed that a persistent background dust concentration can be generated by CTDE. By comparison with model estimates of global dust emissions, we found that during the study year, the Australian CTDE comprised about 6 - 17 % relative to the yearly global dust emissions. It even exceeded the global model estimates for annual Australian dust emissions, arguably due to favorable conditions in the study year compared to the climatological mean, underrepresentation of regional characteristics, and corresponding underestimation of Australian dust emissions in the global models. Additionally, the disuse of a comprehensive drag partition scheme in our model potentially led to CTDE overestimation. On the local scale, CTDE was observed as being about twice as frequent as saltation bombardment and aggregates disintegration (SADE) and produced more than 80 % of dust emissions compared to that of SADE. Our results suggest that CTDE may be a significant driver of soil nutrient redistribution and air quality at the local scale while contributing to the global impacts of dust on radiation interactions and biogeochemical cycles.

Kurzzusammenfassung

Konvektive Turbulenz kann kurzzeitige und räumlich begrenzte Bodenimpulsflüsse generieren und somit Staub emittieren. Dieser Mechanismus wird als konvektivturbulente Staubemission (engl. "Convective Turbulent Dust Emission", CTDE) bezeichnet und wird als wichtigste Form der direkten aerodynamischen Staubemission angesehen. CTDE tritt vornehmlich unter Schwachwindbedingungen auf, da Konvektion dann den Hauptantrieb der atmosphärischen Turbulenz darstellt. Der CTDE-Prozess ist stochastisch und muss nicht die Saltation von sandgroßen Partikeln beinhalten. Bisher wurde der genannte Prozess nicht in Staubemissionsschemata berücksichtigt. Die Signifikanz von CTDE im globalen Staubhaushalt sowie deren Auswirkungen im System Erde-Atmosphäre sind daher bislang weitgehend unbekannt. In dieser Studie wird ein Parametrisierungsschema des beschriebenen Prozesses entwickelt. Das Schema wird in das WRF ("Weather Research and Forecasting") Modell in LES ("large-eddy simulation") sowie in regionalem Modus mit gekoppelter Chemie (WRF/Chem) implementiert und zur Untersuchung des CTDE-Prozesses und dessen Signifikanz auf lokaler und regionaler Skala genutzt. Die Stochastizität der CTDE wird im regionalen Parametrisierungsschema durch Wahrscheinlichkeitsdichtefunktionen für die aerodynamische Hebungskraft und die Kohäsionskraft beschrieben. Die Hebungskraft wurde zunächst als multivariate Verteilung der horizontalen und vertikalen Windgeschwindigkeiten parametrisiert. Später wurde hierfür eine neue Ähnlichkeitstheorie auf Basis der LES Ergebnisse entwickelt und genutzt. Die Kohäsionskraft wurde als Lognormalverteilung mit semiempirischen Verteilungsmomenten bestimmt. Methoden zur Berücksichtigung der Effekte von Rauigkeitelementen sowie Bodenfeuchte wurden vorgeschlagen. Das CTDE-Schema wurde mit Beobachtungsdaten aus dem Horqin Sandy Land in China sowie des "Japan-Australian Dust Experiment" (JADE) in Australien kalibriert und evaluiert. Die Rauigkeitskorrektur ist vorläufig und konnte aus Mangel an Daten zum Vergleich nicht getestet werden. Für die Simulationen wurde daher nur der Vegetationsanteil berücksichtigt. Das kalibrierte Emissionsschema wurde in das Regionalmodell WRF/Chem implementiert um den langfristigen CTDE-Beitrag zum australischen Staubhaushalt zu untersuchen. Die Modellergebnisse verdeutlichen, dass eine dauerhafte Hintergrundstaubkonzentration durch CTDE generiert werden kann. Während des einjährigen Simulationszeitraums produzierte die australische CTDE Emissionen in Höhe von 6 - 17 % der jährlichen globalen Staubemissionen basierend auf Schätzungen von Globalmodellen. Bezogen auf die geschätzte jährliche Staubemission in Australien übertrafen die CTDE Emissionen diese sogar. Als Gründe hierfür werden günstige Wetterbedingungen im Simulationszeitraum verglichen mit dem klimatologischen Mittel, Unterrepräsentation der regionalen Bedingungen in der groben Modellauflösung der Globalmodelle und eine damit einhergehende Unterschätzung der australischen Staubemissionen vermutet. Zusätzlich hat die bisherige unvollständige Berücksichtigung der Rauigkeitseffekte im CTDE-Schema vermutlich zu einer Überschätzung der CTDE geführt. Die Beobachtungen zeigten, dass CTDE etwa doppelt so häufig auftrat wie andere Emissionsmechanismen (Saltationsbeschuss und Disaggregation)

und im Vergleich dazu 80 % der Emissionen verursachte. Auf Basis unserer Ergebnisse ist es wahrscheinlich, dass CTDE auf lokaler Ebene einen wesentlichen Einfluss auf die Umverteilung von Bodennährstoffen sowie auf die Luftqualität hat, während CTDE auf globaler Ebene für die Wechselwirkung mit atmosphärischer Strahlung und dem biogeochemischen Zyklus besonders relevant ist.

Contents

1 Introduction

Aeolian processes attracted the attention of an increasing number of researchers in a wide area of research disciplines during the recent decades (*Shao et al.*, 2011, and references therein). The term "aeolian" (Aeolus = god of the winds in Greek mythology) has the meaning "relating to or arising from the action of the wind" (`http://www.oxforddictionaries.com`). In a natural environment, aeolian processes primarily refer to the entrainment, transport, and deposition of sand and mineral dust particles and their geomorphological effects. Soil particles can be categorized depending on particle diameter, d, e.g. in the categories of clay ($d \leq 4\,\mu$m), silt ($4\,\mu\text{m} < d \leq 63\,\mu$m), sand ($63\,\mu\text{m} < d < 2\,\text{mm}$), and gravel ($2\,\text{mm} < d < 2\,\text{m}$). Silt and clay are usually referred to as dust (*Shao*, 2008). Due to their smaller sizes, dust aerosols can be easily mixed through the planetary boundary layer by atmospheric turbulence and can be transported by wind over distances of up to several thousand kilometers. In contrast, sand transport is constrained to the local environment, over tens of meters (e.g. *Bagnold*, 1941). Due to its large radius of influence, the effect of dust transport is manifold. In the following paragraphs, the significance of dust in the Earth system at the local, regional, and global scale is highlighted in the context of aeolian sediment emission, transport, and deposition. Descriptions of the physical emission mechanisms are provided and the relative importance of the mechanisms is discussed. In this study, we focus on the direct aerodynamic entrainment of dust particles by convective turbulence. We describe the emission process and present insights from field observations. Finally, we identify current research gaps, leading to the objectives addressed in this study.

The appearance of dust events can be very spectacular, either on a large spatio-temporal scale ($\propto$ 100 - 1000 km and 1 - 10 days) as in case of dust storms (e.g. *McTainsh et al.*, 2005; *Shao et al.*, 2010, 2011) or on small spatio-temporal scales (e.g. $\propto$ 1 - 100 m and $\propto$ 1 - 10 min) as exemplified by dust devils (e.g. *Sinclair*, 1969; *Balme and Greeley*, 2006). Dust can, however, also be entrained into the atmosphere intermittently and thus in less organized patterns. While dust events rarely occur in Europe, they belong to everyday life in Africa, particularly in the Sahel region (e.g. *Klose et al.*, 2010), Asia, and to a lesser degree in Australia and America (*Shao et al.*, 2013). This underlines the importance of dust in the mentioned regions in the context of air quality, land management, and landscape formation at the local and regional scale.

During transport, mineral dusts affect climate on regional and global scale through aerosol-radiation and aerosol-cloud interactions (e.g. *Tegen and Lacis*, 1996; *Rosenfeld et al.*, 2001; *Bangert et al.*, 2012; *Boucher et al.*, 2013, IPCC AR5). The change in radiation is due to scattering and absorption of shortwave radiation and absorption and re-emission of longwave radiation by aerosols (*Sokolik and Toon*, 1996; *Heinold et al.*, 2011). Following *Boucher et al.* (2013, and references therein), the longwave radiative forcing of aerosols at the top of the atmosphere (TOA) is generally positive. In contrast, the shortwave radiative forcing is mostly negative at the surface and the TOA. In the case of strong aerosol absorption, shortwave radiative forcing at the surface can be intensified, while at the TOA radiative forcing can be weakened or even reversed with increasing aerosol absorption and surface albedo (*Tegen et al.*, 2010; *Boucher et al.*, 2013). Dust particles are known to serve as efficient ice nuclei (*Isono*, 1955; *DeMott et al.*, 2003; *Sassen*, 2005; *Field et al.*, 2006; *Hoose et al.*, 2008), but can also act as cloud condensation nuclei (*Kumar et al.*, 2011; *Karydis et al.*, 2011). The results of these aerosol-cloud interactions are, however, very complex, partially compensating, and a separate quantification is nearly impossible (*Boucher et al.*, 2013; *Rosenfeld et al.*, 2014). Although important, the net effect of dust-cloud interactions is thus difficult to determine.

Dust particles carry soil nutrients, minerals, and carbon from their point of origin to the area of deposition. Among the major components of mineral aerosols are tectosilicates (e.g. feldspar, quartz), layer silicates or phyllosilicates (e.g. illite, kaolinite, smectite), carbonates (e.g. calcite, dolomite), gypsum (calcium sulfate), and iron oxides (e.g. hematite, goethite) (*Claquin et al.*, 1999; *Sokolik and Toon*, 1999; *Kandler et al.*, 2009; *Nickovic et al.*, 2012; *Formenti et al.*, 2014). Dust-carried micronutrients, such as iron or phosphorus, the latter being released from soil parent material through weathering (*Okin et al.*, 2004), can act as fertilizers for rain forests, e.g. in the Amazon basin, and for oceanic regions

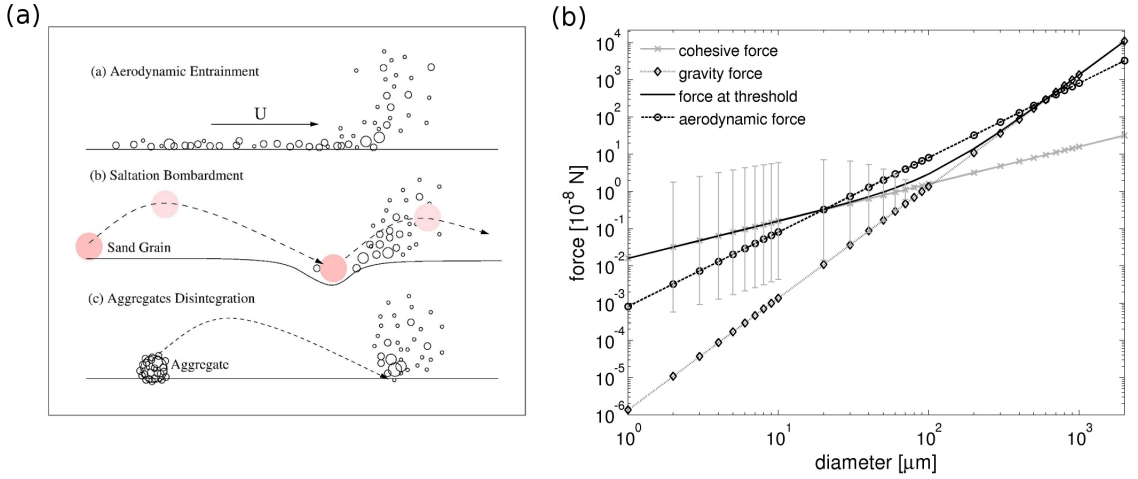

Fig. 1.1.: (a) Illustration of dust emission mechanisms (from *Shao* (2008)); (b) Relative importance of forces relevant for dust emission (modified from *Shao* (2008)). The aerodynamic force is plotted for $u_* = 0.4\,\mathrm{m\,s^{-1}}$. Error bars indicate the standard deviation of the cohesive force as given in *Klose et al.* (2014a, Eq. 8). The stochastic nature of the cohesive force may lead to particle uplift at a lower threshold.

(*Bristow et al.*, 2010) where riverine nutrient inputs are small or nonexistent (*Nickovic et al.*, 2012). Based on oceanic bottle and open water experiments, *Martin and Fitzwater* (1988) and *Martin et al.* (1994) proposed the so-called "iron hypothesis": phytoplankton growth in high-nitrate-low-chlorophyll (HNLC) waters is limited by iron supply with associate constraints on CO_2 uptake and consequences on climate (*Martin*, 1990; *Fung et al.*, 2000; *Jickells et al.*, 2005; *Mahowald et al.*, 2005). *Cropp et al.* (2013) investigated the likelihood of dust-induced phytoplankton blooms in proximity to the Australian continent on a climatological basis by comparing ocean receptivity to dust deposition. However, no unique link between dust supply and marine biological response could be identified until now (*Boyd et al.*, 2010), arguably due to the episodic dust-storm related iron supply mostly considered in contrast to the relatively continuous phytoplankton iron demand.

In contrast to the indirect fertilizing effect, dust can act as a substrate for microorganisms, such as bacteria or fungi, and viruses, which can be transported over long-distances with their carriers (*Griffin*, 2007). In the deposition area, this can have serious effects on human or animal health through penetration into the lung or transport of pathogens and allergens (*Kellogg and Griffin*, 2006; *Derbyshire*, 2007; *Griffin*, 2007) and on ecosystems through deposition of pathogens or chemical contaminants (*Shinn et al.*, 2000; *Garrison et al.*, 2003; *Kellogg and Griffin*, 2006).

The first sequence in the dust cycle (*Shao et al.*, 2011) is the process of dust emis-

sion. Three different mechanisms of dust entrainment have been identified (Figure 1.1a): (1) saltation bombardment, (2) aggregates disintegration, and (3) direct aerodynamic entrainment (*Shao*, 2008). Saltation bombardment (*Shao et al.*, 1993), also known as sand blasting, describes the emission of dust particles through bombardment with sand-sized particles or particle aggregates. When soil aggregates are transported in saltation, the energy exerted on the aggregates as they impact the soil surface can result in their disintegration and the release of fine dust particles. This mechanism is referred to as aggregates disintegration or auto-abrasion (*Shao*, 2008). The direct aerodynamic entrainment of soil particles and aggregates occurs when the air flow alone provides enough energy to overcome the retarding forces acting on a particle, namely gravity force and inter-particle cohesive forces.

All forces relevant for dust emission depend on particle diameter: the aerodynamic force acts on the particle surfaces and is thus $\propto d^2$; the gravity force depends on particle volume and is $\propto d^3$, and the inter-particle cohesive forces, which are composed of Van der Waals forces, electrostatic forces, chemical binding forces, etc., are on average $\propto d$ (*Shao*, 2001, 2008). For small particles ($d < 20\,\mu m$) the cohesive force dominates and for large particles ($d > 500\,\mu m$) the gravity force is the strongest (Figure 1.1b). The particle-size range in between, which is that of potential saltating grains, is most favorable for direct aerodynamic entrainment, which makes the mechanisms (1) and (2) the most efficient for dust-particle uplift, as the impact energy of saltating particles can easily overcome the retarding forces. Due to the high cohesive forces in the dust-particle size range, the mechanism of aerodynamic dust entrainment has been considered negligible for long time. The inter-particle cohesive forces are, however, influenced by many factors, e.g. particle shape, mineral composition, surface roughness, etc., and may vary over orders of magnitude for particles of similar size, suggesting a stochastic behavior of the cohesive forces (*Zimon*, 1982). The standard deviation of the cohesive force as estimated by *Shao* (2008) based on *Zimon*'s data (*Klose et al.*, 2014a, Eq. 8) is illustrated as error bars on the mean cohesive force (*Klose et al.*, 2014a, Eq. 7) in Figure 1.1b. It can be seen that the variation may be such that the inter-particle cohesion is weaker than the aerodynamic lift even for small particle-sizes. This means that for a fraction of particles, the retarding forces are smaller than on average, allowing for direct aerodynamic entrainment.

The previous paragraph shows that in the situation of strong mean wind, the emission mechanisms of saltation bombardment and aggregates disintegration are very efficient and most important. However, strong mean winds occur episodic rather than permanent, leading to temporal gaps between subsequent emission events. The length of these gaps

depends strongly on both atmospheric and land-surface conditions, the latter determining the minimum surface shear stress required for saltation. In contrast, atmospheric turbulence occurs permanently. The turbulence intensity depends on wind shear and buoyancy. In the case of weak mean wind in the absence of saltation, the buoyancy contribution to turbulence production is most important. Convective turbulence generates localized and intermittent strong surface shear stresses that can effectively entrain dust into the atmosphere. We herein assume that a fraction of loose dust particles is always existent and available for uplift. The described mechanism is stochastic and is referred to as "Convective Turbulent Dust Emission" (CTDE) in this study. The magnitude of CTDE is expected to be smaller than that of saltation bombardment, but compared to the episodic occurrence of the latter, CTDE most likely occurs much more frequently, e.g. everyday in arid regions in summer. Hence, the importance of CTDE lies in the generation of a background dust concentration with significant effects on air quality, radiation, and ocean biogeochemistry.

Several studies exist, which provide insights on the importance of CTDE from the perspective of field observations. During the MATADOR (Martian ATmosphere And Dust in the Optical and Radio) field campaign, *Renno et al.* (2004) investigate the dust concentration associated with coherent dry convective plumes and dust devils and report interior dust concentrations of up to $0.1\,\mathrm{g\,m^{-3}}$. *Koch and Renno* (2005) deduce that the former mechanisms contribute to up to 35 % of the global mineral dust budget. This value has been obtained by estimation of the spatio-temporal fractions occupied by dust devils and dry convective plumes and the observations from MATADOR. *Oke et al.* (2007) observed an average of 28 dust devils per day during a 20-day period in a $35\,\mathrm{km^2}$ study area in Australia, suggesting a high importance of this mechanism. From field experiments in the Caspian Depression, *Gledzer et al.* (2009) and *Chkhetiani et al.* (2012) found that fine dust aerosols constitute a substantial part of the total surface layer aerosol at weak winds and strong surface heating. Vertical profiling of convective dust plumes has been done by *Ansmann et al.* (2009) in the framework of the Saharan Mineral Dust Experiment (SAMUM), showing the convective transport of mineral dust. *Allen et al.* (2013) studied the relative importance of different meteorological processes generating dust emissions, such as cold pool outflows, breakdown of nocturnal low-level jets, and convective plumes and vortices. Although the contribution of convective plumes has been found to be only about 2 %, *Allen et al.* categorized 13 % of measured nephelometer scattering as background dust. As convective emissions are not necessarily organized as coherent plumes or dust devils, part of the background aerosol can likely be attributed to CTDE.

In view of the previous paragraphs, a clear gap between dust event observations and their numerical representation becomes obvious. While dust emissions are observed not only at high wind shear, but also under convective turbulent conditions in the absence of strong mean wind, no description of the emission process and no generally applicable parameterization scheme for CTDE exists. Until now, CTDE has widely been considered negligible and has not been included in regional and global atmospheric models. In this study, we hypothesize that direct aerodynamic entrainment is not negligible on long time scales and is most relevant under convective turbulent conditions, i.e. strong surface heating and weak mean wind, where large-eddies develop and generate localized strong aerodynamic lifting forces. In this thesis, we provide an overview on existing dust emission schemes, develop a detailed description of the mechanisms involved in CTDE and propose a comprehensive CTDE parameterization scheme. We use this scheme to assess the importance of CTDE at local and regional scale.

1.1. Overview on dust emission modeling

Most dust emission schemes focus on saltation bombardment. One of the first emission schemes was proposed by *Gillette and Passi* (1988) following an unpublished theory of *Owen* (1987). According to *Owen*'s theory, dust flux "should follow a function of friction velocity that asymptotically approaches the fourth power of friction velocity" (*Gillette and Passi*, 1988):

$$F = C_2 u_*^4 \left(1 - \frac{u_{*t}}{u_*}\right) \tag{1.1}$$

with dust emission flux F, friction velocity u_*, threshold friction velocity u_{*t}, and an empirical dimensional coefficient C_2 [M L^{-6} T^3]. u_{*t} is the minimum friction velocity required for the initiation of saltation and has been assigned to land use type in the latter work.

Shao et al. (1993, 1996) developed a physics-based dust emission scheme based on the kinetic energy transferred to the particles resting on the surface by the saltating grains. Vertical dust emission flux is herein considered proportional to horizontal saltation flux. The scheme is a spectral parameterization, calculating the emission of dust particles of size d_i, emitted by saltators of size d_s as

$$\tilde{F}\left(d_i, d_s\right) = \beta\left(d_i, d_s\right) Q\left(d_s\right) u_{*t}^{-2}\left(d_i\right) \tag{1.2}$$

with Q [μg m^{-1} s^{-1}] being the horizontal saltation flux and β being a bombardment parameter depending on dust and saltator particle-size [m s^{-2}], empirically determined from wind tunnel experiments. u_{*t} represents the drag force and is thus an indicator of the binding energy of the dust particles, as the latter is the product of a length scale and the drag force. The total emission flux is then obtained as combination of bombardments as

$$F = \int_{d_1}^{d_2} \int_{0}^{d_1} \tilde{F}\left(d_i, d_s\right) p\left(d_i\right) p\left(d_s\right) \delta d_i \delta d_s \tag{1.3}$$

where $[0, d_1]$ is the dust-particle size range, $[d_1, d_2]$ that of saltating grains and δ the differential. The consideration of the energy balance during saltation bombardment is also the basis for other dust emission parameterizations, e.g. that of *Alfaro and Gomes* (2001).

The dust emission scheme of *Marticorena and Bergametti* (1995) is semi-empirical and also assumes $F \propto Q$. The proportionality is estimated based on the soil's clay content η_c, as this is considered to be the soil fraction responsible for dust particle abundance. The bulk dust flux is given as

$$F = a_1 \exp\left(a_2 \eta_c - a_3\right) \times Q \tag{1.4}$$

with empirical parameters a_1, a_2, and a_3. *Marticorena and Bergametti* found the expression to work well for $\eta_c < 20\,\%$, as crust effects hamper dust emission at higher clay contents.

Shao (2001, 2004) developed a new approach for spectral dust flux calculation, explicitly accounting for aggregates disintegration in addition to saltation bombardment. The approach is based on the volume removal of the saltating particles:

$$F\left(d_i, d_s\right) = c_y \eta_{fi} \left[(1-\gamma) + \gamma \sigma_p\right] \times (1 + \sigma_m) \times \frac{Qg}{u_*^2}. \tag{1.5}$$

The term in squared brackets describes aggregates disintegration with free dust to aggregated dust ratio σ_p. The term in round brackets represents saltation bombardment with bombardment efficiency σ_m and the last term describes saltation. c_y is a constant, η_{fi} is the mass fraction of dust with diameter d_i in fully dispersed particle-size analysis, and γ is a fixed function of friction velocity, representing the aggregation binding strength. The bombardment efficiency, σ_m, is the ratio of ejected to impacted mass. As shown in Equation (1.5), dust flux is proportional to saltation flux, but the proportionality depends

on soil texture and soil plastic pressure. *Shao et al.* (2011) have shown that the scheme is not sensitive to γ and can be simplified as

$$F\left(d_i, d_s\right) = c_y \eta_{mi} \frac{Qg}{u_*^2} \tag{1.6}$$

with η_{mi} being the dust mass fraction of size d_i in minimally dispersed analysis.

Kok (2011) and *Kok et al.* (2014) made use of an analogy between the saltation bombardment emission process and the fragmentation theory of brittle material such as glass. They parameterize dust-particle release caused by the fragmentation of soil aggregates due to the bombardment with sand-sized grains. After adaptation of the indivisible constituent size x_0 and the side crack propagation length λ to dust-particle aggregates, *Kok* (2011) obtain equations for number- and volume-size distributions of emitted dust. *Kok et al.* (2014) augmented this approach with theories for the saltation process and obtained for vertical dust emission flux

$$F = C f_{\text{bare}} f_{\text{clay}} \frac{\rho\left(u_*^2 - u_{*t}^2\right)}{u_{*st}} \left(\frac{u_*}{u_{*t}}\right)^{C_\alpha \frac{u_{*st} - u_{*st0}}{u_{*st0}}} \tag{1.7}$$

where C is a coefficient of soil erosion susceptibility to saltation bombardment, f_{bare} the bare surface fraction, f_{frag} the fraction of saltator impacts resulting in fragmentation, ρ air density, u_{*st} the standardized threshold friction velocity normalized to $\rho_0 = 1.225\,\text{kg}\,\text{m}^{-3}$, u_{*ts0} that of an optimally erodible soil, and C_α a dimensionless coefficient. Here, u_{*t} is defined as the minimum u_* for which erosion occurs at a bare soil.

As discussed previously, aerodynamic dust entrainment has been widely neglected until now, because the inter-particle cohesive forces are known to be large on average compared to the aerodynamic forces. Only few studies exist, which aim to numerically estimate the latter process. *Loosmore and Hunt* (2000) conducted wind tunnel experiments with a PM10 dust surface (dust particles with $d < 10\,\mu\text{m}$) to investigate dust flux occurrence in the absence of saltation. The authors measured dust concentration for idealized flow conditions at u_* ranging between about 0.6 and $1.4\,\text{m}\,\text{s}^{-1}$. *Loosmore and Hunt* (2000) found that there exists a continuous dust flux even below the visual threshold (i.e. u_{*t}), suggesting the latter may not be "an appropriate parameter for dust release". From their experimental results, they estimate the aerodynamic dust flux to be

$$F = 3.6 u_*^3. \tag{1.8}$$

Ito et al. (2010) implemented this formulation into their large-eddy simulation (LES)

model. They conducted simulations for a convective mixed layer and showed that thermal convection can provide conditions favorable for direct dust entrainment in the absence of strong mean winds. *Descamps et al.* (2005) made use of probability density functions (pdfs) for aerodynamic and cohesive forces in their pavement model and aim to predict the temporal evolution of surface particle-size distribution.

Chkhetiani et al. (2012) relate the dust mass concentration in the absence of saltation to the temperature drop, δT, at the surface as

$$\Delta C \propto (\delta T)^{\alpha} \tag{1.9}$$

with dust emission flux

$$F = -\kappa_c \frac{|\Delta C|}{\delta z}. \tag{1.10}$$

ΔC is the difference between dust concentration at the surface and the background aerosol concentration, κ_c is the kinematic diffusion of dust, and δz is a height difference. α is a coefficient which was found to range between 1/2 - 2/3 for small and moderate u_* and about $-1/2$ for large u_*. Based on these dependencies, they obtain $F \propto u_*^3$, consistent with *Loosmore and Hunt* (2000) and the early work of *Bagnold* (1941), originally developed for saltation.

This section shows that most dust emission schemes consider only saltation bombardment (*Gillette and Passi*, 1988; *Shao et al.*, 1993, 1996; *Marticorena and Bergametti*, 1995; *Kok*, 2011; *Kok et al.*, 2014). Aggregates disintegration is explicitly accounted for only in a few emission parameterizations (*Shao*, 2001, 2004). Although the schemes work well for the prediction of strong dust events such as dust storms (e.g. *Cavazos et al.*, 2009; *Shao et al.*, 2010), they cannot be used for CTDE due to the different underlying mechanism. Numerical estimates of CTDE exist, but they are subject to several constraints. The equation of (*Loosmore and Hunt*, 2000) is purely empirical and thus specific to the experimental setup used. In the approach of *Chkhetiani et al.* (2012), the change in aerosol mass concentration is deduced from a parameterization of the turbulent flow without describing the emission process itself. Particle uplift due to atmospheric turbulence is determined in the pavement model of *Descamps et al.* (2005). However, only the number of emitted particles is estimated based on an uplift criterion rather than the dust emission flux based on the equation of particle motion. It is thus not currently possible to generally apply the mentioned schemes in regional atmospheric models.

1.2. Objectives and thesis outline

The previous discussions show that dust emission in the absence of saltation, i.e. CTDE, is poorly understood. Accordingly, no numerical tool for the prediction of CTDE in regional atmospheric models is available. Although site-based observations confirm the existence of CTDE, significance assessments remain rather uncertain leading to negligence of the process in most studies. The aim of this study is to investigate the mechanism of CTDE and to provide a clear definition of the processes involved. Further, a comprehensive parameterization scheme for prediction of the CTDE mechanism is to be developed. It is intended that the parameterization will be generally applicable in regional atmospheric models. Knowing the emission process, the relevance of CTDE in the Earth system is to be investigated. The research objectives of this thesis can be summarized as:

1. Investigation and definition of the CTDE mechanism;
2. Development of a comprehensive CTDE parameterization scheme;
3. Evaluation of the CTDE scheme based on field observations;
4. Implementation of the scheme into a regional atmospheric model; and
5. Assessment of the CTDE relevance in the Earth system.

This thesis consists of an introductory chapter, four publications, a chapter on the contribution of CTDE to the regional dust budget, and conclusions. In the five main chapters (Chapters 2 - 6), the CTDE mechanism is detailed, the development steps of a CTDE scheme are described, and results from field observations and a regional modeling study on CTDE are presented as outlined in the following and visualized in Figure 1.2.

In Chapter 2 (*Klose and Shao*, 2012), the process of CTDE is described in detail for the first time and first developments on a stochastic CTDE parameterization scheme are introduced. The scheme computes dust emission based on the balance of inter-particle cohesive and lifting forces. Both forces are described by means of probability distributions. The CTDE scheme is implemented into the Weather Research and Forecasting model with chemistry (WRF/Chem) and applied to the Taklimakan desert in China. Simulation results of a three-day model run are shown and compared to lidar observations. A first estimate on the CTDE based dust budget in the simulation domain is presented and uncertainties arising from inaccuracies in the representation of inter-particle cohesive forces are quantified.

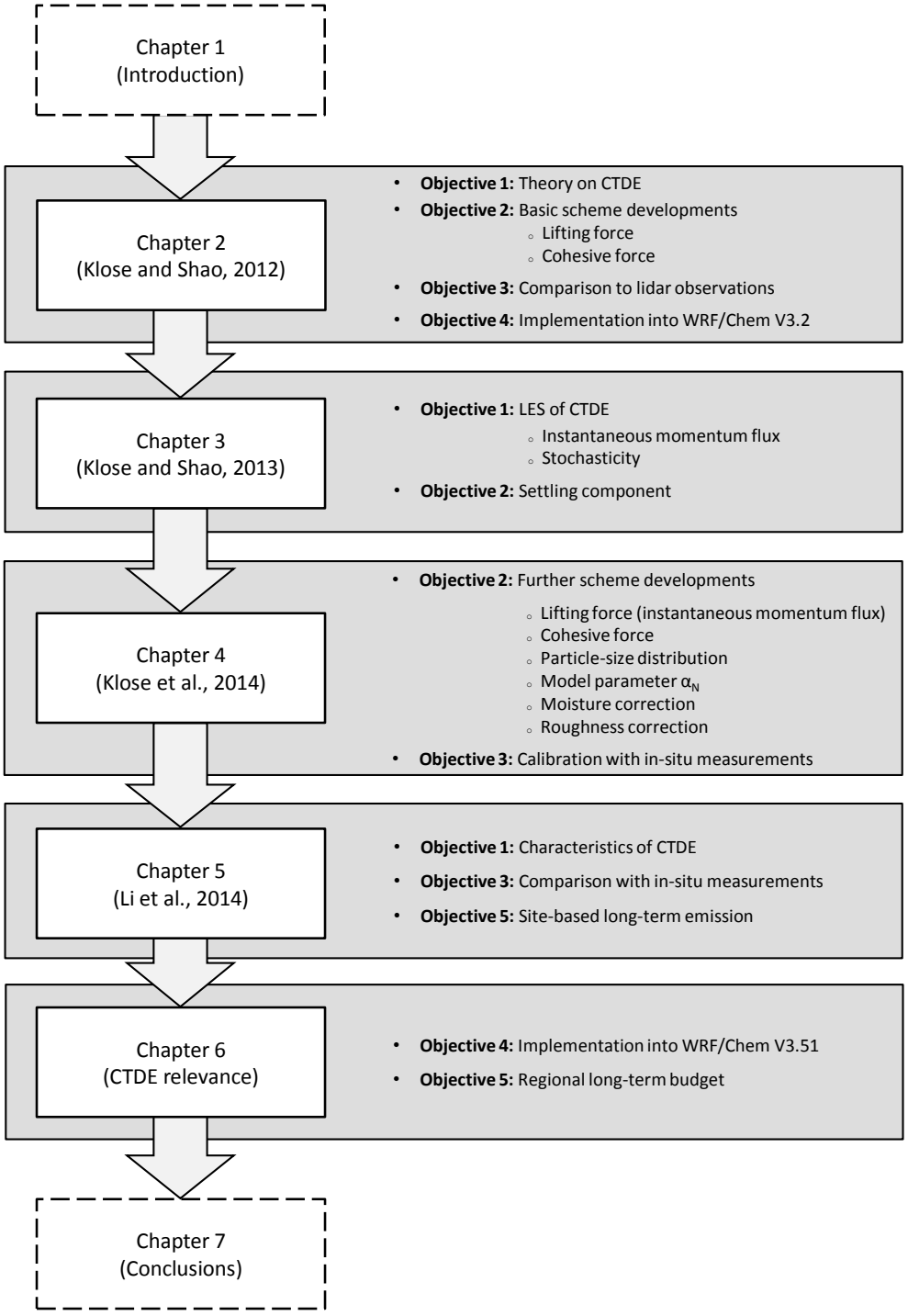

Fig. 1.2.: Flowchart visualizing the research objectives listed in Section 1.2 as addressed in the framework of this thesis.

In addition to cohesive and lifting forces, the gravity force is retained in the equation of particle motion used for derivation of the CTDE equation in Chapter 3 (*Klose and Shao*, 2013). This leads to an additional settling component in the CTDE equation. The mechanism of CTDE is illustrated and the term "Convective Turbulent Dust Emission" is first introduced and established. To investigate the dynamics of CTDE, the parameterization is included into the WRF-LES model. In the WRF-LES model with dust (WRF-LES/D), no parameterization for the lifting force is needed, as the atmospheric flow is mostly resolved due to the high model resolution. This enables the investigation of the lifting force arising from atmospheric turbulence. The lifting force is based on the instantaneous momentum flux exerted on the surface by large eddies. The stochastic behavior of both instantaneous momentum flux and CTDE is shown and the hypothesis that large-eddies can lead to dust emission, which is the basis of the CTDE mechanism, is tested.

Further developments of the CTDE parameterization scheme are proposed in Chapter 4 (*Klose et al.*, 2014a). These include the consideration of the size-dependence of an important model parameter, the change from a purely empirical to partly theory-based representation of the cohesive force, the use of area particle-size distribution (psd) instead of mass psd, and most important, the development of a similarity theory for instantaneous momentum flux based on the LES results of Chapter 3. Additionally, methods to account for soil-moisture and roughness effects are suggested. The new model version is tested and calibrated with field observations from China and Australia.

In Chapter 5 (*Li et al.*, 2014), field measurements taken during one year in the Horqin Sandy Land area in China were analyzed. During this time period, dust concentration, saltation activity, as well as meteorological parameters have been observed. The diurnal and seasonal variation of CTDE is studied and the characteristics are specified from the perspective of field observations. The occurrence frequency of CTDE is investigated and the long-term contribution is estimated and compared to that of saltation bombardment and aggregates disintegration (SADE).

In the framework of the regional model WRF/Chem, the newly developed dust emission parameterization is applied for a long-term regional CTDE budget study for Australia (Chapter 6). Based on synoptic station data, a one-year time period with a high peak frequency of convective dust events but low dust storm frequency is selected as simulation period. Model input quantities such as vegetation cover, dust source area, and particle-size distributions are specified for the time period and area under investigation. The simulation results are analyzed with regard to the seasonal variation of dust emission, atmospheric dust load, and deposition. A regional budget estimate is provided and the relevance of

CTDE is highlighted.

The final chapter (Chapter 7) synthesizes the results with regard to the objectives of this thesis. The research outcomes are discussed and priorities for future research are identified.

2 Stochastic parameterization of dust emission

Reference:

Klose, M., and Y. Shao (2012), Stochastic parameterization of dust emission and application to convective atmospheric conditions, *Atmos. Chem. Phys.*, *12*(12), 7309–7320, doi: 10.5194/acp-12-7309-2012

Atmos. Chem. Phys., 12, 7309–7320, 2012
www.atmos-chem-phys.net/12/7309/2012/
doi:10.5194/acp-12-7309-2012

Atmospheric Chemistry and Physics

Stochastic parameterization of dust emission and application to convective atmospheric conditions

M. Klose and Y. Shao

Institute for Geophysics and Meteorology, University of Cologne, Kerpener Str. 13, 50937 Cologne, Germany

Correspondence to: M. Klose (mklose@uni-koeln.de)

Received: 7 December 2011 – Published in Atmos. Chem. Phys. Discuss.: 30 January 2012
Revised: 22 May 2012 – Accepted: 29 July 2012 – Published: 16 August 2012

Abstract. We develop a parameterization scheme of convective dust emission for regional and global atmospheric models. Convective dust emission occurs in the absence of saltation as large eddies intermittently produce strong shear stresses on the surface and entrain dust particles into the air. This dust emission mechanism has not been included in the traditional dust models. The scheme presented in this study is a new approach which takes account of the stochastic nature of convective dust emission. It consists of the statistical representations of soil particle size, inter-particle cohesion, and instantaneous surface shear stress. A method of determining the probability density function of the latter quantity is proposed. Dust emission is then estimated from the overlap of the probability density functions of the aerodynamic lifting and inter-particle cohesive forces. The new scheme is implemented into the WRF/Chem model and applied to dust modeling in the Taklimakan Desert. A comparison with lidar data shows that the model can reproduce the main features of the dust patterns and their diurnal variations. For the case studied, convective dust emission is typically several $\mu g\,m^{-2}\,s^{-1}$ and at times up to $50\,\mu g\,m^{-2}\,s^{-1}$.

1 Introduction

The existing dust emission schemes used in regional and global atmospheric models are mainly concerned with the parameterization of dust emission caused by saltation bombardment (e.g. Marticorena and Bergametti, 1995) and aggregates disintegration (e.g. Shao, 2004). These schemes are fairly effective for the simulation of dust emission during strong dust events (e.g. Shao et al., 2010). However, they are not designed for quantifying dust emission under weak wind conditions, which is generated by intermittent turbulence rather than by the mean wind shear and the associated saltation of sand-sized grains. As pointed out in previous studies (Marticorena et al., 1997; Shao et al., 1993), the intensity of dust emission due to direct aerodynamic lifting is much weaker than that due to saltation bombardment and aggregates disintegration, and can therefore be neglected in modeling strong dust events (e.g. dust storms). However, while the intensity of aerodynamic dust emission is weak in general, it may occur frequently, e.g. on daily basis in desert areas. In contrast, strong dust events occur much less frequently, maybe a few times a month during the peak dust season. Therefore, aerodynamic dust emission may constitute a major contributor to the regional and global dust budgets on seasonal, annual or longer time scales. For example, Koch and Renno (2005) reported that convective plumes and vortices contribute to about 35 % of the global budget of mineral dust. Several recent review papers also highlighted the potential importance of micro-scale dust emission (Shao et al., 2011; Knippertz and Todd, 2012).

Aerodynamic dust emission by turbulence is most obvious under convective (atmospheric boundary layer) conditions, as exemplified by dust devils in desert in summer. In this study, we call aerodynamic dust emission due to convective turbulence convective dust emission. A few studies on convective dust emission have been carried out in recent years. Ansmann et al. (2008) investigated the vertical structure of convective dust plumes using lidar observations in Morocco during the Saharan Mineral Dust Experiment (SAMUM). Heintzenberg (2008) and Loosmore and Hunt (2000) carried out wind-tunnel experiments and found that dust emission also occurs in the absence of saltation. Gledzer et al. (2009) considered particles significantly smaller than the thickness

of the viscous sublayer and estimated the mass concentration of dispersed fine particles in the viscous thermal boundary layer based on field measurements in the desertified areas near the Caspian Sea. The driving parameters in their approach are friction velocity and temperature drop near the surface. Ito et al. (2010) carried out a large-eddy simulation (LES) to estimate convective dust emission. They considered a particle size range from 1 to 10 µm and computed the dust fluxes according to Loosmore and Hunt (2000). Their simulations show that dust concentration in the mixed layer linearly increases with surface heat flux.

The first aim of this study is to develop a scheme for the parameterization of convective dust emission. An important feature of the scheme is a statistical description of the stochastic variables involved in the process. This is a new approach to dust emission modeling in contrast to the conventional dust emission schemes. The theory for the new scheme is described in Sect. 2. The second aim of the study is to develop the capacity of assessing the contribution of convective dust emission to regional and global dust budgets. To this end, a technique is proposed to implement the new scheme in the framework of the WRF/Chem model. An atmospheric model (e.g. regional) has a typical grid size of a few to a few tens of kilometers. For a given model grid cell, the joint probability density function (joint pdf) of the horizontal and vertical velocity components, i.e. the shear stress, is generated based on the pdfs for the individual components following Manomaiphiboon and Russell (2003). The WRF/Chem model with the new scheme is then implemented for the simulation of a convective dust event in the Taklimakan Desert. The model results are compared with the lidar data collected at Aksu.

2 Convective dust emission

The main mechanisms for dust emission are aerodynamic entrainment, saltation bombardment, and aggregates disintegration (Shao, 2008). In case of strong winds, saltation bombardment and aggregates disintegration are the dominant mechanisms in comparison to aerodynamic entrainment. In the context of dust emission, strong winds refer to the situations when $u_* > u_{*t}$, where u_* is friction velocity and u_{*t} is threshold friction velocity for saltation. If wind is too weak to activate saltation ($u_* < u_{*t}$), then aerodynamic entrainment becomes the prevalent mechanism for dust emission. Convective dust emission is the most important form of aerodynamic entrainment and is thus the focus of the new dust scheme. The applicability of our approach is, however, not limited to convective conditions. It can be easily extended to other turbulent conditions, e.g. shear generated turbulence, by modifying the momentum transport parameterization described in Sect. 4.1.

Convective turbulence occurs in regions of strong surface heating, such as desert areas in summer. A super-adiabatic temperature gradient commonly exists in the atmosphere near the surface, which forces the development of thermals and generates strong vertical velocity fluctuations.

Let us consider a unit area covered with dust particles of different sizes. A force τ is exerted by turbulence on the unit area ($[\tau] = \mathrm{N\,m^{-2}} = \mathrm{Pa}$). If the force is evenly distributed, then the force exerted on a particle with a cross-section of a is

$$f_d = |\tau| \cdot a = |\tau| \cdot \frac{\pi d^2}{4}. \tag{1}$$

The fraction η_i of particles of size d_i in a given size interval δd_i is

$$\eta_i = p\,(d_i)\,\delta d_i. \tag{2}$$

Here, $p\,(d_i)$ denotes the particle size distribution function (psd). Therefore, the force exerted on all particles in this size interval is given by

$$f\,(d_i) = |\tau| \cdot a\,(d_i) \cdot \eta_i. \tag{3}$$

The quantity τ is the instantaneous vertical flux of horizontal momentum given by

$$|\tau| = \rho\sqrt{(u'w')^2 + (v'w')^2} \tag{4}$$

with air density ρ. Note that the current values of $u'w'$ and $v'w'$ are used instead of the mean values $\overline{u'w'}$ and $\overline{v'w'}$ of the Reynolds shear stress. As detailed in Sect. 3, τ is parameterized by means of a joint pdf of the horizontal and vertical wind components.

Dust emission can be expressed as the number flux n_d of dust particles of size d multiplied by the particle mass m_p:

$$F = n_\mathrm{d} \cdot m_\mathrm{p} = N_\mathrm{d} w_\mathrm{p} \cdot m_\mathrm{p} \tag{5}$$

where N_d is the particle number concentration and w_p the particle vertical velocity which obeys the equation of particle motion, namely,

$$\frac{\mathrm{d}w_\mathrm{p}}{\mathrm{d}t} = \underbrace{-\frac{1}{T_\mathrm{p}}\left(w_\mathrm{p} - w_\mathrm{a}\right)}_{\mathrm{I}} \underbrace{-\,g}_{\mathrm{II}} \underbrace{+\frac{(f - F_i)}{m_\mathrm{p}}}_{\mathrm{III}}. \tag{6}$$

The first term contains the particle response time T_p and the vertical component $(w_\mathrm{p} - w_\mathrm{a})$ of the particle-to-air relative velocity $\boldsymbol{U}_\mathrm{r}$, with w_a being the vertical velocity of the air. In general, T_p can be expressed as

$$T_\mathrm{p} = \frac{4}{3}\frac{d}{C_\mathrm{d} U_\mathrm{r}}\frac{\rho_\mathrm{p}}{\rho} \tag{7}$$

with aerodynamic drag coefficient C_d, and U_r being the magnitude of $\boldsymbol{U}_\mathrm{r}$ (Shao, 2008). The particle density ρ_p is approximately $2560\,\mathrm{kg\,m^{-3}}$. Term I in Eq. (6) describes the behavior of a particle in air and is important as soon as the particle is

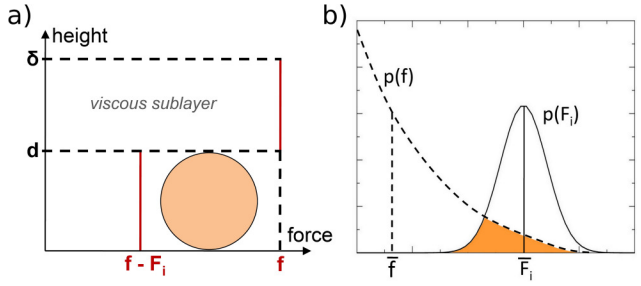

Fig. 1. (a) Illustration of the lifting force affecting a particle in the viscous sublayer; **(b)** illustration of the probabilistic distributions used for the description of the cohesive and lifting forces.

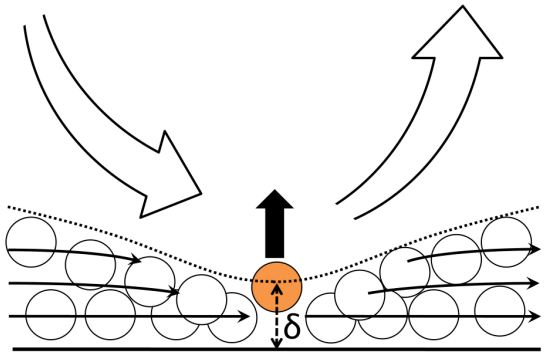

Fig. 2. Illustration of a large eddy above the viscous sublayer (flow indicated by arrows), which exerts a force on the particles, reduces the depth of the viscous sublayer δ (dotted line) and increases the particle number concentration.

lifted from the surface. Term II reflects the particle acceleration due to gravity. Term III is the most important term concerning the emission process. The force exerted on the particle by wind as described in Eq. (3) is f and the cohesive force F_i. F_i is only active up to a height of the order of particle diameter and is then zero (Fig. 1a). In our scheme, both f and F_i are stochastic quantities which obey certain probability distributions. Therefore, dust emission is proportional to the overlap of the two distributions (Fig. 1b).

A dust particle can be considered to be emitted from the surface if it passes through the viscous sublayer adjacent to the surface. Therefore, Eq. (6) is integrated over the depth of the laminar layer to determine the vertical velocity of the dust particle motion:

$$w_\mathrm{p} = -\frac{w_\mathrm{t}}{2} + \frac{(f - F_i)}{m_\mathrm{p}} \frac{T_\mathrm{p} d}{2\delta} + \frac{f}{m_\mathrm{p}} \frac{T_\mathrm{p}(\delta - d)}{2\delta} \tag{8}$$

with particle terminal velocity $w_\mathrm{t} = gT_\mathrm{p}$. The effective turbulent flux τ (sum of molecular and turbulent fluxes) is approximately constant with height in the surface layer (Stull, 1988). In the viscous sublayer, τ obeys the Newtonian law:

$$\tau = \nu\rho \frac{dU}{dz} \tag{9}$$

with ν being the kinematic viscosity. Suppose $U(z = 0) = 0$. Then, an integration of Eq. (9) yields

$$\frac{U}{u_*} = \frac{u_*}{\nu} z. \tag{10}$$

Suppose the instantaneous friction velocity is $u_* = \sqrt{\tau/\rho}$ and the transition between the laminar and turbulent flows (which defines the top of the viscous sublayer) starts at a friction Reynolds number of $u_* z/\nu = 5$ (Schlichting et al., 2003). Then, the thickness δ of the viscous sublayer can be estimated as

$$\delta = \frac{5\nu}{u*}. \tag{11}$$

The first term in Eq. (8) represents dust deposition and therefore does not have to be included in the dust emission scheme. The particle vertical velocity w_p in Eq. (5) can now be substituted by Eq. (8). As illustrated in Fig. 2, the particle number concentration N_d must be inversely proportional to the depth of the laminar layer, namely, $N_\mathrm{d} = \alpha_N/\delta$ with α_N in m^{-2} being the proportionality parameter. It follows that the dust emission flux can be expressed as

$$F_d = \begin{cases} \alpha_N \frac{T_\mathrm{p}}{2\delta} \left(f - F_i \frac{d}{\delta}\right) & \text{for } f > F_i \text{ and } \delta > d, \\ 0 & \text{else.} \end{cases} \tag{12}$$

The parameter α_N is an unknown empirical parameter to be determined by comparison of the scheme with observations. Finally, the total convective dust emission for all particles of a given particle size interval is given by

$$F(d_i) = \eta_i \cdot \int_0^\infty \left(\int_0^f \alpha_N \frac{T_\mathrm{p}}{2\delta} \left(f - F_i \frac{d}{\delta}\right) p(F_i)\,\mathrm{d}F_i \right) p(\tau)\,\mathrm{d}\tau. \tag{13}$$

The innermost integration accounts for the stochastic behavior of the cohesive force F_i (see Sect. 3.1) and the integration over the instantaneous shear stress τ accounts for the stochastic behavior of the lifting force f, which is related to τ by Eq. (3). Thus, the two integrals multiplied by the number of particles of size d_i describe the amount of dust emitted for this particle size (see also Fig. 1b). Finally, the integration over particle diameter d_i of $F(d_i)$ multiplied by the psd yields the total dust emission for all particle sizes. The principal mechanisms of convective dust emission as parameterized by Eq. (13) are summarized in Fig. 2.

3 Parameterization

As shown in the previous section, the parameterizations for both the cohesive and lifting forces are necessary, and the parent-soil psd must be specified as an input quantity. As our main concern is convective dust emission under weak mean wind conditions, minimally-disturbed psds are used. These

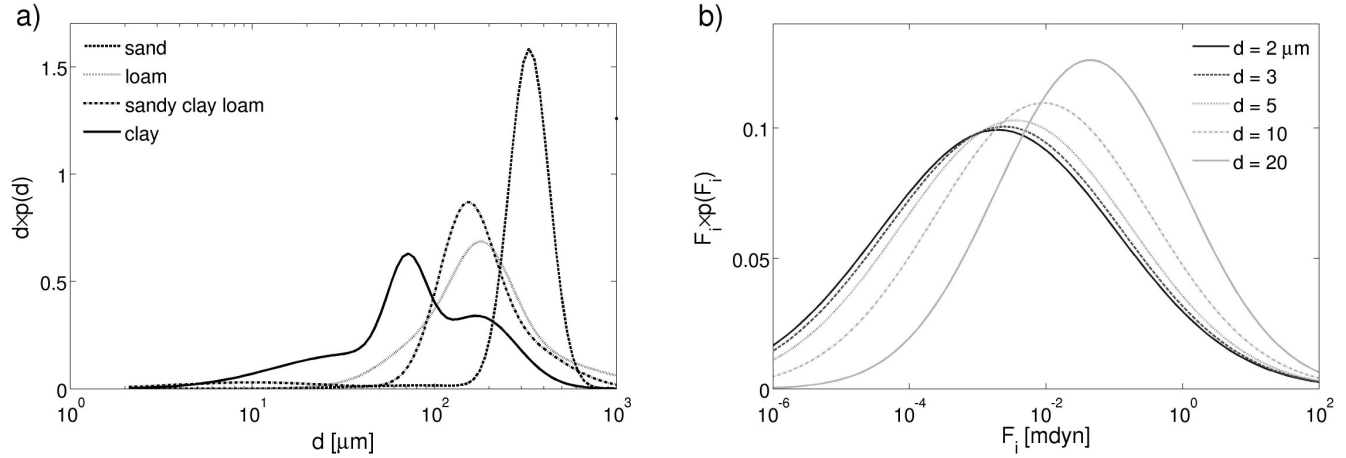

Fig. 3. (a) Parameterizations of particle size distribution composed from four log-normal distributions to fit experimental data. The results for the four soil types used in this study are shown; **(b)** probabilistic distribution of the cohesive force for particle diameters of 2, 3, 5, 10, and 20 μm plotted in $F_i \cdot p(F_i)$. The distributions are calculated using Eq. (14).

are approximations to the parent soil psd seen by turbulence, as they are obtained with the minimal mechanical and chemical disturbances to the soil samples. In contrast, fully-disturbed psds are obtained by applying strong mechanical and chemical forces to disaggregate the soil particles, which rarely occurs in real dust emission processes (Shao, 2008). The use of minimally-disturbed psd is thus more appropriate for our scheme. In this study, the minimally-disturbed psds for the parent soils are approximated as the sum of four log-normal distributions as described by Shao (2001). The U.S. Department of Agriculture's (USDA's) soil classification distinguishes 12 soil texture classes based on the percentages of sand, silt, and clay. Due to the lack of psd measurements, these classes are regrouped into four classes in the model, namely, sand, loam, sandy clay loam, and clay. For these soils, the psds are shown in Fig. 3a.

3.1 Cohesive force

The particle retarding force includes the cohesive force and the gravity force. The cohesive force is mainly composed of Van der Waals-forces, electrostatic forces, capillary forces, and chemical binding forces (Shao, 2008). For small particles, cohesive force dominates, while for large particles gravity force dominates. Factors such as particle shape, mineral composition, surface roughness, etc., profoundly affect the inter-particle cohesion and consequently, the cohesive force may differ over orders of magnitude for particles in the same size range. In general, the factors contributing to the inter-particle cohesion are so various that the cohesive force can be best treated as a stochastic variable with certain probability distributions. Based on the data of Zimon (1982), the retarding force appears to obey a log-normal distribution. In the scheme developed here, the pdf of F_i is given by

$$p(F_i) = \frac{1}{F_i \sqrt{2\pi}\sigma_{F_i}} \exp\left(-\frac{\left(\ln F_i - \ln \bar{F}_i\right)^2}{2\sigma_{F_i}^2}\right), \quad (14)$$

where the mean value $\bar{F}_i$ and the geometric standard deviation σ_{F_i} ($\bar{F}_i$ and σ_{F_i} in mdyn $= 10^{-8}$ N, and d in μm) are

$$\bar{F}_i(d) = \left[10\exp\left(4.3569 - 0.2183d + 0.0018d^2\right)\right]^{-1} \quad (15)$$

$$\sigma_{F_i}(d) = 4.1095 - 0.04761d. \quad (16)$$

The coefficients herein are obtained by fitting the pdf to the data of Zimon (1982). The results for six particle sizes between 1 and 20 μm are shown in Fig. 3b. As seen, $\bar{F}_i$ increases with particle diameter and the range of F_i variation increases with decreasing particle size due to the greater dominance of the stochastic cohesive force and the reduced importance of gravity force. We emphasize, however, the above described parameterization of F_i is only provisional. More data is required for improved treatment of F_i and tests on the model sensitivity to this treatment is necessary. Nevertheless, it is sufficient to use the data to illustrate our idea of stochastic dust modeling.

3.2 Lifting force

To parameterize the shear stress generated by convective turbulence, the joint pdfs of (u', w') and (v', w') are required. These are determined by use of the similarity theory. Since the velocity fluctuations u' and v' behave similarly, they have equal variances which can be combined to $\sigma_{u_h}^2 = \sqrt{2}\sigma_u^2$. In the remainder of this paper, u denotes the total horizontal wind component. The (u', w') joint pdf can be constructed on the basis of the pdfs of u' and w'. The required statistical

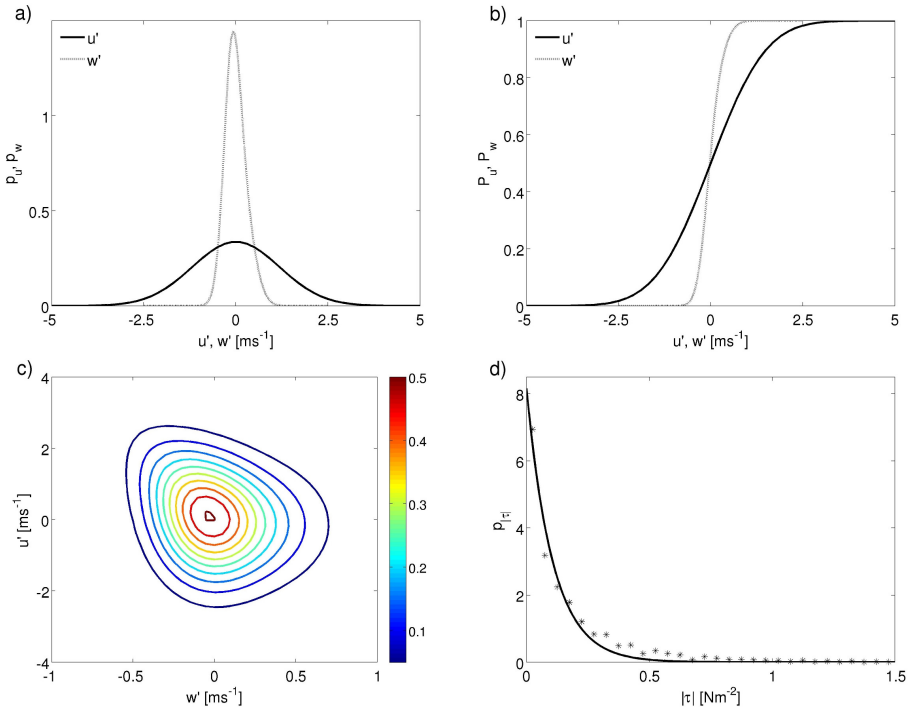

Fig. 4. Procedure of determining the pdf of τ, p_τ, by using the pdfs of u' and w', p_u and p_w **(a)**, their cdfs P_u and P_w **(b)**, as well as their joint pdf **(c)**. Shown in **(d)** is the pdf of $|\tau|$, $p_{|\tau|}$.

moments, such as variances and skewnesses can be estimated from the mixed layer similarity theory. The appropriate scaling velocity and length are respectively the convective velocity scale w_* and planetary boundary layer (PBL) depth z_i. According to the similarity laws (Kaimal and Finnigan, 1994), the variances of u' and w' are given by

$$\frac{\sigma_u^2}{w_*^2} = \frac{\sigma_v^2}{w_*^2} \approx 0.35 \tag{17}$$

$$\frac{\sigma_w^2}{w_*^2} = 1.8\left(\frac{z}{z_i}\right)^{2/3}\left(1-0.8\frac{z}{z_i}\right)^2 \tag{18}$$

while the skewness for w', $\gamma = \overline{w'^3}/\sigma_w^3$, is defined by

$$\frac{\overline{w'^3}}{w_*^3} = 1.0\left(\frac{z}{z_i}\right)\left(1-0.7\frac{z}{z_i}\right)^3. \tag{19}$$

The mean value of the momentum transfer, $\tau_R = -\rho\overline{u'w'}$, is also obtained from the similarity theory, i.e.

$$\frac{-\overline{u'w'}}{w_*^2} = \left(\frac{k}{|z_i/L|}\right)^{2/3}\left(1-\frac{z}{z_i}\right)^{3/2-q} \tag{20}$$

with

$$q = \frac{1}{2}\frac{|z_i/L|}{(1+|z_i/L|)} \tag{21}$$

where $\overline{u'w'}$ represents the covariance σ_{uw}^2 between u' and w'. L is the Obukhov length.

Following Manomaiphiboon and Russell (2003), the pdf of τ, and thus that of f, is obtained in three steps. First, the pdfs of u' and w', p_u and p_w, and the corresponding cumulative distribution functions (cdfs), P_u and P_w, are computed. Second, the (u', w') joint pdf, p_j, is computed using the above pdfs and cdfs. Last, the pdf of τ, p_τ, is obtained from p_j with $\tau = -\rho u'w'$. Note that since different combinations of u' and w' can yield the same τ, p_τ is the sum of p_j for the same $u'w'$ product as follows

$$p_\tau(\tau_i)\,\mathrm{d}\tau = \sum_{\substack{u',w' \\ -\rho u'w'=\tau_i}} p_j\left(u', w'\right)\mathrm{d}u'\mathrm{d}w'. \tag{22}$$

To determine p_u, P_u, etc., the method proposed by Manomaiphiboon and Russell (2003) is used. While p_u is Gaussian, p_w is approximated with a Bi-Gaussian pdf as convective turbulence exhibits a negative skewness.

Manomaiphiboon and Russell (2003) parameterized the joint pdf of u' and w' according to the technique of Koehler and Symanowski (1995). The essence of this technique is to derive the joint pdf from the predefined marginal distributions. The shapes of the marginal distributions are conserved during the transformation to a joint pdf.

Figure 4 shows the process of determining p_τ step by step. The mean value of τ, τ_R, as well as the variances of u' and w', estimated by means of the mixed layer similarity theory, are herein used to match the parameterized pdf of τ to the environmental conditions given by the model simulations.

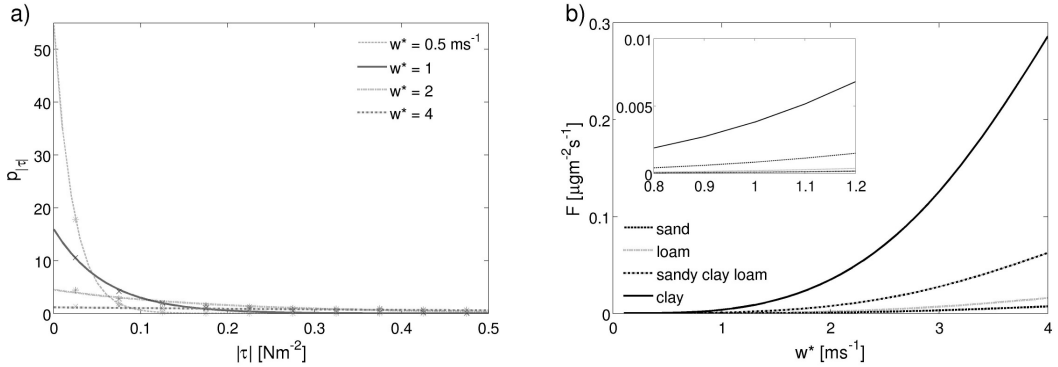

Fig. 5. (a) Sensitivity of $p_{|\tau|}$ to w_*; **(b)** Sensitivity of dust emission flux F to w_* for different soil types. The insert shows the F and w_* relationship for $w_* \approx 1\,\mathrm{m\,s^{-1}}$.

The above described dust emission scheme and the parameterizations have been integrated in the WRF model (Advanced Research version) (Wang et al., 2009) with chemistry (WRF/Chem, Grell et al., 2005). The GOCART (Georgia Tech/Goddard Global Ozone Chemistry Aerosol Radiation Transport) aerosol scheme (Chin et al., 2000) is used as the basis for the implementation of our scheme. The convective dust emission module, together with the other dust emission modules, can be chosen in combination with the GOCART simple chemistry option (Kang et al., 2011). We refer to the above model as WRF/Chem_Dust.

4 Dust scheme performance

4.1 Offline tests

To examine the performance of the new dust scheme, offline tests are first carried out. In these tests, α_N is set to 1. The scheme sensitivity to w_* and soil attributes is first examined. For this purpose, p_τ is computed for various w_* values in the range between 0.5 and $4\,\mathrm{m\,s^{-1}}$. The PBL depth z_i and the Obukhov length L are set to $z_i = 1000\,\mathrm{m}$ and $L = -10\,\mathrm{m}$. The results for $p_{|\tau|}$ are shown in Fig. 5a.

Analysis shows that τ_R is almost constant and always positive, indicating that the net momentum flux is directed downwards. In contrast to the small variation of τ_R, the standard deviation of τ increases with w_* corresponding to the rising intensity of turbulence, i.e. the stronger variations in u' and w' also result in stronger variations in τ. Due to the greater variance of τ, the overlap of the pdfs of τ and F_i also increases (Fig. 1b). As a result, dust emission increases with w_*. The small variation of τ_R is understandable, because the shear stress due to the mean wind is not included. Clearly, the inclusion of u_* would lead to increased variations in τ_R. The characteristics of p_τ for different wind and stability conditions as well as the implications to dust emission will be described in a future study.

Tests are performed to investigate the dependency of dust emission F on w_* for different soil types (Fig. 5b). As α_N is not yet known, F/α_N is shown (a preliminary estimate of α_N is given in Sect. 4.2.1). For constant w_*, F is weak for soils with large particles (e.g. sand), and clearly increases for soils rich in small particles (e.g. clay). Figure 5b also shows that F substantially increases with w_*.

4.2 Case study

The WRF/Chem_Dust model is implemented to the Taklimakan Desert to the simulation of a weakly convective dust event. The numerical results are then compared with the measurements of a ground-based lidar at the Aksu Water Balance Experimental Station, Xinjiang Institute of Ecology and Geography of the Chinese Academy of Sciences (Jin et al., 2010). The station is located in the northern part of the Taklimakan Desert (40.62° N, 80.83° E, 1028 m above sea level). The measurements were taken with a Mie-scattering polarization lidar, which continuously determines the vertical distribution of aerosols from the PBL through the troposphere up to the stratosphere (Kai et al., 2008). The three-day period, 23–25 March 2009, is chosen for comparison with the simulations. During these days, the noon time (14 LST) surface heat flux fell between 100 and $250\,\mathrm{W\,m^{-2}}$ in much of the simulation domain (not shown). At the fringes of the Taklimakan desert, it exceeded $300\,\mathrm{W\,m^{-2}}$ on occasions. The ratio of z_i/L was mostly less than -45. Thus, the case studied is convective, and satisfies the requirement for testing the scheme. Although convective turbulence is more prevalent in summer, we have at this stage no other suitable data for model verification.

The model run is set up with a horizontal resolution of 25 km. The domain extends over 1500 km × 750 km, which corresponds to 60 grid points in x-direction and 30 in y-direction. The domain as well as the topographical height can be seen in Fig. 7. In the vertical direction, 28 model levels are used up to a pressure level of 50 hPa. The Yonsei University (YSU) PBL scheme (Hong et al., 2006) was applied to

estimate w_* and z_i. The source areas for dust emission calculation have been defined as suggested by Shao and Dong (2006). The authors calculated the dust concentration on the basis of synoptic visibility reports using an empirical relationship. A location is classified as a potential dust source area if the average dust concentration exceeds a threshold value and additional criteria regarding erodibility and vegetation cover are satisfied. The potential dust source area is shown in Fig. 7 (background, dotted).

The geographical data are interpolated from terrestrial data based on the default 24-category land use classification and 16-category soil classification in WRF with a 10 m resolution. The vegetation cover data used in this study is combined from vegetation type data of the State Key Laboratory of Resources and Environment Information System (LREIS) of the Institute of Geography, Chinese Academy of Sciences, and NDVI (Normalized Differenced Vegetation Index) data derived from NOAA/NASA (National Oceanic and Atmospheric Administration/National Aeronautics and Space Administration) Pathfinder AVHRR (Advanced Very High Resolution Radiometer) land dataset (Shao and Dong, 2006). The meteorological initial and lateral boundary conditions are specified by the 6-hourly Final Analysis data (FNL) of the NCEP Global Forecast System (GFS) with 1° resolution. Four sequential model runs have been made to enable a full update of the meteorological conditions every 24 h. Thus, the simulation covers 22 March 2009 00:00 UTC to 26 March 2009 00:00 UTC, which corresponds to 22 March 05:30 LST to 26 March 05:30 LST, including one day spin up time before the period of comparison. The resulting dust concentration of each one-day simulation is passed to the consecutive simulation as initial condition. Four particle size bins are currently used in the model: $d \leq 2.5$, $2.5 < d \leq 5$, $5 < d \leq 10$, and $10 < d \leq 20\,\mu$m respectively for bins 1–4.

4.2.1 Comparison to lidar measurements

A lidar measures the backscattering of aerosols, water droplets, and other scattering objects in the atmospheric column through which the lidar beam passes. The backscattering coefficient of aerosols, β_a, can be used to calculate quantities such as backscattering ratio R, which is the ratio of total (molecular plus aerosol) to molecular backscattering,

$$R(z) = \frac{\beta_m(z) + \beta_a(z)}{\beta_m(z)} \tag{23}$$

with β_m being the backscattering coefficient of molecules (Kai et al., 2008). R is measured in 60 m height intervals and the lidar overlap effect is empirically corrected before the lidar data are used for the analysis. Dust concentration, c, can be approximated based on the backscattering ratio, R, according to

$$c = a \cdot R \tag{24}$$

where $a = 0.04\,\mathrm{mg\,m^{-3}}$ is a coefficient determined by fitting R to c derived from the near-surface dust concentration (observed using high volume sampler) and a prespecified dust concentration profile.

The column dust load in turn can be derived by integrating the dust concentration in the vertical direction. We assume that all aerosols below the cloud base are dust particles and the column dust load is determined by emission, advection, and deposition. In reality, not all aerosols are dust particles and a background aerosol concentration is present in the atmosphere, which has to be removed from the measurements for comparison with the model simulation. Since no initial conditions of aerosol concentration for the dust-free situations are available, a mean profile is calculated and removed from the concentration data.

We first compared the model-simulated and lidar-observed dust load below the lowest cloud base (about 4300 m for the study period). This comparison turned out to be less meaningful, because for reasons yet to be clarified, the highest dust concentration occurred in heights above the boundary layer. The dust there was unlikely to be related to local convective dust emission. For this reason, we used the model-simulated boundary layer height (pblh) as the reference level and calculated the PBL dust load by integrating the dust concentration up to pblh. To find the most appropriate comparison, we tested several options by comparing the lidar data with the model data (I) from the Aksu grid cell, (II) averaged over 9 grid cells surrounding Aksu, and (III) averaged over 25 grid cells surrounding Aksu. The α_N parameter is calculated for each of these options by fitting the model data to the lidar data for the 12-h period between 12:00 and 24:00 LST, 24 March 2009, by using a MATLAB® robust curve fitting technique with a Cauchy weighting function. Figure 6a, c, and e show the scatter plots of the model versus the lidar PBL dust load, together with the linear regressions. Colors indicate the time of the data points. From the slope of the straight lines, we found $\alpha_N = 1912.9$, 785.2, and $685.1\,\mathrm{m^{-2}}$ for comparison options I, II and III, respectively. Figures 6b, d, and e show the PBL dust load for the days of 23–25 March 2009 estimated from the lidar data and the model simulations using the calibrated α_N values. Note that the lidar PBL dust load also varies slightly as the pblhs estimated for options I, II, and III are somewhat different.

Figure 6a and b present the results for option I. The diurnal cycle of the dust loading is reproduced, but some problems exist. The model overestimated the PBL dust load for the mornings of 24 and 25 March and the evening of 25 March. Figure 6c and d present the results for option II and III. The degree of agreement between the lidar and model data is similar for both options, except for 23 March. Again, the model over predicted the PBL dust load for the evening of 25 March. Only in option III (Fig. 6f), the model shows a decreasing PBL dust load at this time. No substantial differences between options II and III can be seen for other times.

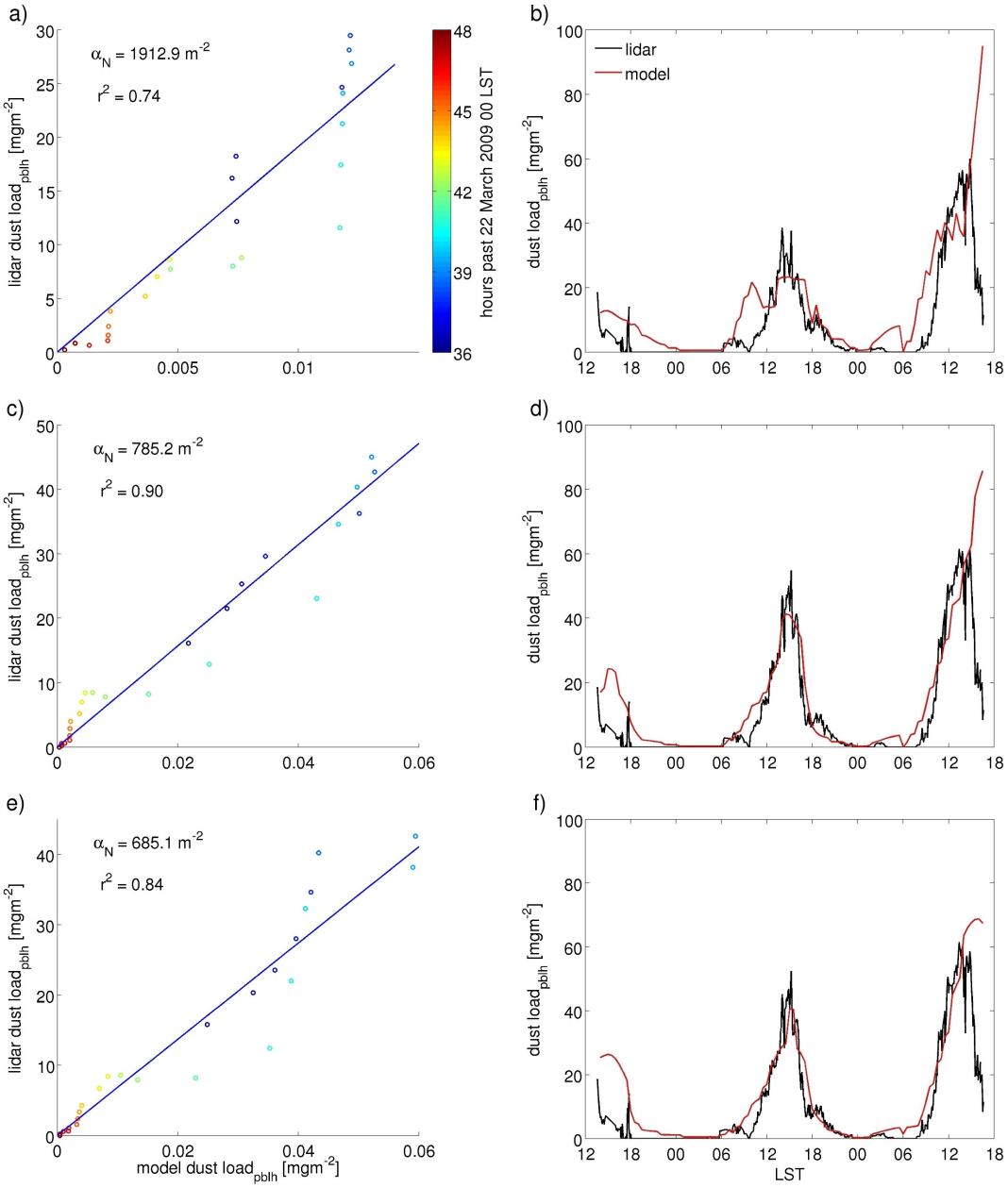

Fig. 6. **(a)** Scatter plot of model versus lidar PBL dust load for option I (one grid cell) for the 12-h period (12:00 to 24:00 LST, 24 March 2009) for determination of α_N as the slope of the linear relationship, with r^2 denoting the coefficient of determination. **(b)** PBL dust load derived from lidar data (black) and simulations (red) for 23, 24, and 25 March 2009. **(c)** as **(a)** and **(d)** as **(b)**, but for option II (9 grid-cell average); **(e)** as **(a)** and **(f)** as **(b)** but for option III (25 grid-cell average). Lidar data from K. Kai and Y. Jin, with acknowledgment.

The calibrated value of α_N decreased from 1912.9 to 685.1 m^{-2} from option I to III. By comparing the model results for the Aksu grid cell and the adjacent grid cells, it is found that the model-simulated dust emission for the Aksu grid cell is smaller. To reduce the model uncertainties, it seems reasonable to accept the α_N values obtained from option II and III. The difference between the α_N values is relatively small and therefore, $\alpha_N = 785.2\,\mathrm{m}^{-2}$ is used for subsequent model runs. The coefficient of determination r^2 (see Fig. 6) underlines this choice as option II also has the highest value of $r^2 = 0.90$.

4.2.2 Quantitative analysis

The above described case is rerun with α_N set to 785.2 m^{-2}. The model simulation shows that dust emission in the Taklimakan Desert is primarily limited to the desert fringes. As example, Fig. 7 shows the predicted dust emission for

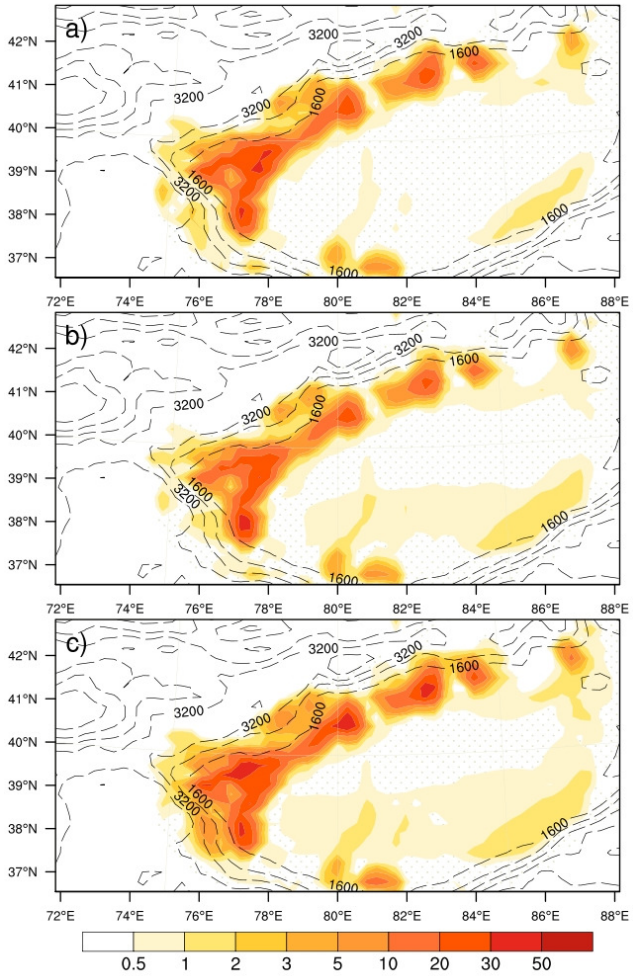

Fig. 7. Predicted emission flux (in $\mu g\,m^{-2}\,s^{-1}$) for 14:00 LST on **(a)** 23, **(b)** 24, and **(c)** 25 March 2009, together with the potential dust source area (background, dotted) and topographical height (contours up to 4800 m in 800 m intervals).

14:00 LST on 23, 24 and 25 March 2009, when convective turbulence is expected to be the strongest. The pattern of dust emission clearly shows its dependency on soil type. In the interior of the Taklimakan Desert, where sand is the dominant soil type, there is little dust emission. For areas where dust emission occurred, the total (all particle size) dust emission fell between 1 and 30 $\mu g\,m^{-2}\,s^{-1}$ at noon time, reaching occasionally a maximum of 50 $\mu g\,m^{-2}\,s^{-1}$. The dust concentration in the lowest model layer is up to 150 $\mu g\,m^{-3}$ in the areas of dust emission, reaching on occasions a maximum of 300 $\mu g\,m^{-3}$.

To study the influence of soil composition on dust emission in greater detail, four locations are selected from the domain representing the four soil groups used for the simulation as follows:

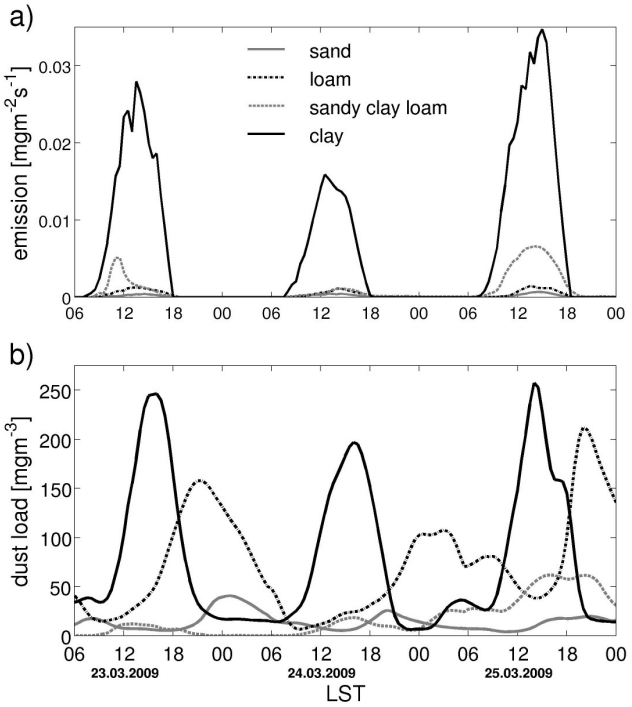

Fig. 8. Time series of **(a)** dust emission and **(b)** dust load of all particle sizes for the days 23, 24, and 25 March 2009 for the four locations representing clay, sandy clay loam, clay, and sand.

1. (77.1° E, 39.5° N) for clay,
2. (76.0° E, 38.3° N) for sandy clay loam,
3. (75.0° E, 39.7° N) for loam, and
4. (78.6° E, 38.4° N) for sand.

The time series of dust emission, column dust load, and w_* are analyzed for the four locations. Figure 8 shows the time series of dust emission and dust load for all particle sizes. Clay consists a high proportion of small particles and reveals a clear connection between dust emission and convection, which is most prevalent during noon (Fig. 8a). Sandy clay loam also contains a high fraction of dust and an obvious relation between dust emission and w_* (for this location, w_* is relatively small, not shown). In contrast, loam contains only a small fraction of dust (Fig. 3a) and hence gives less dust emission. The relatively large dust load (Fig. 8b) found at the location is due to advection rather than local emission, as revealed by the fact that the high dust loads occurred during night. Sand is predominantly composed of large particles and hence produces little convective dust emission.

4.2.3 Dust budget

A dust budget is calculated to estimate the total convective dust emission over the study domain. The dust budget equation, integrated over the 3-D study domain, can be written as

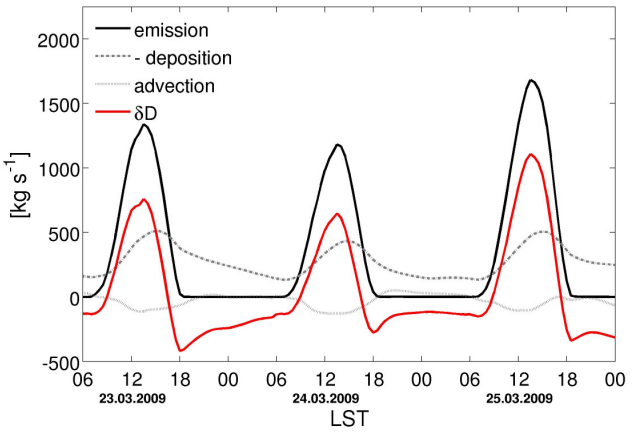

Fig. 9. Domain integrated dust emission, deposition (negative) and advection [kg s^{-1}]. Dust load change with time, δD, is calculated according to Eq. (25).

$$\delta D = \mathrm{AF} - \mathrm{AF}_D - \mathrm{AF}_{A_u} - \mathrm{AF}_{A_v} \quad (25)$$

where δD is the change with time of the dust load over the domain, AF the total dust emission, AF_D the total dust deposition and AF_{A_u} and AF_{A_v} the transport through the lateral boundaries. Figure 9 shows their time series. Up to about 1500 kg s^{-1} of dust are emitted at noon time each day by convective turbulence. This makes a total emission of 86.5 kt for the three-day period in the study domain. Deposition reaches about 500 kg s^{-1} during the time of maximum dust concentration and the total amount of deposited dust for the study period is 70.3 kt. Advection is relatively small during the study period due to the weak winds. δD reaches up to 1000 kg s^{-1} at noon time. The accumulated dust load over the study period is 7.3 kt.

4.2.4 Model uncertainties

In conventional dust emission schemes, the threshold friction velocity, u_{*t}, is a key parameter. An ideal u_{*t} is defined, which depends only on particle diameter, and it is then corrected to account for the influences of the environmental factors, such as surface roughness, soil moisture, salt crust, etc., by multiplying the ideal u_{*t} with correction functions (Shao, 2008). In our scheme, the concept of threshold friction velocity is not used, and the influences of the environmental factors are reflected in the probability distributions of F_i and $|\tau|$. As pointed out in Sect. 3.1, our estimate of $p(F_i)$ is provisional. The parameters used to estimate $p(F_i)$ are likely to have considerable uncertainties and vary from case to case depending on the prevailing environmental conditions. To investigate the uncertainties arising from the $p(F_i)$, we conducted a set of sensitivity experiments in which we (a) increased and (b) reduced the mean value $\bar{F}_i$ by 20 %, and (c) increased and (d) reduced the standard deviation σ_{F_i} by 20 %. The perturbed $p(F_i)$ functions for the sensitivity experiments are shown in Fig. 10a. We repeated the model simulations for 24 March with the new $p(F_i)$ functions and compared the herewith obtained dust emissions with respect to the reference run. Figure 10b shows the domain integrated emission for 24 March 2009 for the sensitivity experiments together with the reference dust emission ±10 %. As can be seen, a 20 % increase/decrease in $\bar{F}_i$ leads to about 5 % decrease/increase in dust emission. In comparison, the changes in σ_{F_i} only affect the predicted dust emission to a small degree. This is because the changes in $p(F_i)$ are rather small. Spatially, the changes in $\bar{F}_i$ resulted in about 5 % changes in dust emission in most regions where dust emission occurred, whereas the changes in σ_{F_i} produced significant changes only in the regions of strong emission (up to 5 %, not shown).

5 Concluding remarks

In this paper, a parameterization scheme for convective dust emission is presented. We have pointed out that convective dust emission may play an important role in the global dust budget and the mechanisms for convective dust emission differs profoundly from that for dust emission generated by the saltation of sand-sized grains driven by the mean wind. The construction of the new scheme is based on two important observations: (1) convective eddies generate intermittently large shear stresses on fractions of the aeolian surface; and (2) due to the stochastic nature of inter-particle cohesion, there always exists a fraction of free dust that can be entrained into the air by turbulence or weak winds without saltation. The fundamental difference between our scheme and the conventional dust emission schemes is that in our scheme the stochastic nature of dust emission has been taken into consideration, in terms of the probability distributions of the inter-particle cohesive forces and the turbulent shear stress.

We have developed the WRF/Chem_Dust model by integrating the new dust emission scheme, together with several other conventional schemes (Kang et al., 2011), into the WRF/Chem model, which is then applied to the simulation of a convective dust event in the Taklimakan Desert. The model results are compared with the lidar data obtained at Aksu. The model is found to be able to reproduce the basic spatial and temporal features of dust patterns in the atmospheric boundary layer. We have used the lidar data for a 12-h period to calibrate the model parameter α_N and found α_N to be around 785.2 m^{-2}. Based on this choice of α_N, convective dust emission is found to be of the order of magnitude 1 to 10 µg m^{-2} s^{-1} up to a maximum of 50 µg m^{-2} s^{-1} at noon time. During the three-day study period, a total of 86.5 kt dust are emitted from, and 70.3 kt are deposition to, the study area (1500×750 km^2), resulting in a net dust emission of 7.3 kt.

The model-lidar comparison must be viewed in light of several limitations. The study area and the selected dates

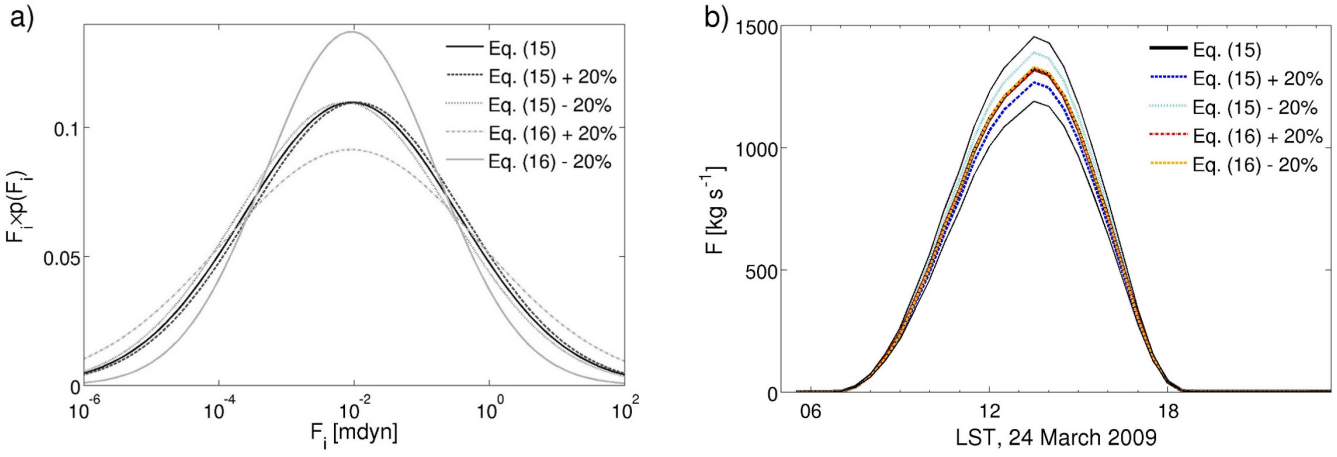

Fig. 10. **(a)** Distribution of $F_i \times p(F_i)$ for $\bar{F}_i \pm 20\,\%$ and $\sigma_{F_i} \pm 20\,\%$ with respect to the reference values. **(b)** Domain integrated dust emission [kg s^{-1}] for the sensitivity experiments shown in **(a)**.

(23–25 March 2009) for the model validation are by no means optimal. In the Taklimakan Desert, convective turbulence during this time of the year is not as pronounced as in summer. Also, the presence of clouds during the study period reduced the incoming radiation and prevented surface heating. The topography around Aksu is rather complicated, as it is located close to the Tianshan Mountains. The flow there can be strongly influenced by the mountain-valley winds, especially in the morning and evening. The flow in the Taklimakan Desert, surrounded by the Tibetan Plateau, the Pamir Plateau and the Tianshan Mountains, is also very complex. Kim et al. (2009) studied the dust layer height at Aksu in April 2002 and found its diurnal variation is strongly influenced by the local circulation which can lead to increased dust load in the morning and night. This phenomenon is also embedded in the lidar measurements used in this study. Aksu is therefore not an ideal site for the calibration of our model. The Sahara would be a more suitable reference for testing our model, but we have so far no available data for the area.

A more reliable calibration of the α_N parameter is also desirable. The lidar data used in this study have considerable uncertainties in determining dust load in the atmospheric boundary layer due to the overlapping effect. Further, as indicated in Sect. 3.1, the parameterization of the cohesive force is only provisional.

Given the above restrictions, we consider the model and the lidar data to be in reasonable agreement. With the calibrated α_N value, typical convective dust emission is found to be about $3\,\mu g\,m^{-2}\,s^{-1}$ for clay and $1\,\mu g\,m^{-2}\,s^{-1}$ for sandy clay loam for $w_* = 1\,m\,s^{-1}$. The typical magnitude of convective dust emission is consistent with that of the dust emission observed under weak wind conditions ($u_* \leq u_{*t}$), as reported in the literature (Fig. 7.2 of Shao, 2008). Nickling and Gillies (1993) measured the near-surface vertical dust flux for non-dust storm periods in Mali and reported values around $1\,\mu g\,m^{-2}\,s^{-1}$ for $u_* < 0.2\,m\,s^{-1}$. Dust flux measurements made under weak wind conditions for other regions show the same order of magnitude (Nickling et al., 1999).

Several improvements to the proposed scheme are planned. In this study, we concentrated on dust emission by convective turbulence and assumed turbulence is buoyancy driven. We have therefore used w_* as the scaling velocity for the variances of turbulent velocity according to the mixed-layer similarity theory. In fact, turbulence can be both shear-driven and buoyancy-driven. Moeng and Sullivan (1994) introduced a more general velocity scale w_m for turbulence, which combines buoyancy and shear production of turbulence,

$$w_m^3 = w_*^3 + 5u_*^3. \quad (26)$$

For the generalization of the proposed scheme, such a combination of u_* and w_* would provide a more adequate parameterization for the pdf of the instantaneous shear stress.

In conventional dust emission schemes, threshold friction velocity u_{*t} is used, which is first calculated for ideal conditions (dry and bare soil) and then corrected to account for the effects of surface roughness, soil moisture, salt content, crust, etc. (Shao, 2008). In this study, u_{*t} is not used, but the impact of the above-mentioned environmental factors must be reflected in the probability distributions of the cohesive forces. The stochastic nature of the cohesive force and its statistical quantification will be the most formidable, yet unavoidable, problem for the application of the new scheme.

Acknowledgements. We are grateful to Prof. Kenji Kai and Dr. Yoshitaka Jin from the Nagoya University of Japan for the provision of the lidar data used for the comparison with our scheme. We also wish to thank the two anonymous reviewers for their suggestions which helped to improve the manuscript.

Edited by: J. Quaas

References

Ansmann, A., Tesche, M., Knippertz, P., Bierwirth, E., Althausen, D., Müller, D., and Schulz, O.: Vertical profiling of convective dust plumes in southern Morocco during SAMUM, Tellus, 61B, 340–353, doi:10.1111/j.1600-0889.2008.00384.x, 2008.

Chin, M., Rood, R. B., and Lin, S.-J.: Atmospheric sulfur cycle simulated in the global model GOCART: Model description and global properties, J. Geophys. Res., 105, 24671–24687, 2000.

Gledzer, E. B., Granberg, I. G., and Chkhetiani, O. G.: Convective Aerosol Fluxes near the Ground Surface, Doklady Earth Sci., 426, 652–657, doi:10.1134/S1028334X09040321, 2009.

Grell, G. A., Peckham, S. E., Schmitz, R., McKeen, S. A., Frost, G., Skamarock, W. C., and Eder, B.: Fully coupled "online" chemistry within the WRF model, Atmos. Environ., 39, 6957–6975, doi:10.1016/j.atmosenv.2005.04.027, 2005.

Heintzenberg, J.: The SAMUM-1 experiment over Southern Morocco: overview and introduction, Tellus, 61B, 2–11, doi:10.1111/j.1600-0889.2008.00403.x, 2008.

Hong, S.-Y., Noh, Y., and Dudhia, J.: A new vertical diffusion package with an explicit treatment of entrainment processes, Mon. Weather Rev., 134, 2318–2341, 2006.

Ito, J., Niino, H., and Nakanishi, M.: Large eddy simulation on dust suspension in a convective mixed layer, SOLA, 6, 133–136, doi:10.2151/sola.2010-034133, 2010.

Jin, Y., Kai, K., Shibata, T., Zhang, K., and Zhou, H.: Validation of the dust layer structure over the Taklimakan desert, China, by the CALIOP space-born LIDAR using gound-based LIDAR, SOLA, 6, 121–124, doi:10.2151/sola.2010-031, 2010.

Kai, K., Nagata, Y., Tsunematsu, N., Matsumura, T., Kim, H.-S., Matsumoto, T., Hu, S., Zhou, H., Abo, M., and Nagai, T.: The structure of the dust layer over the Taklimakan desert during the dust storm in April 2002 as observed using a depolarization lidar, J. Meteor. Soc. Japan, 86, 1–16, 2008.

Kaimal, J. C. and Finnigan, J. J.: Atmospheric Boundary Layer Flows, their Structure and Measurement, Oxford University Press, Oxford, 1994.

Kang, J.-Y., Yoon, S.-C., Shao, Y., and Kim, S.-W.: Comparison of vertical dust flux by implementing three dust schemes into WRF/Chem, J. Geophys. Res., 116, D09202, doi:10.1029/2010JD014649, 2011.

Kim, H.-S., Nagata, Y., and Kai, K.: Variation of dust layer height in the northern Taklimakan Desert in April 2002, Atmos. Environ., 43, 557–567, doi:10.1016/j.atmosenv.2008.10.023, 2009.

Knippertz, P. and Todd, M. C.: Mineral dust aerosols over the Sahara: Meteorological controls on emission and transport and implications for modeling, Rev. Geophys., 50, doi:10.1029/2011RG000362, 2012.

Koch, J. and Renno, N. O.: The role of convective plumes and vortices on the global aerosol budget, Geophys. Res. Lett., 32, L18806, doi:10.1029/2005GL023420, 2005.

Koehler, K. J. and Symanowski, J. T.: Constructing Multivariate Distributions with Specific Marginal Distributions, J. Multivar. Anal. 55, 261–282, 1995.

Loosmore, G. A. and Hunt, J. R.: Dust resuspension without saltation, J. Geophys. Res., 105, 20663–20671, doi:10.1029/2000JD900271, 2000.

Manomaiphiboon, K. and Russell, A. G.: Formulation of joint probability density functions of velocity for turbulent flows: an alternative approach, Atmos. Environ., 37, 4917–4925, doi:10.1016/j.atmosenv.2003.08.022, 2003.

Marticorena, B. and Bergametti, G.: Modeling the atmospheric dust cycle: 1. Design of a soil-derived dust emission scheme, J. Geophys. Res., 100, 16415–16430, 1995.

Marticorena, B., Bergametti, G., Aumont, B., Callot, Y., N'Doumé, C., and Legrand, M.: Modeling the atmospheric dust cycle: 2. Simulation of Saharan dust sources, J. Geophys. Res., 102, 4387–4404, 1997.

Moeng, C.-H. and Sullivan, P. P.: A comparison of shear- and buoyancy-driven planetary boundary layer flows, J. Atmos. Sci., 51, 999–1022, 1994.

Nickling, W. G. and Gillies, J. A.: Dust emission and transport in Mali, West Africa, Sedimentology, 40, 859–868, 1993.

Nickling, W. G., McTainsh, G. H., and Leys, J. F.: Dust emission from the Channel Country of western Queensland, Australia, Z. Geomorph. N.F., 116, 1–17, 1999.

Schlichting, H., Gersten, K., and Krause, E.: Boundary-layer theory, Springer-Verlag, Berlin, 8., rev. and enl. ed., corr. print. edn., 2003.

Shao, Y.: A model for mineral dust emission, J. Geophys. Res., 106, 20239–20254, 2001.

Shao, Y.: Simplification of a dust emission scheme and comparison with data, J. Geophys. Res., 109, D10202, doi:10.1029/2003JD004372, 2004.

Shao, Y.: Physics and Modelling of Wind Erosion, Springer–Verlag, Berlin, 2 edn., 2008.

Shao, Y. and Dong, C. H.: A review on East Asian dust storm climate, modelling and monitoring, Global Planet. Change, 52, 1–22, doi:10.1016/j.gloplacha.2006.02.011, 2006.

Shao, Y., Raupach, M. R., and Findlater, P. A.: The effect of saltation bombardment on the entrainment of dust by wind, J. Geophys. Res., 98, 12 719–12 726, 1993.

Shao, Y., Fink, A. H., and Klose, M.: Numerical simulation of a continental-scale Saharan dust event, J. Geophys. Res., 115, D13205, doi:10.1029/2009JD012678, 2010.

Shao, Y., Wyrwoll, K.-H., Chappell, A., Huang, J., Lin, Z., McTainsh, G. H., Mikami, M., Tanaka, T. Y., Wang, X., and Yoon, S.: Dust cycle: An emerging core theme in Earth system science, Aeolian Research, 2, 181–204, doi:10.1016/j.aeolia.2011.02.001, 2011.

Stull, R. B.: An Introduction to Boundary Layer Meteorology, Kluwer Academic Publishers, Norwell, 1988.

Wang, W., Bruyère, C., Duda, M., Dudhia, J., Gill, D., Lin, H.-C., Michalakes, J., Rizvi, S., and Zhang, X.: ARW Version 3 Modeling System User's Guide, http://www.mmm.ucar.edu/wrf/users/docs/user_guide_V3/ARWUsersGuideV3.pdf, 2009.

Zimon, A. D.: Adhesion of dust and powder, Consultants Bureau, New York, USA, 1982.

3 Large-eddy simulation of turbulent dust emission

Reference:

Klose, M., and Y. Shao (2013), Large-eddy simulation of turbulent dust emission, *Aeolian Research*, *8*, 49–58, doi: 10.1016/j.aeolia.2012.10.010

Supplementary material to Chapter 3 is provided in Appendix A.

Aeolian Research 8 (2013) 49–58

Contents lists available at SciVerse ScienceDirect

Aeolian Research

journal homepage: www.elsevier.com/locate/aeolia

Large-eddy simulation of turbulent dust emission

Martina Klose *, Yaping Shao

Institute of Geophysics and Meteorology, University of Cologne, Kerpener Str. 13, 50937 Cologne, Germany

ARTICLE INFO

Article history:
Received 26 July 2012
Revised 5 October 2012
Accepted 13 October 2012

Keywords:
Turbulent dust emission
Convective dust
Large-eddy dust modeling
Surface shear stress
WRF
Wind erosion

ABSTRACT

Turbulent dust emission is an important mechanism to be considered in dust models. For example, over a heated desert surface under weak wind conditions, convective turbulence can be highly developed, which generates patches of enhanced shear stresses and entrains dust into the atmosphere. This mechanism of dust emission differs from those considered in existing dust emission schemes because it does not have to involve the saltation of sand-sized particles. In this study, we develop a large-eddy dust model, WRF-LES/D, by coupling the WRF large-eddy flow model with a new dust mobilization scheme. It is then applied to the simulation of turbulent dust emission under various stability and wind conditions. Our aim is to understand how turbulent dust emission occurs and how turbulent dust fluxes depend on atmospheric control parameters. We show that, due to the complexity of turbulent motion and the dust cohesive forces, turbulent dust emission is a stochastic process which needs to be statistically quantified. With the numerical results, we quantify the large-eddy induced shear stresses on the surface and turbulent dust emissions in terms of probabilistic distributions. For a given soil type, it is shown that these distributions can be described in terms of a few control variables, including the friction velocity, u_*, and the convective scaling velocity, w_*.

1. Introduction

Dust emission parameterization schemes (here after dust schemes) for regional and global dust models have been under development since the early 1990s (e.g. Shao et al., 1993; Marticorena and Bergametti, 1995; Alfaro and Gomes, 2001; Zender et al., 2003; Shao, 2004; Kok, 2011). In these schemes, saltation bombardment and aggregates disintegration are considered to be the main mechanisms. The successful applications of these schemes to regional and global dust modeling have been reported in numerous studies (e.g. Tanaka and Chiba, 2006; Reinfried et al., 2009; Darmenova et al., 2008; Uno et al., 2009), but they are not applicable to weak wind conditions when there is no saltation. Experiences show that turbulent dust emission, i.e., dust emission due to convective turbulent motion in the absence of strong mean wind, is not insignificant, as exemplified by the dust devils often observed over heated desert surfaces. On Mars, dust devils are most important to dust emission (Balme and Greeley, 2006; Greeley et al., 2006). Aeolian dust is the primary source of iron supply to the surface oceans, vital to the phytoplankton growth and air–sea carbon exchange (Mahowald et al., 2009; Maher et al., 2010). While strong dust events are important to the episodic increase in atmospheric dust concentration, the weak but frequent dust events may be more important in maintaining the background dust concentration and the continuous dust supply to sustain the ocean biomass productivity.

Convective turbulent dust emission (CTDE) is the most outstanding form of turbulent dust emission. While CTDE is widely perceived to be important, no scheme existed for its quantitative estimate until the recent work of Klose and Shao (2012). The classic view has been that dust emission is related to the motion of sand-sized grains driven by the mean wind (Bagnold, 1941; Shao, 2008), as illustrated in Fig. 1a. The mechanism of CTDE is different, as shown in Fig. 1b: in a convective atmospheric boundary layer, large eddies have coherent structures (e.g. micro-bursts, vortex rolls and vortices) of dimensions comparable to boundary-layer depth. These eddies are efficient entities in generating localized momentum fluxes to the surface. Although the eddies only occupy fractions of time and space, the momentum fluxes to these fractions can be many times the average. Consequently, the surface intermittently experiences patches of strong shear stresses which entrain dust into the atmosphere. The essential differences between CTDE and the dust emission mechanisms considered in "traditional" dust schemes are (1) CTDE is stochastic and (2) it does not have to, although it can, involve saltation.

Research is needed to understand the dynamics of CTDE for its parameterization in large scale models. This is a challenging problem due to the rapid change of turbulence scales close to the surface and the random factors which affect surface properties. To our knowledge, no field or laboratory experiments on CTDE have ever been carried out. Large-eddy simulation provides a powerful

* Corresponding author. Tel.: +49 221 470 5776; fax: +49 221 470 5161.
E-mail addresses: mklose@uni-koeln.de (M. Klose), yshao@uni-koeln.de (Y. Shao).

1875-9637/$ - see front matter © 2012 Elsevier B.V. All rights reserved.
http://dx.doi.org/10.1016/j.aeolia.2012.10.010

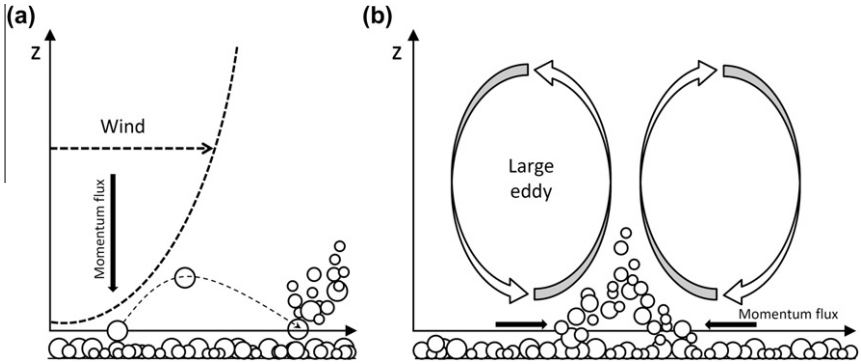

Fig. 1. (a) Conventional view of dust emission via saltation bombardment induced by the momentum flux to the surface by the mean wind. (b) Illustration of particle lifting caused by the momentum intermittently transported to the surface by turbulent eddies. Saltation may be but does not need to be involved.

tool to studying the problems of CTDE. This technique has been widely used to modeling atmospheric turbulent flows (Deardorff, 1970; Moeng et al., 2007), also in relation to dust devils (Michaels and Rafkin, 2004). Kanak et al. (2000) and Kanak (2005) showed that vortices can be generated from convective cells or branches of convective cells forced under the conditions of strong heat flux and weak wind shear. Ohno and Takemi (2010) found that the merge of multiple vortices with the same sign of vorticity is important for strengthening and maintaining intense vortices. While these numerical studies provided a better understanding of dust-devil dynamics, they are done without dust.

We study the mechanisms of CTDE by means of large-eddy modeling, focusing on two important issues, namely, (1) how convective turbulence produces surface shear stresses and how the probability distributions of the shear stress can be statistically quantified, and (2) how convective turbulence generates dust emission and how size-resolved dust emission depends on macroscopic atmospheric conditions. Our hypothesis is that the impact of large eddies on dust emission can be statistically evaluated from the model simulations and CTDE can be expressed in terms of a small number of environmental control parameters. To this end, we develop a large-eddy dust model (WRF-LES/D) by coupling the Advanced Research WRF (Weather Research and Forecasting) large-eddy model (Skamarock et al., 2008) Version 3.2 with a new dust module. WRF-LES/D is then applied to simulating turbulent dust emission for various conditions of boundary-layer stability and flow speed for a given soil type. The numerical results are evaluated to answer the above listed questions. The purpose of this paper is not to validate WRF-LES/D, but to use it as a tool to establish a conceptual basis for the parameterization of CTDE and more generally of turbulent dust emission.

2. Large-eddy dust model

The large-eddy dust model, WRF-LES/D, couples the WRF large-eddy model with a new dust mobilization scheme.

2.1. Dust mobilization scheme

The ansatz of the new dust scheme differs from that of traditional dust emission schemes, in that the stochastic nature of dust emission is considered. This is done by taking into account the statistical distributions of turbulent shear stress and retarding forces on dust particles. We distinguish between turbulent shear stress and Reynolds shear stress. The latter on the surface is

$$\tau = -\rho\sqrt{(\overline{u'w'})^2 + (\overline{v'w'})^2} \tag{1}$$

where ρ is air density, u' and v' are the horizontal velocity derivations from the horizontal mean wind components $\bar{u}$ and $\bar{v}$, and w' is the vertical. The over-line denotes the Reynolds averaging (approximated in atmospheric boundary-layer studies by an averaging over 20 min). τ is the shear stress exerted by the mean wind on the surface, which is considered in traditional dust schemes to be the primary driver for the dust emission process. However, τ is not the suitable quantity for driving turbulent dust emission, because the motion and emission of dust particles respond to shear stresses varying on much shorter time scales. We thus define the instantaneous shear stress vector as

$$\vec{\tau}_f = \rho(uw)\,\vec{i} + \rho(vw)\,\vec{j} \tag{2}$$

with $u = \bar{u} + u'$, etc. Note that the direction of $\vec{\tau}_f$ is irrelevant to dust emission, but its magnitude

$$\tau_f = \rho\sqrt{(uw)^2 + (vw)^2} \tag{3}$$

is. The aerodynamic force that acts on a particle on the surface, f, is proportional to τ_f

$$f = \tau_f \pi d^2/4 \tag{3a}$$

Due to turbulent fluctuations, f is a stochastic quantity which obeys a pdf (probability density function), $p(f)$.

Two retarding forces act on a dust particle on the surface: the gravity force, $f_g = m_p g$ with dust particle mass, m_p, and gravitational acceleration, g, and the inter-particle cohesive force, f_i, i.e., $f_t = f_g + f_i$. For small particles, f_i dominates but depends on many factors, ranging from particle shape to soil mineralogical composition, and is best characterized as a stochastic variable. Suppose the pdf of the retarding force is $p(f_t)$. Then, dust emission due to turbulence must be proportional to the overlapping area between $p(f)$ and $p(f_t)$ as depicted in Fig. 2a.

Dust emission is the vertical dust mass flux at the surface. We interpret the "surface" as the top of the viscous layer adjacent to the ground (i.e., D in Fig. 2b). Suppose the dust particle number flux through that surface is n ($m^{-2}\,s^{-1}$) and the dust particle mass is m_p. Then the dust flux is

$$\tilde{F} = n \cdot m_p = N w_p m_p \tag{4}$$

where w_p is the vertical component of the dust particle velocity at the surface and N the dust particle number concentration in the viscous layer. The equation w_p obeys is

$$\frac{dw_p}{dt} = -\frac{w_p - w}{T_p} - \frac{f - f_t}{m_p} \tag{5}$$

with T_p being the particle response time. As f_i is zero as soon as the particle leaves the ground, by integrating Eq. (5) over the depth of D, we obtain an approximate solution for w_p

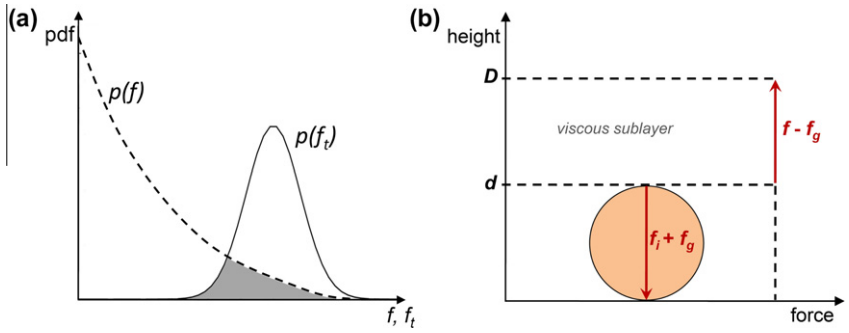

Fig. 2. (a) An illustration of the probability density functions $p(f)$ and $p(f_t)$; Turbulent dust emission is proportional to the $p(f) - p(f_t)$ overlap; (b) An illustration of the lifting and retarding forces acting on a particle on the surface.

$$w_p = -\frac{w_t}{2} + \frac{T_p}{2}\left(\frac{f}{m_p} - \frac{f_i}{m_p}\frac{d}{D}\right) \quad \text{for } f > f_i,\ D > d \tag{6}$$

where w_t is the particle terminal velocity. If we assume N is inversely proportional to D, i.e., $N = \alpha_N/D$ with α_N being a coefficient to be determined, Eq. (4) leads to a flux of the form

$$\tilde{F} = \begin{cases} \frac{\alpha_N}{2D}\left\{-w_t m_p + T_p\left(f - f_i\frac{d}{D}\right)\right\} & f > f_i,\ D > d \\ 0 & \text{else} \end{cases} \tag{7}$$

The dust emission for a given particle size d_j can now be estimated as

$$F_j = \int_0^\infty \left[\int_0^f \tilde{F}\cdot p_j(f_i)\cdot df_i\right] p(f)\cdot df \tag{8}$$

Eq. (7) and (8) can be simplified for specific distributions of $p_j(f_i)$ and $p(f)$. For example, for

$$p_j(f_i) = \delta(f_i - f_{i0})$$
$$p(f) = \delta(f - f_0)$$

we have

$$F_i = \begin{cases} \frac{\alpha_N}{2D}\left\{-w_t m_p + T_p\left(f_0 - f_{i0}\frac{d}{D}\right)\right\} & f_0 > f_{i0},\ D > d \\ 0 & \text{else} \end{cases} \tag{9}$$

The coefficient, α_N, is according to our preliminary estimate around 800 m^{-2} (Klose and Shao, 2012). Finally, for multi-sized soils, the total dust emission is

$$F = \int_o^{d_{max}} F_j p(d_j)\cdot \delta d_j \tag{10}$$

where d_{max} is the maximum size of dust particles (20 μm in our study) and $p(d_j)$ is the particle size distribution. In summary, Eq. (7), (8), and (10) constitute the scheme for CTDE. The scheme requires as input three probability distribution functions, two related to soil properties, i.e., the particle size distribution $p(d)$ and the cohesive force distribution $p(f_i)$, and one related to turbulence, i.e., the distribution of the aerodynamic force $p(f)$. In our study, $p(d)$ and $p(f_i)$ are specified and $p(f)$ is derived from the large-eddy model described in the following section.

2.2. Large-eddy flow model

The flow model of WRF-LES/D is based on the WRF large-eddy mode. WRF is a fully compressible non-hydrostatic model capable of large-eddy simulation (Moeng et al., 2007). For this study, a turbulent kinetic energy (TKE) based nonlinear backscatter and anisotropy (NBA) subfilter-scale stress model is used (Kosovic, 1997; Mirocha et al., 2010). This subfilter-scale stress (τ_{sg} equivalent) is estimated as

$$M_{ij} = -C_e l\left\{2(e)^{1/2}S_{ij} + \left(\frac{27}{8\pi}\right)^{1/3} C_s^{2/3} l\left[C_1\left(S_{ik}S_{kj} - \frac{1}{3}S_{mn}S_{mn}\delta_{ij}\right) + C_2(S_{ik}R_{kj} - R_{ik}S_{kj})\right]\right\} \tag{11}$$

with the strain-rate tensor $S_{ij} = 1/2(\partial u_{g,i}/\partial x_j + \partial u_{g,j}/\partial x_i)$ and rotation-rate tensor $R_{ij} = 1/2(\partial u_{g,i}/\partial x_j - \partial u_{g,j}/\partial x_i)$ of the resolved velocity components. C_s, C_e, C_1, and C_2 are functions of a constant backscatter coefficient C_b of 0.36 (Kosovic, 1997), so that the NBA model is consistent with a 1.5 order TKE closure (Lilly, 1967) in the limiting case of $C_b \to 0$.

Options for the parameterization of long and short-wave radiative transfer are included in WRF-LES/D (Skamarock et al., 2008). Also, the land-surface models available in WRF have been coupled with WRF-LES/D, e.g. the Noah land surface model (Chen et al., 1996; Chen and Dudhia, 2001). After a significant modification according to Shao et al. (submitted for publication), the modified scheme has multi vegetation layers and four soil layers with thicknesses of 0.01, 0.03, 0.06, and 0.1 m from top to bottom. This configuration with thin soil layers is necessary for large-eddy simulation. The land-surface model provides surface sensible and latent heat fluxes for the large-eddy flow model, and the land-surface quantities important to dust modeling (e.g. soil wetness). WRF-LES/D, with the capacity for turbulence, dust, radiation and land-surface modeling, is now a powerful tool for high-resolution dust simulation.

2.3. Numerical experiments

Numerical experiments are carried out with WRF-LES/D for various atmospheric stability and background-wind conditions (Table 1). The model horizontal resolution is 10 m and the vertical resolution changes with height (higher resolution closer to the surface). The Arakawa-C staggered grid is used and the depth of the lowest model layer is 0.5 m (grid center). The domain of the simulation is 2000 × 2000 × 1500 m^3 and the corresponding number of grid points is 200 × 200 × 90 (staggered dimensions). The simulation time is 90 min with an output interval of 10 s. The first 30 min of the simulation is the model spin up time. Accordingly, the remaining 60 min (361 time steps) data are used for analysis. For model initialization, the mean wind is logarithmic in the vertical and uniform in horizontal. The logarithmic wind profile is defined by the specified roughness length, z_0, and the friction velocity, u_*. For each experiment, a constant (with time) surface heat flux is specified. In other words, our experiments are for idealized cases and hence the land surface model and the radiation model are not activated to avoid unnecessary uncertainties. For the convective cases, an inversion is set at 1000 m. The lateral boundary conditions are periodic and implicit Rayleigh damping is used for vertical velocity in the top 300 m of the domain with a damping coefficient of 0.01.

In all experiments, the soil type is loam and $p(f_i)$ and $p(d)$ are pre-specified (Fig. 3). The cohesive force, f_i, is affected by multiple factors, including particle size, shape, geometry and the environmental controls such as soil wetness and chemical compositions. It is conceptually important to apply a probabilistic treatment to

Table 1
List of numerical experiments. Assumed are $z_0 = 10$ mm and a loam soil for all cases. For the convective cases, the boundary layer inversion height is set to $z_i = 1000$ m.

Name	u_* (m s^{-1})	H (W m^{-2})	w_* (m s^{-1})
Exp1	0.15	−50	−1.12*
Exp2	0.3	−50	−1.12
Exp3	0.5	−50	−1.12
Exp4	0.15	0	0
Exp5	0.3	0	0
Exp6	0.5	0	0
Exp7	0.15	200	1.77
Exp8	0.3	200	1.77
Exp9	0.5	200	1.77
Exp10	0.15	400	2.23
Exp11	0.3	400	2.23
Exp12	0.5	400	2.23
Exp13	0.15	600	2.55
Exp14	0.3	600	2.55
Exp15	0.5	600	2.55

* Undefined for stable conditions, but is formally computed by using $w_* = (gz_iH_0/\rho c_p\bar{\theta})^{1/3}$.

f_i. However, very little is known about the precise form of the cohesive force probability density function, $p(f_i)$. As a preliminary approximation, we use a log-normal distribution derived on the basis of a small dataset of Zimon (1982):

$$P(f_i) = \frac{1}{f_i\sqrt{2\pi}\sigma_{fi}} \exp\left(-\frac{(lnf_i - ln\bar{f}_i)^2}{2\sigma_{fi}^2}\right) \quad (12)$$

with the statistical moments given by

$$\bar{f}_i(d) = 10\exp(4.3569 - 0.2183d + 0.0018d^2)^{-1}$$
$$\sigma_{fi}(d) = 4.1095 - 0.0476d$$

where $\bar{f}_i$ and σ_{fi} are in 10^{-8} N and particle size d in μm. Fig. 3b shows $p(f_i)$ for five particle sizes between 2 and 20 μm. As $\bar{f}_i$ increases with particle size, σ_{fi} decreases, indicating the increased randomness of the cohesive force for smaller particles.

2.3.1. Instantaneous momentum flux

The parameterization of turbulent dust emission requires a simple method of quantifying $p(f)$. Knowledge of $p(f)$ can be obtained by studying the pdf of the momentum flux, $p(\tau_f)$, by using the results of the large-eddy simulations, because $p(f)$ is proportional to $p(\tau_f)$. In a large-eddy model, $\vec{\tau}_f$ is the sum of the grid-resolved component, $\vec{\tau}_g$ and the subgrid component, $\vec{\tau}_{sg}$, i.e.,

$$\vec{\tau}_f = \vec{\tau}_g + \vec{\tau}_{sg} \quad (13)$$

The magnitudes of $\vec{\tau}_g$, $\vec{\tau}_{sg}$, and $\vec{\tau}_f$ are, respectively

$$\tau_g = \rho\sqrt{(u_gw_g)^2 + (v_gw_g)^2}$$
$$\tau_{sg} = \sqrt{\tau_{sg,x}^2 + \tau_{sg,y}^2}$$
$$\tau_f = \rho\sqrt{(u_gw_g + \tau_{sg,x})^2 + (v_gw_g + \tau_{sg,y})^2}$$

If all turbulence is resolved, then $\tau_f = \tau_g$, while if turbulence is not at all resolved (close to surface), then $\tau_f = \tau_{sg}$. The various definitions of the momentum fluxes are summarized in Table 2. We

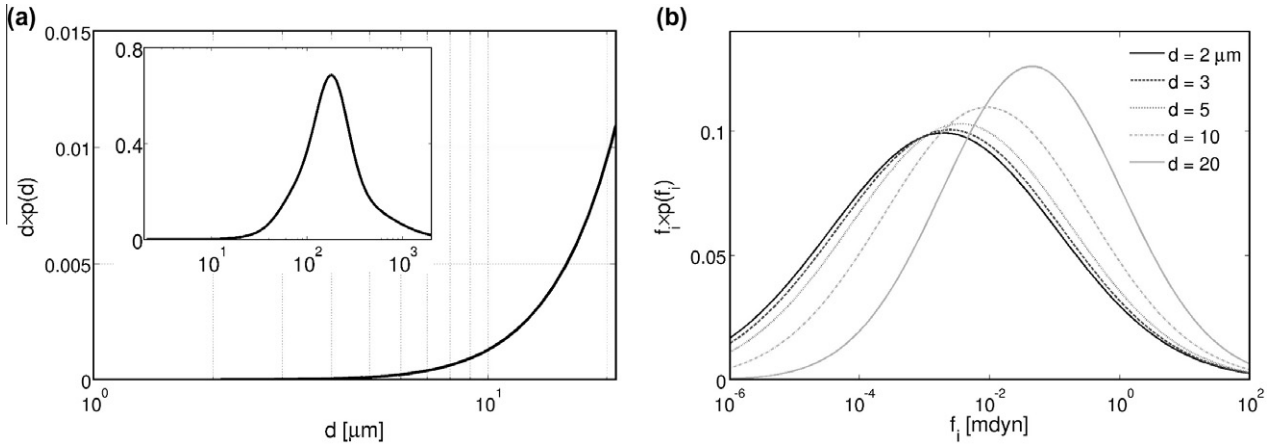

Fig. 3. (a) Particle size distribution of a loam soil for $d < 20$ μm used in the numerical experiments. Insertion: distribution for $d < 2000$ μm. (b) Probability distribution of the cohesive force for particle diameters of 2, 3, 5, 10, and 20 μm plotted in $f_i \times p(f_i)$ against f_i.

Table 2
A summary of the definitions of momentum fluxes.

Symbol	Mathematical expression	Physical meaning
$\vec{\tau}_f$	$\vec{\tau}_f = \rho(uw)\,\vec{i} + \rho(vw)\,\vec{j}$	Instantaneous momentum flux
τ_f	$\tau_f = \rho\sqrt{(u_gw_g + \tau_{sg,x})^2 + (v_gw_g + \tau_{sg,y})^2}$	Magnitude of $\vec{\tau}_f$
$\vec{\tau}_g$	$\vec{\tau}_g = \rho(u_gw_g)\,\vec{i} + \rho(v_gw_g)\,\vec{j}$	Grid resolved instantaneous momentum flux
τ_g	$\tau_g = \rho\sqrt{(u_gw_g)^2 + (v_gw_g)^2}$	Magnitude of $\vec{\tau}_g$
$\vec{\tau}_{sg}$	$\vec{\tau}_{sg} = \rho(u_gw_{sg})\,\vec{i} + \rho(u_{sg}w_g)\,\vec{i} + \rho(u_{sg}w_{sg})\,\vec{i} + \rho(v_gw_{sg})\,\vec{j} + \rho(v_{sg}w_g)\,\vec{j} + \rho(v_{sg}w_{sg})\,\vec{j}$	Subgrid instantaneous momentum flux; parameterized
τ_{sg}	$\tau_{sg} = \sqrt{\tau_{sg,x}^2 + \tau_{sg,y}^2}$	Magnitude of $\vec{\tau}_{sg}$
$\vec{\tau}$	$\vec{\tau} = \rho(\overline{u'w'} + \overline{\tau_{sg,x}})\,\vec{i} + \rho(\overline{v'w'} + \overline{\tau_{sg,y}})\,\vec{j}$	Shear stress of mean wind; Divergence of $\vec{\tau}$ is friction to mean wind
τ	$\tau = -\rho\sqrt{(\overline{u'w'} + \overline{\tau_{sg,x}})^2 + (\overline{v'w'} + \overline{\tau_{sg,y}})^2}$	Magnitude of $\vec{\tau}$. In boundary-layer meteorology, convention is to align x-direction with mean wind, U, then $\tau = -\rho(\overline{U'w'}) = \rho u_*^2$, as $\overline{U'w'}$ is always negative (momentum flux is downwards)

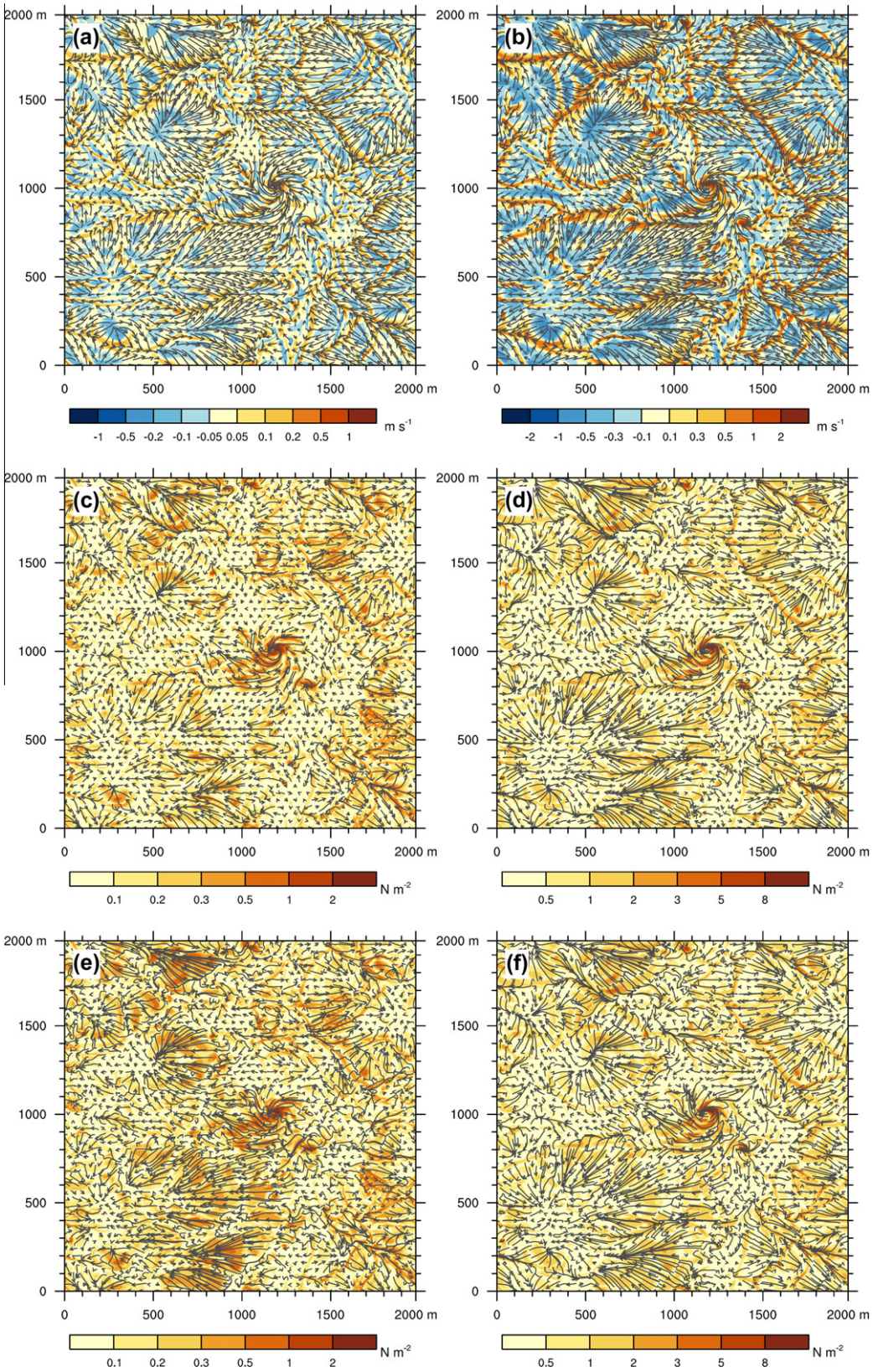

Fig. 4. (a): WRF-LES/D simulated (Exp10, Table 1) vertical velocity fluctuations (color shaded, m s^{-1}) and horizontal wind vectors for the $z = 2$ m level; (b) As (a), but for the $z = 10$ m level; (c) Grid-resolved momentum flux vector, $\vec{\tau}_g$, and its magnitude, τ_g, in N m^{-2} for the $z = 2$ m level; (d) As (c) but for the $z = 10$ m level; (e) and (f) as (c) and (d), but for $\vec{\tau}_f$ and τ_f.

now use the WRF-LES/D simulations to examine the behavior of τ_f and $p(\tau_f)$. In the bulk of the boundary layer, momentum flux is primarily due to large eddies, such that $\tau_f \approx \tau_g$. The dominant scale of turbulence changes rapidly with height and the momentum flux closer to the surface is primarily due to subgrid-scale eddies, such that $\tau_f \approx \tau_{sg}$. Since τ_{sg} is parameterized using a subgrid closure

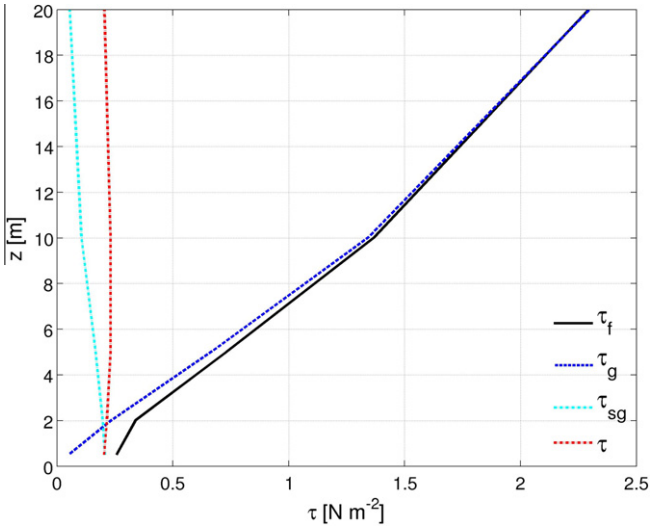

Fig. 5. (a) Profiles of $\bar{\tau}_g, \bar{\tau}_{sg}, \bar{\tau}_f$ and τ from a WRF-LES/D simulation (Exp8, Table 1).

scheme, a question arises whether the subgrid closure correctly produces τ_{sg}. To test the effect of the subgrid closure, we repeated Exp8 with 20 m horizontal resolution. Analysis of $p(\tau_g)$ and $p(\tau_{sg})$ confirm that the unresolved fraction increases slightly as expected. The differences in $p(\tau_g)$ between the model runs with different model resolutions are found to be small. However, the universality of the subgrid closure needs further improvement and the sensitivity of $p(\tau_f)$ to model resolution needs to be further tested.

Fig. 4 shows an example from Exp10 of the turbulent flow fields (mean wind excluded) and the turbulent momentum fluxes at the 2 and 10 m levels. The flow patterns on the two levels (Fig. 4a and b) are similar, characterized by the networks of convergence lines of distinct upward motions and divergence areas of weaker downward motions. At certain junctions of the convergence lines, positively and negatively rotating vortices develop. In comparison with the flow at the 2 m level, turbulence at the 10 m level is more pronounced. Fig 4c and d show the corresponding τ_g and Fig. 4e and f show τ_f. Associated with the turbulent motions, patterns of momentum fluxes emerge, with relatively strong momentum fluxes occurring along the convergence lines, in areas of strong downdrafts and vortices. There are little qualitative differences in the patterns of τ_g and τ_f between the 2 and 10 m levels, although quantitative differences exist. The simulations confirm our hypothesis that large eddies generate patches of strong momentum fluxes which eventually result in intermittent dust emissions.Fig. 5 shows the space-and-time averaged momentum flux profiles of $\bar{\tau}_f$, $\bar{\tau}_g$ and $\bar{\tau}_{sg}$, computed as follows

$$\bar{\tau}_f = \frac{1}{N_x N_y N_t} \sum_{n_x n_y n_t} \tau_f(n_x, n_y, n_t) \tag{14}$$

etc., where N_x (=199) and N_y (=199) are the number of grid points in the x- and y-direction, respectively, and N_t (=361) the time steps of model integration. For comparison, the profile of τ (Reynolds shear stress) is also shown. As expected, τ is almost constant with height. In contrast, $\bar{\tau}_{sg}$ decreases, while $\bar{\tau}_g$ increases, with height. In the upper part of the atmospheric surface layer (e.g., $z > 10$ m), we have $\bar{\tau}_{sg} \ll \bar{\tau}_g$ because turbulence is gradually resolved by the grid. Also $\bar{\tau}_f$ increases with height and deviates significantly from τ.

The deviation $\bar{\tau}_f - \tau$ suggests that the instantaneous turbulent momentum flux substantially differs from the Reynolds shear stress.

Fig. 6 shows $p(\tau_g)$, $p(\tau_{sg})$ and $p(\tau_f)$ for levels z = 0.5, 2, 5, 10, 20, and 40 m for Exp8. It can be seen that the influence of subgrid-scale turbulence on $p(\tau_f)$ decreases with height, because the typical size of turbulence increases and the turbulent eddies are more and more model resolved.

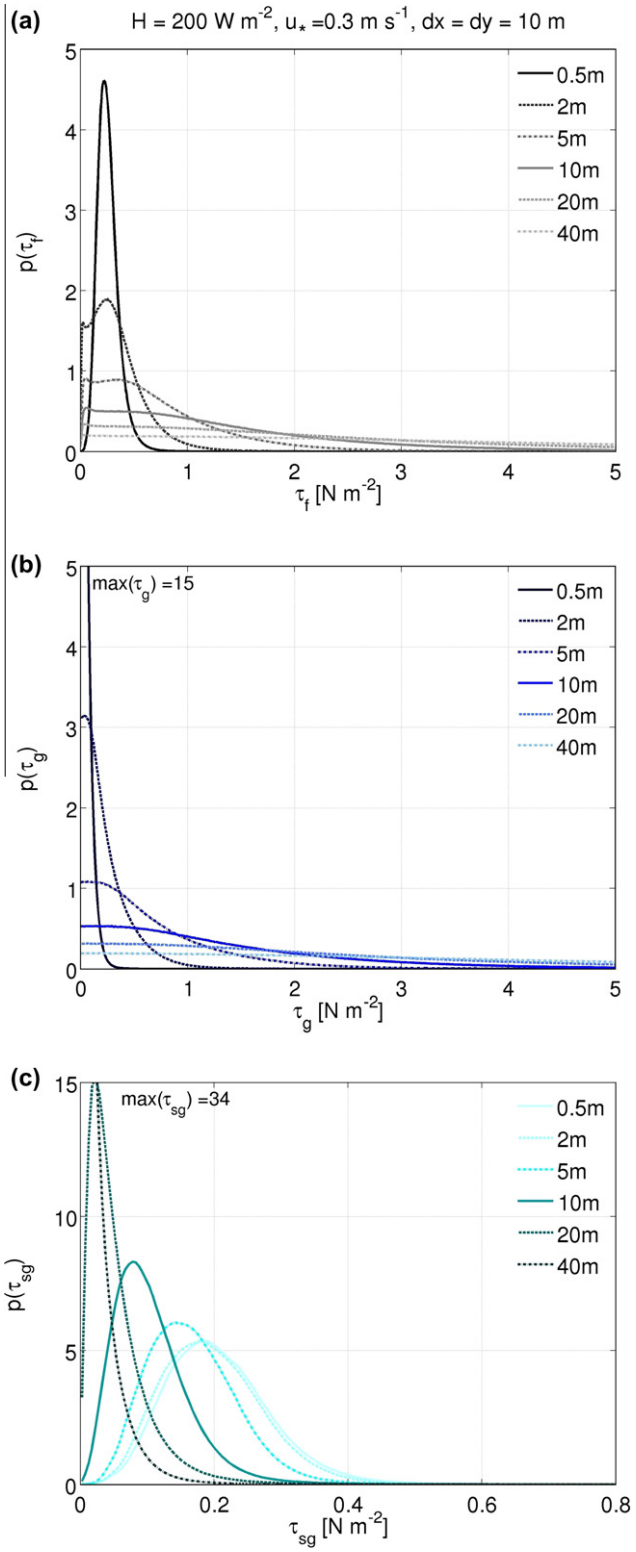

Fig. 6. Probability distribution functions of momentum fluxes τ_f, τ_g and τ_{sg} at the levels of z = 0.5, 2, 5, 10, 20, and 40 m.

Due to the variations of $p(\tau_f)$ with height, we must decide which $p(\tau_f)$ is representative for the surface. Two choices appear to be plausible. The first choice is to find a level close to the surface,

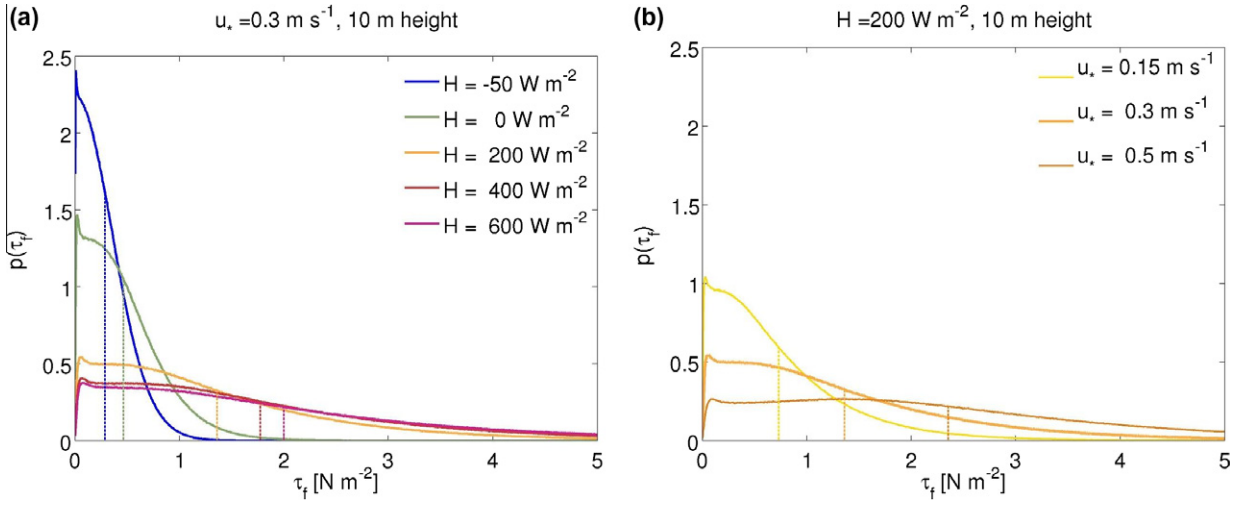

Fig. 7. Probability distribution functions of momentum fluxes for $z = 10$ m for (a) constant u_* but varying H, and (b) constant H but varying u_*. The mean values of τ_f are indicated by dashed lines. Exp8 ($H = 200$ W m^{-2}, $u_* = 0.3$ m s^{-1}) can be used as reference for comparison between Figs. (a) and (b).

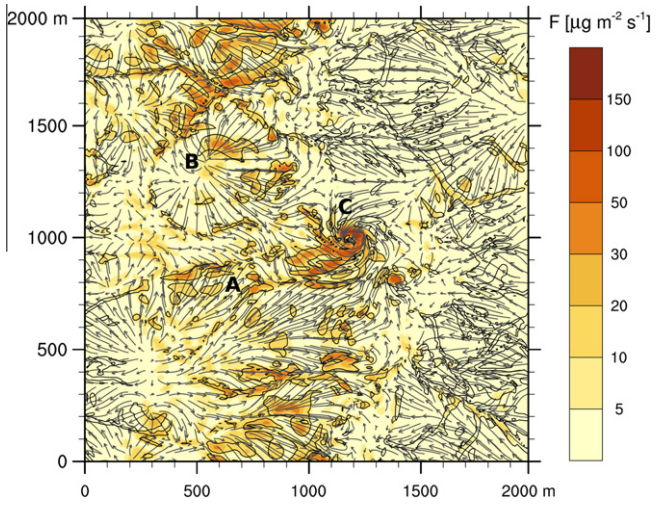

Fig. 8. Turbulent wind speed (vectors, in m s^{-1}) and turbulent instantaneous momentum flux of $\tau_f = 1$ N m^{-2} (contour) at 10 m height together with turbulent dust emission (shaded, μg m^{-2} s^{-1}).

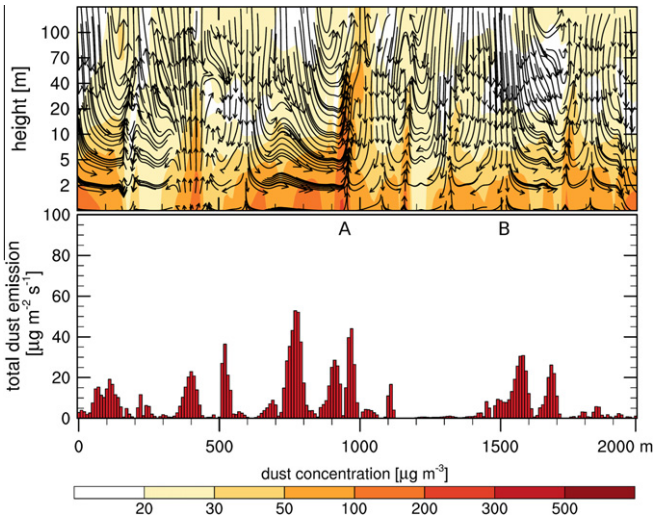

Fig. 9. (Top) Cross-section ($y = 90$) of dust concentration (shaded in μg m^{-3}) and velocity vectors (u', w') in m s^{-1}. (Bottom) dust emission at $y = 90$ (in N m^{-2}). At locations A and B, dust emissions related to updrafts and downdrafts are significant.

where the interactions between atmosphere and land-surface are immediate, e.g. at 2 m height. The problem at such a low height is that large eddies are not fully developed and the surface response time may be too large for the particles to react on the fluctuations induced by micro-scale turbulence. The second choice is to choose a level at which large eddies are well developed and are the main momentum conveyors. In this study, we take 10 m as the reference level, where the effect of subgrid closure is small. The justification for this choice is that the time scale of the eddies prevalent on this level is sufficiently large, such that the flow on this time scale is at local equilibrium with the surface. Another advantage of using the 10 m level is that it is approximately the lowest level of regional weather and global climate models. However, some uncertainties remain and several difficult issues are yet to be fully clarified. The essence of the problem lies in the lack of understanding how τ_f varies with height close to the surface. While the Reynolds averaged momentum flux, τ, is often assumed to be constant with height, τ_f in general increases with height as Fig. 5 shows. Our large-eddy simulation cannot provide a conclusive answer to this question, because in the model, the momentum flux near the surface is parameterized and the parameterization schemes cannot correctly reproduce the probability distribution of the instantaneous momentum fluxes, because these schemes are designed to reproduce the mean value of the momentum flux. A possible consequence of using the instantaneous momentum flux at the 10 m level may be an overestimated momentum flux at the surface. But this choice must be qualitatively correct, as Fig. 4 confirms. It is also noted that the dust emission scheme includes a model parameter α_N, which is provisionally estimated by Klose and Shao (2012), but needs to be verified with observed data. Thus, at this stage of our work, α_N also contains the uncertainty in the choice of the reference level. Fig. 7 shows the dependency of $p(\tau_f)$ on u_* and H for $z = 10$ m. The magnitudes and variances of τ_f increase with H for given u_* (Fig. 7a). Under stable conditions, turbulence is suppressed and τ_f is confined to small values and under more unstable conditions, turbulence is enhanced and τ_f obtains large values. This implies that for given mean wind, convective turbulence enhances dust emission. The magnitudes and variances of τ_f also increase with u_* for given H, as expected.

Klose and Shao (2012) proposed a turbulent dust emission scheme. The theoretic basis of their scheme is as described in Section 2, but the parameterization of the instantaneous surface shear stress follows the method of Manomaiphiboon and Russell (2003) and Koehler and Symanowski (1995). The latter technique derives the joint pdf [e.g. joint pdf of (u', w')] from the marginal distributions (e.g. pdfs of u' and w'). The marginal distributions can be approximated by using the Monin–Obukhov similarity laws. While this technique is useful, it is too time consuming to be applicable to regional and global dust modeling. Based on the large-eddy simulation, $p(\tau_f)$ are found to be empirical functions of u_* and w_* (not shown), and these empirical functions can be directly used in Eq. (8) for estimating turbulent dust emission.

3. Turbulent dust emission

The simulations show that large eddies can produce significant dust emission over fractions of the land surface. Fig. 8 is a snap shot of CTDE simulated in Exp10. As seen, dust emissions occur along updraft convergence lines (Fig. 8, area A), at downdraft centers (Fig. 8, area B), and in areas of vortices (Fig. 8, area C).

The process of dust emission by large eddies can be more clearly seen from Fig. 9. Fig. 9 shows a vertical cross section of dust concentration together with the velocity vectors (u', w') (top), and the corresponding dust emission (bottom). Close to the surface, vertically rotating vortices (vorticity component in y-direction) exist, and relatively strong updrafts and downdrafts are evident. Both updrafts and downdrafts produce dust emissions, e.g., at locations A and B. The near-surface dust concentration associated with the convective dust emission for a typical case is about 100–200 μg m^{-3} and the typical dust emission rate is of the order of magnitude of 10^1 μg m^{-2} s^{-1}. It is further seen from Fig. 9 that large eddies, due to their cohesive structure, can effectively carry dust to the upper levels of the atmospheric boundary layer.

Dust emission is itself a stochastic variable that obeys a probabilistic distribution. Fig. 10 shows the distributions of turbulent dust emission, F, for the numerical experiments listed in Table 1, averaged over 361 samples (snap shots every 10 s over a period of 60 min). Using the simulated data, we have computed the statistic moments of F, e.g. its mean, $\bar{F}$, and standard deviation, σ_F (Table 3). For example, $\bar{F}$ is 9.26 μg m^{-2} s^{-1} and σ_F 13.32 μg m^{-2} s^{-1} for Exp8. F is found to be approximately Weibull distributed, i.e.,

$$p(F) = \frac{\alpha}{\beta}\left(\frac{F}{\beta}\right)^{\alpha-1}\exp\left(-\left[\frac{F}{\beta}\right]^{\alpha}\right) \tag{15}$$

with shape parameter α and scale parameter β (α, $\beta > 0$). The pdf of F can be approximated with a Weibull distribution according to Eq. (15) (Fig. 10). The Weibull distribution parameters are given in Table 3. The shape parameter α is found to be nearly constant ($\alpha \approx 0.8$) for all atmospheric stability and background-wind conditions. In contrast, the scale parameter, β, increases both with wind shear and with instability, except for the stable cases (Exp 1–3), for which β decreases with u_*.

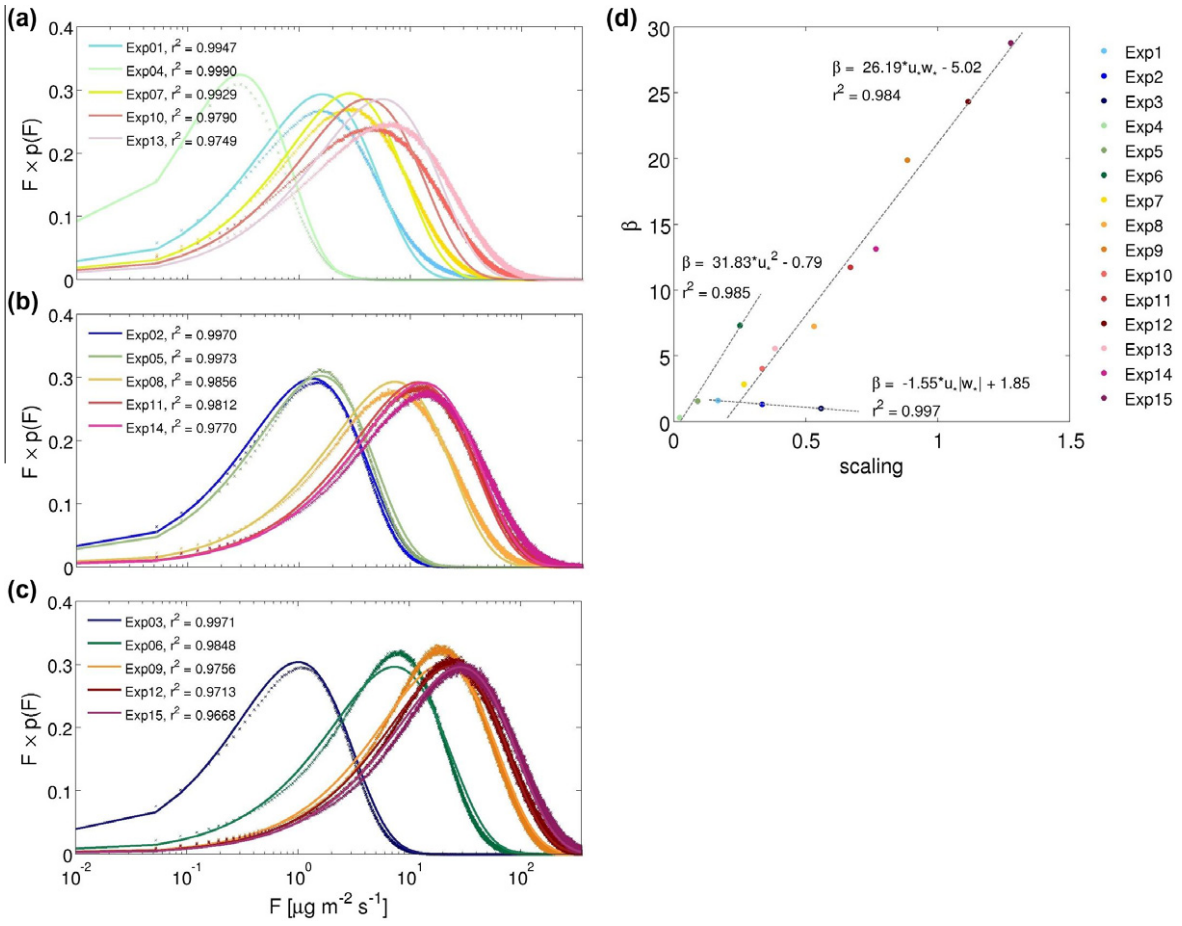

Fig. 10. (a) Probability distributions of dust emission flux averaged over 361 time steps of simulation time (crosses) and fitted Weibull distributions (Eq. (15), lines) for the 5 experiments with u_* = 0.15 m s^{-1} plotted $F \times p(F)$ versus F. (b) and (c) as (a) but for u_* = 0.3 and 0.5 m s^{-1}. The coefficients of determination (r^2) are given for each fitting. (d) Dependency of scale parameter β on u_*w_* for convective cases (Exp 7–15), on $u_*|w_*|$ for stable conditions (Exp 1–3), and on u_*^2 for neutral cases together with weighted linear regressions.

Table 3
Statistics of dust emission for all numerical experiments.

Name	$\bar{F}$ ($\mu g\,m^{-2}\,s^{-1}$)	σ_F ($\mu g\,m^{-2}\,s^{-1}$)	α	β ($\mu g\,m^{-2}\,s^{-1}$)
Exp1	2.08	3.54	0.797	1.607
Exp2	1.36	1.68	0.810	1.317
Exp3	1.02	1.23	0.825	0.999
Exp4	0.28	0.35	0.882	0.294
Exp5	1.58	1.91	0.822	1.554
Exp6	7.70	9.15	0.805	7.324
Exp7	3.63	5.39	0.800	2.844
Exp8	9.26	13.32	0.797	7.247
Exp9	20.96	24.45	0.815	19.879
Exp10	6.24	10.24	0.776	4.035
Exp11	14.53	19.89	0.794	11.730
Exp12	27.96	35.04	0.809	24.313
Exp13	8.47	13.70	0.776	5.562
Exp14	17.40	25.05	0.791	13.141
Exp15	34.44	44.08	0.803	28.764

To demonstrate the relation of scale parameter β to the macroscopic atmospheric control parameters, β is plotted against the product of friction velocity and convective velocity scale, $u_* w_*$ (Fig. 10d). A simple linear relationship is found. Some exceptions must be made for stable/neutral conditions, as the formally computed w_* is negative/zero in these cases. For stable conditions, the absolute value of w_* is used for simplicity, whereas for neutral cases, a linear relationship between β and ${u_*}^2$ is shown.

4. Conclusion

We have argued that convective turbulent dust emission is an important process that must be considered in dust emission parameterization. The mechanism of turbulent dust emission differs from the other dust emission mechanisms, such as saltation bombardment and aggregates disintegration, considered in "traditional" dust emission schemes. Our hypothesis is that under certain background atmospheric and land-surface conditions, large eddies develop and generate sporadic momentum fluxes which produce patchy and intermittent dust emission. While the strength, size, and number of the large eddies are difficult to quantify, their impact on dust emission can be statistically evaluated from the model simulations. On this basis, it is possible to express turbulent dust emission in terms of a small number of environmental control parameters.

We have developed a large-eddy dust model, WRF-LES/D, by coupling the WRF large-eddy model with a new dust module. WRF-LES/D has been applied to simulating turbulence and dust emission for various stability and background-flow conditions for a given soil surface. These simulations enabled us to examine how turbulent dust emission occurs, to quantify the instantaneous shear stress generated by convective eddies and to estimate the order of magnitude and range of variations of dust emission.

We have demonstrated that the instantaneous momentum flux on the surface, τ_f, obeys a probability distribution function, $p(\tau_f)$. The introduction of instantaneous momentum flux, regardless of its direction, in dust modeling is new with respect to the use of a threshold friction velocity u_* in traditional dust emission schemes.

The numerical results confirmed that large eddies can produce significant dust emissions. Under convective conditions, dust emissions occur along updraft convergence lines, at downdraft centers and in areas of vortices. It is found that the near-surface dust concentration due to turbulent dust emission is of the order $10^2\ \mu g\,m^{-3}$ and the typical dust emission rate is of the order 10^1–$10^2\ \mu g\,m^{-2}\,s^{-1}$. Due to the cohesive structure of convective turbulence, dust emitted can be effectively carried to the upper levels of the atmospheric boundary layer. While turbulent dust emission is a stochastic variable, its statistical moments are simply related to the control parameters. We have shown that for a given soil type, turbulent dust emission is a function of u_* and w_*.

The estimated magnitude is subject to the verification of field observations, because we have used in our simulation several parameters which have uncertainties. One of these lies in the choice of the momentum flux reference level (10 m in this study) and another in the parameter α_N in Eq. (7). These uncertainties affect the quantitative estimates of turbulent dust emission, although less so its nature and spatial patterns. Also, the specification of particle cohesive forces is subject to uncertainties. The improvement of our proposed scheme premises reliable future measurements.

References

Alfaro, S.C., Gomes, L., 2001. Modeling mineral aerosol production by wind erosion: emission intensities and aerosol size distributions in source areas. J. Geophys. Res. 106 (D16), 18075–18084.

Bagnold, R.A., 1941. The Physics of Blown Sand and Desert Dunes. Methuen, London, p. 265.

Balme, M., Greeley, R., 2006. Dust devils on Earth and Mars. Rev. Geophys. 44, RG3003. http://dx.doi.org/10.1029/2005RG000188.

Chen, F., Mitchell, K., Schaake, J., Xue, Y., Pan, H., Koren, V., Duan, Y., Ek, M., Betts, A., 1996. Modeling of land-surface evaporation by four schemes and comparison with FIFE observations. J. Geophys. Res. 101, 7251–7268.

Chen, F., Dudhia, J., 2001. Coupling an advanced land surface-hydrology model with the Penn State-NCAR MM5 modeling system. Part I: Model implementation and sensitivity. Mon. Wea. Rev. 129, 569–585.

Darmenova, K., Sokolik, I.N., Shao, Y., Marticorena, B., Bergametti, G., 2008. Development of a physically-based dust emission module within the weather research and forecasting (WRF) model: assessment of dust emission parameterizations and input parameters for source regions in Central and East Asia. J. Geophys. Res. 114, D14201. http://dx.doi.org/10.1029/2008JD011236.

Deardorff, J.W., 1970. A numerical study of three-dimensional turbulent channel flow at large Reynolds numbers. J. Fluid Mech. 41, 453–480. http://dx.doi.org/10.1017/S0022112070000691.

Greeley, R., Whelley, P.L., Arvidson, R.E., Cabrol, N.A., Foley, D.J., Franklin, B.J., Geissler, P.G., Golombek, M.P., Kuzmin, R.O., Landis, G.A., Lemmon, M.T., Neakrase, L.D., Squyres, S.W., Thompson, S.D., 2006. Active dust devils in Gusev crater, Mars: observations from the Mars Exploration Rover Spirit. J. Geophys. Res. 111, E12S09. http://dx.doi.org/10.1029/2006JE002743.

Kanak, K.M., 2005. Numerical simulation of dust devil-scale vortices. Q. J. R. Meteorol. Soc. 131, 1271–1292. http://dx.doi.org/10.1256/qj.03.172.

Kanak, K.M., Lilly, D.K., Snow, J.T., 2000. The formation of vertical vortices in the convective boundary layer. Q. J. R. Meteorol. Soc. 126, 2789–2810.

Klose, M., Shao, Y., 2012. Stochastic parameterization of dust emission and application to convective atmospheric conditions. Atmos. Chem. Phys. Discuss. 12, 3263–3293. http://dx.doi.org/10.5194/acpd-12-3263-2012.

Koehler, K.J., Symanowski, J.T., 1995. Constructing multivariate distributions with specific marginal distributions. J. Multivariate Anal. 55, 261–282.

Kok, J.F., 2011. Does the size distribution of mineral dust aerosols depend on the wind speed at emission? Atmos. Chem. Phys. 11, 10149–10156. http://dx.doi.org/10.5194/acp-11-10149-2011.

Kosović, B., 1997. Subgrid-scale modelling for the large-eddy simulation of high-Reynolds-number boundary layers. J. Fluid Mech. 336, 151–182.

Lilly, D.K., 1967. The representation of small-scale turbulence in numerical experiment. In: Proc. IBM Scientific Computing Symposium on Environmental Sciences. White Plains, NY, pp. 195–210.

Maher, B.A., Prospero, J.M., Mackie, D., Gaiero, D., Hesse, P., Balkanski, Y., 2010. Global connections between aeolian dust, climate and ocean biogeochemistry at the present day and at the last glacial maximum. Earth Sci. Rev. 99 (1–2), 61–97. http://dx.doi.org/10.1016/j.earscirev.2009.12.001.

Mahowald, N., Engelstaedter, S., Luo, A., Sealy, A., Artaxo, P., Benitez-Nelson, C., Bonnet, S., Chen, Y., Chuang, P.Y., Cohen, D.D., Dulac, F., Herut, B., Johansen, A.M., Kubilay, N., Losno, R., Maenhaut, W., Paytan, A., Prospero, J.M., Shank, L.M., Siefert, R.L., 2009. Atmospheric iron deposition: global distribution, variability, and human perturbations. Annu. Rev. Mar. Sci. 2009 (1), 245–278.

Manomaiphiboon, K., Russell, A.G., 2003. Formulation of joint probability density functions of velocity for turbulent flows: an alternative approach. Atmos. Environ. 37, 4917–4925. http://dx.doi.org/10.1016/j.atmosenv.2003.08.022.

Marticorena, B., Bergametti, G., 1995. Modelling the atmospheric dust cycle: 1. Design of a soil-derived dust emission scheme. J. Geophys. Res. 100, 16415–16430.

Michaels, T.I., Rafkin, S.C., 2004. Large eddy simulation of atmospheric convection on Mars. Q. J. R. Meteorol. Soc. 130, 1251–1274.

Mirocha, J.D., Lundquist, J.K., Kosovic, B., 2010. Implementation of a nonlinear subfilter turbulence stress model for large-eddy simulation in the advanced research WRF model. Mon. Wea. Rev. 138, 4212–4228. http://dx.doi.org/10.1175/2010MWR3286.1.

Moeng, C.-H., Dudhia, J., Klemp, J., Sullivan, P.S., 2007. Examining two-way grid nesting for large eddy simulation of the PBL using the WRF model. Mon. Weather Rev. 135, 2295–2311.

Ohno, H., Takemi, T., 2010. Mechanisms for intensification and maintenance of numerically simulated dust devils. Atmos. Sci. Lett. 11, 27–32. http://dx.doi.org/10.1002/asl.249.

Reinfried, F., Tegen, I., Heinold, B., Hellmuth, O., Schepanski, K., Cubasch, U., Huebener, H., Knippertz, P., 2009. Simulations of convectively-driven density currents in the Atlas region using a regional model: impacts on dust emission and sensitivity to horizontal resolution and convection schemes. J. Geophys. Res. 114, D08127. http://dx.doi.org/10.1029/2008JD010844.

Shao, Y., 2004. Simplification of a dust emission scheme and comparison with data. J. Geophys. Res. 109, 372. http://dx.doi.org/10.1029/2003JD004.

Shao, Y., 2008. Physics and Modelling of Wind Erosion. Springer Verlag.

Shao, Y., Raupach, M.R., Flindlater, P.A., 1993. Effect of saltation bombardment on the entrainment of dust by wind. J. Geophys. Res. 98, 12719–12726.

Shao, Y., Liu, S.F., Schween, J., Crewell, S., submitted for publication. Large-eddy atmosphere–land surface modeling over heterogeneous surfaces: model development and comparison with measurements. Boundary-Layer Meteorol.

Skamarock, W.C., Klemp, J.B., Dudhia, J., Gill, D.O., Barker, D.M., Duda, M.G., Huang, X.Yu., Wang, W., Powers, J.G. 2008. A Description of the Advanced Research WRF Version 3, NCAR Tech. Note, NCAR/TN-475+STR, 113.

Tanaka, T.Y., Chiba, M., 2006. A numerical study of the contributions of dust source regions to the global dust budget. Global Planet. Change 52, 88–104.

Uno, I., Eguchi, K., Yumimoto, K., Takemura, T., Shimizu, A., Uematsu, M., Liu, Z., Wang, Z., Hara, Y., Sugimoto, N., 2009. Asian dust transported one full circuit around the globe. Nat. Geosci. 2, 557–560.

Zender, C.S., Bian, H., Newman, D., 2003. Mineral dust entrainment and deposition (DEAD) model: description and 1990s dust climatology. J. Geophys. Res. 108, 4416. http://dx.doi.org/10.1029/2002JD002775.

Zimon, A.D., 1982. Adhesion of Dust and Powde. Consultants Bureau, New York, USA.

4 CTDE scheme improvement and evaluation

Reference:

Klose, M., Y. Shao, X. L. Li, H. S. Zhang, M. Ishizuka, M. Mikami, and J. F. Leys (2014a), Further development of a parameterization for convective turbulent dust emission and evaluation based on field observations, *J. Geophys. Res. Atmos.*, *119*, 10,441–10,457, doi: 10.1002/2014JD021688

AGU PUBLICATIONS

JGR

Journal of Geophysical Research: Atmospheres

RESEARCH ARTICLE

10.1002/2014JD021688

Key Points:
- Further developments of a convective turbulent dust emission (CTDE) scheme
- A new statistical description of instantaneous momentum flux
- Correction functions for soil moisture and surface roughness effects on CTDE

Correspondence to:
M. Klose,
mklose@uni-koeln.de

Citation:
Klose, M., Y. Shao, X. Li, H. Zhang, M. Ishizuka, M. Mikami, and J. F. Leys (2014), Further development of a parameterization for convective turbulent dust emission and evaluation based on field observations, *J. Geophys. Res. Atmos.*, *119*, 10,441–10,457, doi:10.1002/2014JD021688.

Received 4 MAR 2014
Accepted 14 AUG 2014
Accepted article online 18 AUG 2014
Published online 11 SEP 2014

Further development of a parameterization for convective turbulent dust emission and evaluation based on field observations

Martina Klose[1], Yaping Shao[1], Xiaolan Li[2], Hongsheng Zhang[2], Masahide Ishizuka[3], Masao Mikami[4], and John F. Leys[5]

[1]Institute for Geophysics and Meteorology, University of Cologne, Cologne, Germany, [2]Laboratory for Climate and Ocean-Atmosphere Studies, Department of Atmospheric and Ocean Sciences, School of Physics, Peking University, Beijing, China, [3]Faculty of Engineering, Kagawa University, Takamatsu, Japan, [4]Meteorological Research Institute, Japan Meteorological Agency, Tsukuba, Japan, [5]Scientific Services Division, Office of Environment and Heritage, Department of Premier and Cabinet, Gunnedah, New South Wales, Australia

Abstract Further developments of a parameterization scheme for convective turbulent dust emission (CTDE) are presented. The scheme is advanced by including (1) a new statistical description of instantaneous momentum flux, (2) a correction function for cohesive force to account for the effect of soil moisture, and (3) a correction function for lifting force to consider the effect of vegetation roughness elements. The probability density function describing instantaneous momentum flux is now derived from large-eddy simulations for different atmospheric stabilities. The vegetation correction function is based on a drag partition theory. Additional improvements on the representations of interparticle cohesive force and particle size distribution are introduced. The new CTDE scheme is tested against the field data obtained at a sand storm monitoring station in the Horqin Sandy Land in China in 2011 and during the Japan-Australia Dust Experiment in Australia in 2006.

1. Introduction

Three dust emission mechanisms have been recognized [*Shao*, 2008]: saltation bombardment, aggregates disintegration, and aerodynamic entrainment. In the situation of strong mean wind, the first two mechanisms are efficient and most important. Several dust emission parameterization schemes already exist for one or both of these two mechanisms, e.g., the schemes of [*Marticorena and Bergametti*, 1995] or [*Shao*, 2004]. Direct aerodynamic dust entrainment was neglected in earlier studies [e.g., *Alfaro and Gomes*, 2001; *Zender et al.*, 2003; *Kok and Renno*, 2009]. This is justified if we consider dust emission in episodic dust storm events when the amount of dust emitted by direct entrainment may be of orders of magnitude smaller than that by saltation bombardment [*Loosmore and Hunt*, 2000]. However, the long-term contribution of recurrent aerodynamic dust entrainment may be substantial. Recently, effort has been made to investigate the process of Convective Turbulent Dust Emission (CTDE), the most important form of aerodynamic dust entrainment [*Klose and Shao*, 2013]. Field experiments have been carried out to investigate CTDE among other processes [e.g., *Heintzenberg*, 2008; *Chkhetiani et al.*, 2012]. *Ansmann et al.* [2008] analyzed the vertical profiles of convective dust plumes by use of lidar measurements of the Saharan Mineral Dust Experiment (SAMUM) in Morocco and suggested that convective processes play an important role in dust production, particularly at low mean wind speeds (< 7 m s^{-1}). *Allen et al.* [2013] studied the relative importance of dust generation mechanisms in central Sahara in the Fennec project and attributed 1–2% of dust emission to dry convective plumes. This reported low value may be related to the fact that no dust devils, a category of "dry convective plumes", were detected at the Fennec site [*Allen et al.*, 2013]. In addition, the latter authors classified 51% of the measurement time (or 13% using total nephelometer scattering) as background dust. In fact, part of the "background dust" might be due to CTDE although not in form of dust plumes. From the modeling perspective, very few studies have focused on CTDE. *Ito et al.* [2010] conducted large-eddy simulations (LES) and used the empirical relation of *Loosmore and Hunt* [2000] to estimate CTDE. *Descamps et al.* [2005] introduced a pavement model in which the temporal evolution of the surface particle size distribution is considered. The latter authors applied probability density functions for aerodynamic lift and particle cohesive forces. The first comprehensive CTDE model was proposed by *Klose and Shao* [2012]. In a follow-up work, *Klose and Shao* [2013] developed a large-eddy dust model, WRF-LES/D, by coupling the Weather

Research and Forecasting (WRF) large-eddy flow model with the new CTDE scheme. This model was used to investigate the CTDE processes in detail. The studies of *Klose and Shao* [2012, 2013] are the basis for the improved CTDE parameterization presented in this study. The model is advanced in that (1) a new statistical description of instantaneous momentum flux, which is crucial for turbulent dust uplift, is obtained based on the simulation results of WRF-LES/D (2) a correction function for soil moisture effects on dust emission is included; and (3) a correction function for the influence of vegetation roughness elements on particle lifting is introduced. Further improvements of the representations of cohesive force and particle size distribution are presented. Tests for model sensitivity on soil moisture and vegetation cover are performed. The model is calibrated and validated with field data from a sand storm monitoring station in the Horqin Sandy Land in China in 2011 [*Li et al.*, 2014] and from the Japan-Australia Dust Experiment (JADE) conducted in Australia in 2006 [*Ishizuka et al.*, 2008, 2014]. For calibration, the data are selected from the time periods which satisfy the criteria for CTDE events.

The CTDE theory is described in section 2. The new statistical representation of instantaneous momentum flux is presented in section 3 followed by the dust model evaluation in section 4. Subsequently, the model sensitivity on the cohesive force parameterization and the correction methods to account for soil moisture and vegetation cover effects are detailed in section 5. The study is concluded in section 6.

2. Convective Turbulent Dust Emission Scheme

The dust emission scheme of *Klose and Shao* [2012, 2013] captures the stochastic nature of the processes involved in CTDE by parameterizing both aerodynamic lifting force and interparticle cohesive force using probability density functions (pdfs). The dust emission flux is given as

$$\tilde{F} = \begin{cases} \frac{\alpha_N}{2D}\left\{-w_t m_p + T_p\left(f - f_i\frac{d}{D}\right)\right\} & \text{for } f > f_t, \\ 0 & \text{else} \end{cases} \tag{1}$$

for a given lifting force f and cohesive force f_i. T_p is the particle response time, d particle diameter, D viscous sublayer thickness, m_p particle mass, and w_t the particle terminal velocity. As shown in *Klose and Shao* [2012], $\alpha_N = N_p D$, with N_p being particle number concentration. Thus, α_N has the dimensions of [m^{-2}] and can be interpreted as the over D integrated particle number concentration per unit area. The value of α_N is unknown, but its characteristics can be specified. Suppose during a CTDE, a unit volume (V1) adjacent to the surface is filled with particles of diameter d_1 and another (V2) with particles of size $d_2 > d_1$. All particles have the same density. A plausible assumption is that the total mass of dust in V1 is equal to that in V2, and thus, $N_p\,(V1)\,d_1^3 = N_p\,(V2)\,d_2^3$. Accordingly, α_N decreases with particle size as

$$\alpha_N = \alpha_{N0}\left(\frac{d}{d_{\text{ref}}}\right)^{-3} \tag{2}$$

with α_{N0} being an empirical constant of dimensions [m^{-2}] and d_{ref} the particle size for which the scheme is calibrated, e.g., 10 μm.

CTDE is initiated only if f exceeds the retarding force $f_t = f_i + m_p g$, where g is the gravitational acceleration. The dust emission flux for a given particle size d_j can be calculated as

$$F_j = \int_0^{\infty}\left[\int_0^{f}\tilde{F}\cdot p_j\left(f_i\right)\mathrm{d}f_i\right]p\left(f\right)\mathrm{d}f, \tag{3}$$

with $p_j(f_i)$ being the pdf of $f_i(d_j)$ and $p(f)$ that of f, and finally, the total dust emission flux is

$$F = \int_0^{d_{\max}} F_j \cdot p_A\left(d_j\right)\delta d_j \tag{4}$$

where $d_{\max}$ is the maximum dust particle diameter (20 μm in the current model version) and $p_A(d_j)$ the area particle size distribution (psd). δ indicates the differential. Note that p_A is used instead of mass psd, p_M, because the surface shear stress acts on particle area instead of particle volume. $p_M(d_j)$ is the one usually directly available from particle size analysis, but for given p_M, p_A can be estimated as

$$p_A\left(d_j\right) = \frac{p_M\left(d_j\right)}{d_j}\left[\sum_{k=1}^{K}\frac{p_M\left(d_k\right)\delta d_k}{d_k}\right]^{-1}. \tag{5}$$

For the Horqin and JADE sites, $p_M(d_j)$ can be found in *Li et al.* [2014] and *Shao et al.* [2011], respectively. The JADE soil type is loamy sand, while the Horqin soil type is sand. Only the minimally dispersed psds are used in the CTDE model, as the relatively weak winds produce little disturbance to the soil.

The interparticle cohesive force is assumed to satisfy a log-normal distribution

$$p\left(f_i\right) = \frac{1}{f_i\sqrt{2\pi}\sigma_{f_i}} \exp\left(-\frac{\left(\ln f_i - \ln \bar{f}_i\right)^2}{2\sigma_{f_i}^2}\right) \tag{6}$$

and the mean value $\bar{f}_i$ and standard deviation σ_{f_i} are estimated with

$$\bar{f}_i = \vartheta d \tag{7}$$

$$\sigma_{f_i} = 4.11 - 0.05d \tag{8}$$

with $\bar{f}_i$ and σ_{f_i} in 10^{-8} N, d in μm, and $\vartheta = 10^2\vartheta_0$ being a coefficient ($[\vartheta] = [\vartheta_0] = \mathrm{kg\,s^{-2}}$). The factor of 10^2 arises from conversion of m in μm and of N in 10^{-8} N. This conversion is necessary for consistency with equation (8), suggested in *Shao* [2008] based on a small data set of *Zimon* [1982].

Equation (7) follows *Shao and Lu* [2000]. In their derivation for threshold friction velocity for saltation, u_{*t}, the latter authors found a parameter γ to be in the range of 1.65×10^{-4} to 5×10^{-4} kg s^{-2}. It follows that ϑ_0 ranges between 0.86×10^{-4} and 2.62×10^{-4} kg s^{-2}. This range is consistent with the values suggested by *Corn* [1961] and *Phillips* [1980]. On this basis, we select $\vartheta_0 = 1.6 \times 10^{-4}$ kg s^{-2}.

The estimates of the parameters for equation (8) have, due to the small sample size of the underlying data, large uncertainties which cannot be well quantified due to our limited knowledge on the cohesive force. To evaluate the dust flux uncertainties arising from f_i, a sensitivity experiment will be conducted (section 5.1).

3. Parameterization of Instantaneous Momentum Flux

The aerodynamic lifting force, f, is proportional to instantaneous momentum flux, τ_f, and we estimate $p(f)$ by parameterizing the pdf of τ_f, $p(\tau_f)$. The Reynolds shear stress is not used here, because it is typically averaged over a time interval of 20–30 min and therefore does not capture the instantaneous shear stress responsible for turbulent dust uplift. In *Klose and Shao* [2012], $p(\tau_f)$ was determined as the joint pdf of turbulent wind speed components u', v', and w', $u' = u - \overline{u}$, etc., and made use of the Monin-Obukhov similarity theory (MOST). This method is, however, computationally costly and subject to the validity of the MOST assumptions. In *Klose and Shao* [2013], large-eddy simulation (LES) was used to investigate the behavior or τ_f and the corresponding dust emissions for various atmospheric stability conditions. Based on the model simulations, a new method is proposed for estimating $p(\tau_f)$ for given atmospheric stabilities. In this method, $p(\tau_f)$ depends both on friction velocity u_* and convective velocity w_*, such that the effects of shear-generated and buoyancy-generated turbulence on τ_f are accounted for. Also, the Obukhov length, L, is used as a measure of stability.

Using the LES simulations, we calculate $p(\tau_f)$ at 10 m height for various stabilities [*Klose and Shao*, 2013], where τ_f is given by

$$\tau_f = \rho\sqrt{\left(u'w' + \frac{1}{\rho}\tau_{\mathrm{sg,x}}\right)^2 + \left(v'w' + \frac{1}{\rho}\tau_{\mathrm{sg,y}}\right)^2} \tag{9}$$

with $\tau_{\mathrm{sg,x}}$ and $\tau_{\mathrm{sg,y}}$ being the subgrid momentum flux components, which are, in the LES simulations, computed using a turbulent kinetic energy based nonlinear backscatter and anisotropy subfilter-scale stress parameterization [*Kosovic*, 1997; *Mirocha et al.*, 2010]. By using u', v', and w' instead of u, v, and w, only the variance of τ_f needs to be considered.

We recognize that $p(\tau_f)$ is height dependent, but τ_f at the surface must be proportional to τ_f at some level above the ground. The 10 m level is chosen, as large-eddies on this level are sufficiently developed and data (measurements or simulations) are most readily available for CTDE modeling. For more details, see *Klose and Shao* [2013].

Three different types of distributions were tested to find the most suitable fitting for $p(\tau_f)$, namely, the Weibull, Gamma, and Frechét distributions:

$$p_W(x) = \frac{\alpha}{\beta}\left(\frac{x}{\beta}\right)^{\alpha-1} \exp\left[-\left(\frac{x}{\beta}\right)^{\alpha}\right] \tag{10}$$

$$p_G(x) = \frac{1}{\beta^{\alpha}\Gamma(\alpha)} x^{\alpha-1} \exp\left[-\left(\frac{x}{\beta}\right)\right] \tag{11}$$

$$p_F(x) = \frac{\alpha}{\beta}\left(\frac{x-\zeta}{\beta}\right)^{-1-\alpha} \exp\left[-\left(\frac{x-\zeta}{\beta}\right)^{-\alpha}\right] \tag{12}$$

where α and β are the shape and scale parameter of the respective distributions. Other distribution functions were also tested (e.g., log-normal and Gumbel) but did not perform well and were thus excluded from further discussions. For p_F, the location of the distribution's minimum, ζ, was assumed to be zero. This assumption is reasonable for $p(\tau_f)$ and reduces the degrees of freedom to 2. To develop a similarity theory for $p(\tau_f)$, τ_f needs to be normalized to allow for building of $p(\tau_f)$ groups characteristic for certain atmospheric situations and for establishment of universal $p(\tau_f)$ functions. To reflect both shear- and buoyancy-induced turbulence, u_* and w_* are included in the scaling. Per definition, we have $u_* = \sqrt{\tau_R/\rho}$ and $w_* = \left(\frac{g}{\Theta}\overline{w'\Theta'}_0 z_i\right)^{1/3}$, where Θ is potential temperature, $\overline{w'\Theta'}_0$ surface buoyancy flux, and z_i the boundary layer thickness. The use of a linear combination of u_* and w_* is more advantageous than the use of their product, as the latter approaches zero if either $w_* \approx 0$ or $u_* \approx 0$. This consideration and tests with various combinations resulted in two scaling factors, s_1 and s_2, for the final analysis:

$$s_1 = \rho\left(w_*^2 + m u_*^2\right) \tag{13}$$

$$s_2 = \rho\left(w_*^3 + m u_*^3\right)^{2/3} \tag{14}$$

where m is a weighting coefficient. The fitting to $p(\tau_f)$ was done after τ_f was scaled either with s_1 or s_2 and with m varying from 1 to 50. Even larger values of m would diminish the relevance of w_*. For each m, the mean and the variance of β were calculated for the categories of stable, neutral, and unstable conditions. For each category, the mean of β corresponding to a minimum variance of β, i.e., σ_β^2, is selected for use in the CTDE scheme.

It turned out that the minimum σ_β^2 for the unstable cases is lower for the Frechét distributions than for the Weibull distributions. For the Gamma distributions, no minimum could be found. Only the unstable cases were considered here, as they are of particular interest for CTDE. The optimal scaling to achieve a minimum σ_β^2 is for the Weibull and Frechét distributions:

$$s_W = \rho\left(w_*^3 + 19 u_*^3\right)^{2/3} \tag{15}$$

$$s_F = \rho\left(w_*^3 + 43 u_*^3\right)^{2/3}. \tag{16}$$

The fitting of $p(\tau_f)$ was then redone with τ_f normalized with s_W and s_F, and the scale parameter α was related to atmospheric stability as power of $|z/L|$ with $z = 10$ m. Figures 1a and 1b show α and β derived from the Weibull fitting and the corresponding approximations for $p(\tau_f)$ derived from the 15 LES runs of *Klose and Shao* [2013]. Blue represents the stable conditions (from week to strong wind speeds, Experiments 1–3) and green the neutral conditions (Experiments 4–6). For the remaining experiments, stability was gradually decreased (Experiments 7, 10, 13: yellow to purple), again from weak to strong winds (Experiments 7–9, Experiments 10–12, and Experiments 13–15). As this study is about CTDE, we only selected the unstable cases (Experiments 7–15) for deriving the relation between α and z/L and found that

$$\alpha = 1.05 + 0.17\left|\frac{z}{L}\right|^{-3/4}. \tag{17}$$

Figure 1d shows the pdfs reproduced by equation (17) together with the constant β values as given in Figure 1b. Figure 1a shows that the stable cases are also close to the curve, which has been fitted to the unstable cases only. Thus, equation (17) can also be used to reproduce the stable cases with the only disadvantage of a somewhat decreased accuracy. Neutral conditions cannot be reproduced by equation (17),

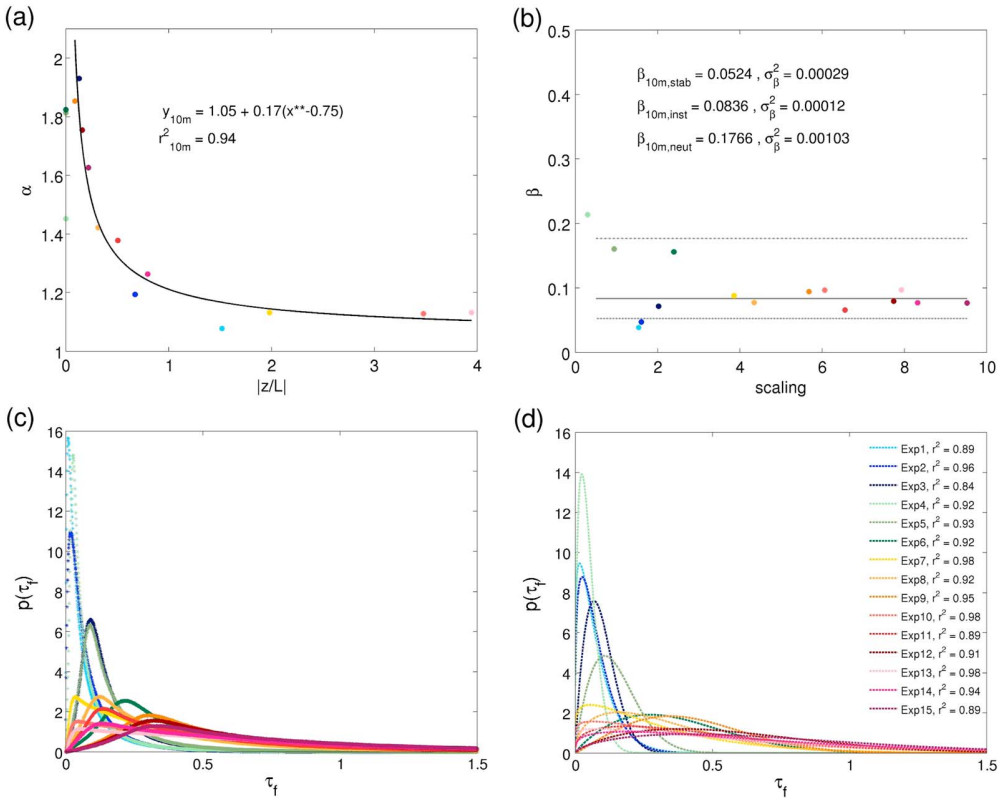

Figure 1. (a) Relationship between the shape parameter α and stability, as represented by $|z/L|$, and the coefficient of determination, r^2. (b) Mean values of the scaling parameter β for different atmospheric stabilities and the corresponding variances σ_β. Probability density functions of instantaneous momentum fluxes (c) obtained from LES and (d) reproduced using Weibull distributions with the parameters obtained from equation (17) and the constant β approximation as shown in Figures 1a and 1b, except for neutral conditions, where the shape parameter has been taken from the fitting directly.

because $z/L \approx 0$. Therefore, the shape parameter obtained by the fitting was directly used for pdf reproduction for the neutral cases (Experiments 4–6) in Figure 1c instead of the approximated α used for stable and unstable conditions. While the Weibull pdfs give somewhat flatter peaks for small τ_f (Figure 1d) compared to the data (Figure 1c), they well reproduced the behavior of the distributions' tails. The results of the Frechét fitting are shown in Appendix A. The shapes of the distributions match better with the original $p(\tau_f)$ for small τ_f, but the probability density was underestimated for large τ_f, especially for very unstable conditions (Figure A1d). Thus, the Weibull distributions were chosen for the CTDE scheme for two reasons:

1. The emphasis of this study is on convective turbulence which is expected to occur under the conditions of weak wind (small u_*) and strong buoyancy (large w_*). For such situations, the Weibull pdfs well represent $p(\tau_f)$ as seen from the large correlation coefficients (Experiments 7, 10, and 13).
2. The intermittently high momentum fluxes are most important for CTDE, which are better reproduced by the Weibull pdfs. With the similarity relationships, we can now estimate $p(\tau_f)$ with input parameters u_*, w_*, and z/L, which are usually available in atmospheric models.

4. Comparison to Field Observations

To enable a general application of the CTDE scheme, the model parameter α_{N0} needs to be determined. Preliminary estimates for α_{N0} exist, e.g., $\alpha_{N0} \approx 800\,\mathrm{m}^{-2}$ obtained by comparison of modeled dust concentrations with lidar observations in the Taklimakan desert [*Klose and Shao*, 2012]. This value is now no longer recommended, because in the latter study, the particle lifting force was calculated based on joint pdfs of turbulent wind speed components and the lidar data had large uncertainties. Also, other model updates have been made since the work of *Klose and Shao* [2012]. Using the new method described in section 3 and in situ observations, more reliable α_{N0} can be estimated. *Li et al.* [2014] used the new version of the scheme and

validated the results against the data collected from a sand storm monitoring station in the Horqin Sandy Land in China in 2011. By investigating five CTDE cases, they found $\alpha_{N0} \approx 10^4\ \mathrm{m}^{-2}$. Measurements were taken for about 1 year at Horqin. To detect more CTDE cases, we additionally analyzed the data of the Japan-Australia Dust Experiment (JADE) conducted in Australia in 2006 [*Ishizuka et al.*, 2008, 2014]. At the JADE site, dust was observed for eight size bins from 0.3 to > 8.4 μm. As recommended by *Ishizuka et al.* [2014], size bins 1 and 8 were excluded from analysis such that a size range from 0.6 to 8.4 μm is used. A 30 min running average was applied to the JADE data. Details on processing of the Horqin data can be found in *Li et al.* [2014]. In the latter work, CTDE events were specified based on three criteria: (1) upward dust flux ($F > 0$), (2) no systematic saltation ($u_* < u_{*t}$), and (3) convective turbulent conditions ($w_* > 0$). By applying these criteria to the two data sets, 18 (14 Horqin and 4 JADE) CTDE cases were identified. Measurements using a SENSIT (a piezoelectric sensor) at the Horqin site and a SPC (sand particle counter) at the JADE site confirm that saltation activities were weak during the selected CTDE cases, but intermittent saltation did occur. Intermittent saltation may occur even if u_* is below u_{*t} [*Stout and Zobeck*, 1997]. We cannot exclude the possibility that intermittent saltation generates dust emission but this mechanism must be considered to be part of the stochastic dust emission process.

All cases were modeled with the new CTDE scheme with α_{N0} initially set to 1. Figure 2 shows the time series and scatterplots of the observations and the model results for four of the Horqin cases. At Horqin, fluxes of dust particles with diameters < 10 μm were estimated from the PM10 concentration profile measurements. The time series of the modeled fluxes were obtained by multiplying the model results (with $\alpha_{N0} = 1$) by an α_{N0} determined from the observed-to-modeled dust-flux ratio shown in the scatterplots. As seen, there is a good agreement between the model predictions and observations and the temporal evolutions match well. For the four cases shown, the coefficient of determination, r^2, is the lowest for the case of 28 November 2011 with $r^2 = 0.26$ and the highest for the case of 14 October 2011 with $r^2 = 0.71$. In the former case, the low r^2 is caused by the poor model-observation agreement at about day 332.6. For the remaining time, the predictions and observations differ only slightly in magnitude. In the latter case, the temporal evolution is well reproduced by the model with only slight discrepancies at about day 318.4 and 318.6. For the four cases, α_{N0} is of the same order of magnitude, ranging between $1.02 \times 10^4\ \mathrm{m}^{-2}$ and $3.95 \times 10^4\ \mathrm{m}^{-2}$. Example 3 has also been analyzed by *Li et al.* [2014].

Overall, in 11 of the 14 Horqin cases (Cases 1–7 and 11–14), the model predictions and observations agree with regard to onset and cessation (where contained in the CTDE period) as well as overall characteristics and α_{N0} is of similar magnitude. Some discrepancies occur in the magnitude of predicted and observed emissions. There are, however, cases where model and measurements do not agree well. For example, in Case 8, the observations show relatively high emissions at the beginning of the CTDE period, which are not reproduced by the model. At this time, the SENSIT showed some signs of saltation, which might have produced the higher dust emissions and makes the estimate of α_{N0} sensitive to the fitting period selected. In Cases 9 and 10, a similar underestimation at the beginning of the event occurs but cannot be clearly attributed to saltation. Possible additional sources of model-observation differences are as follows:

1. Model predictions loose quality under suboptimal CTDE conditions, e.g., small w_*. The reason is that the parameterization of instantaneous momentum flux is optimized for convective conditions.
2. Dust is present already before the CTDE period, which causes a biased concentration measurement and thus biased dust emission estimate. This leads to an overestimation/underestimation in α_{N0}.
3. Dust emission is heterogeneous in the area and not all emitted dust particles pass the instruments. Part of the discrepancies in Cases 9 and 10 might be attributed to possibility (1), as w_* was relatively small at the beginning of the period.

For two of the JADE cases, the α_{N0} values are larger ($\geq 1 \times 10^5\ \mathrm{m}^{-2}$) than for the other cases. Analysis indicates that this might be caused by a u_* that intermittently exceeded u_{*t}. Figure 3a shows the time series of observed and modeled results and Figure 3b the 30 min averages of u_* and w_* together with $u_{*t} = 0.28\ \mathrm{m\,s}^{-1}$ [*Shao et al.*, 2011] for Case 16 (JADE Case 2). The magnitude of CTDE for this case was $\approx 200\ \mu\mathrm{g\,m}^{-2}\,\mathrm{s}^{-1}$, much larger than for the other cases. It can be seen that every time when u_* exceeded u_{*t}, the observed dust flux increased considerably, e.g., at day 62.15 or 62.3. The SPC measurements indicated intermittent saltation at these times. Thus, the relatively high fluxes were probably partially driven by saltation and partially by CTDE, giving a very large α_{N0} if the model is fitted to the data. A reduction of the modeled fluxes for about 50% would yield an α_{N0} of about $7 \times 10^4\ \mathrm{m}^{-2}$, close to α_{N0} of the other examples.

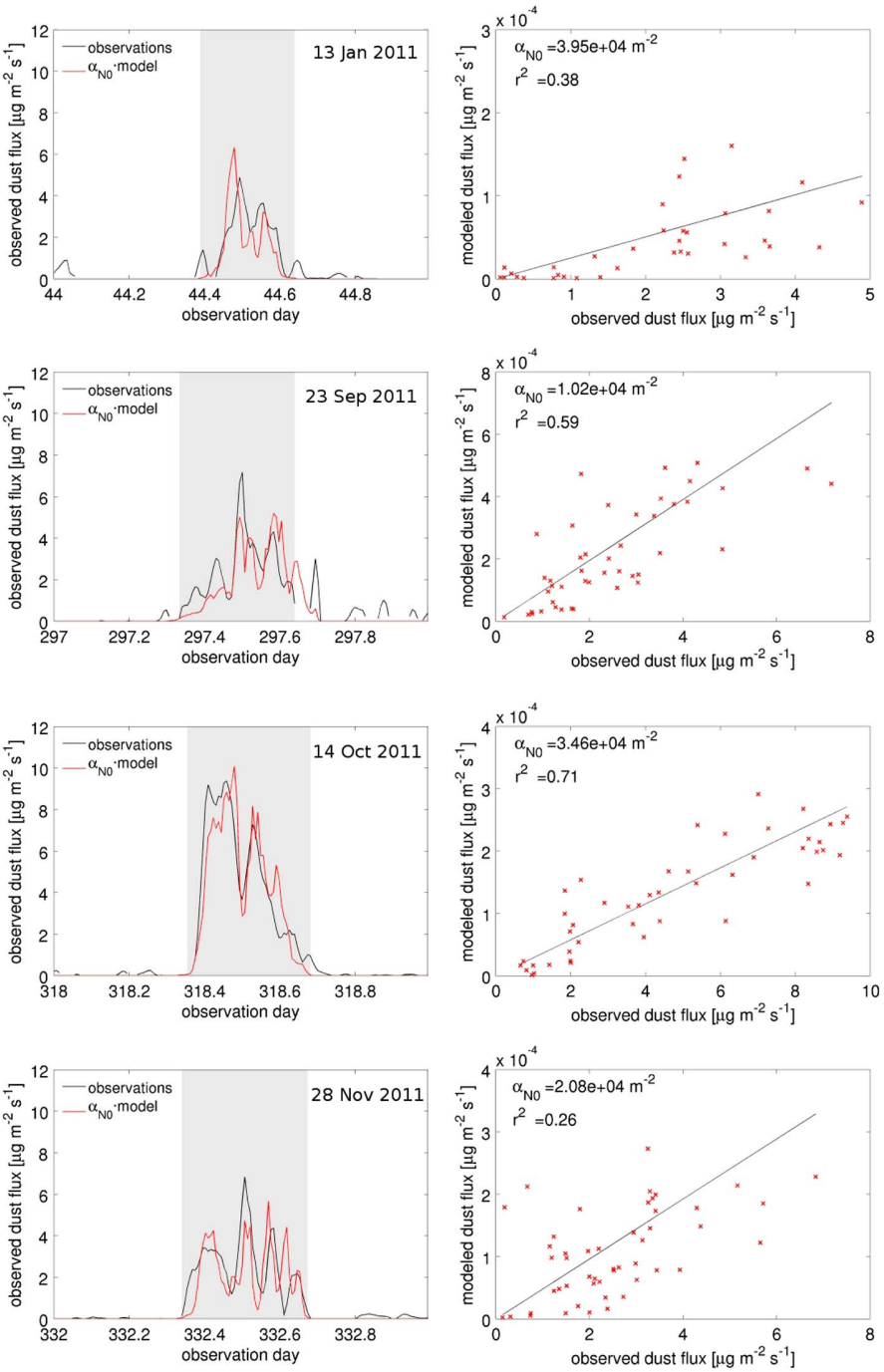

Figure 2. CTDE cases observed in the Horqin Sandy Land. Grey shadings indicate the times when the CTDE criteria were satisfied. (left) Time series of observed and modeled dust emission flux. The time is given in observation days (local time). (right) Corresponding modeled versus observed fluxes for determination of α_{N0}. Values are given in the figures. Note the varying axis scales in the scatterplots.

The same statement applies to Case 17 (JADE Case 3). The above discussions suggest that further improvements to the CTDE scheme are necessary in a future study to include the effect of intermittent saltation on dust emission.

Figure 4a shows α_{N0} for all events together with the corresponding mean soil moisture. The standard errors of α_{N0} are shown as error bars. Cases 1 and 11–13 are detailed in Figure 2. The volumetric water content was

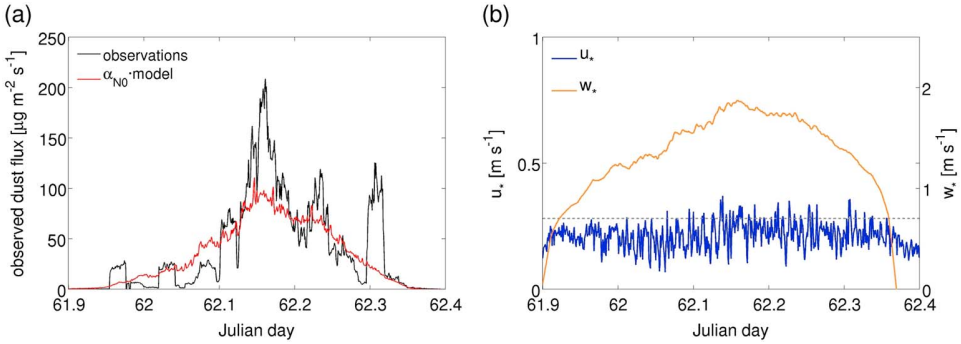

Figure 3. (a) Time series of observed and modeled dust fluxes at the JADE site. (b) Corresponding observations of u_*, w_*, and u_{*t} (dashed line).

measured at 5 cm depth at Horqin and at 1.1 cm at the JADE site. Due to evaporation, it can be assumed that the soil is generally drier at the very surface during daytime in absence of precipitation. Accordingly, there is probably an inconsistency between the soil moisture observations at the two sites.

In case of higher soil moisture, dust emission is expected to be lower and α_{N0} smaller due to dust particle cohesion. This tendency can be found for all cases except for the Horqin Cases 3 and 5 and JADE Case 1 (Case 15). The JADE events were all relatively dry, and saltation might have played a role, as discussed before. The dashed lines indicate the mean value, $\overline{\alpha}_{N0}$, of all cases and the sum of mean and standard deviation, $\overline{\alpha}_{N0} + \sigma_\alpha$. Cases 16 and 17 (JADE Cases 2 and 3) lie above the 1σ level. They are considered as being outliers and excluded from further analysis and model calibration. With the 16 remaining cases, a mean of $\overline{\alpha}_{N0} = 1.98 \times 10^4$ m^{-2} and a relative standard deviation of RSD = 67.7% were found. We hypothesize that this variation can be further reduced if the model accounted for the effects of soil moisture and surface roughness on CTDE. To test this hypothesis, correction methods for these effects are proposed.

5. Effects of Soil Moisture and Surface Roughness on Dust Emission

In *Klose and Shao* [2013], the cohesive and lifting forces are described as log-normal and Weibull pdfs, respectively. The moments of the distributions can be modified to reflect the effects of soil moisture and vegetation cover. Soil moisture affects soil cohesion and can be considered in the parameterization of the cohesive force. Vegetation affects the surface shear stress and can be accounted for in the parameterization of the lifting force.

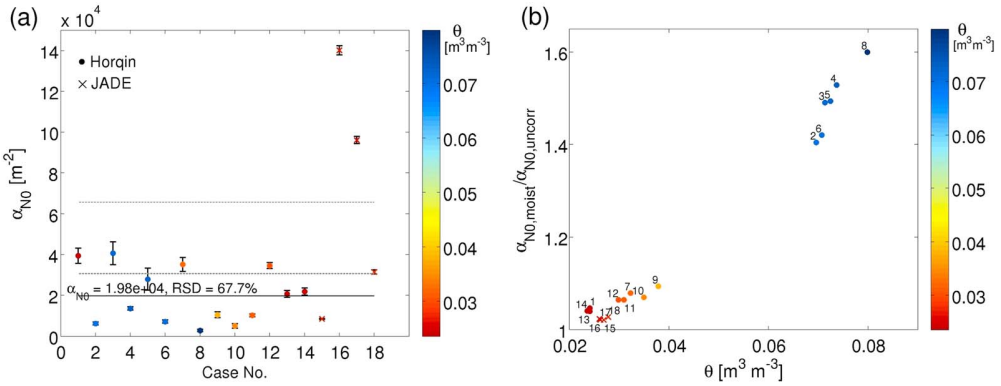

Figure 4. (a) Model parameter α_{N0} for the 18 selected CTDE cases. Colors represent the mean soil moisture during the events. The dashed lines indicate the mean value and mean $\pm\sigma_\alpha$ levels for all events (σ_α: standard deviation of α_{N0}). Events 16 and 17 were considered as outliers and excluded from statistical analysis. The black solid line shows the mean value of the 16 remaining cases. The relative standard deviation (RSD) is also given in the figure. (b) Relative increase $\alpha_{N0,moist}/\alpha_{N0,uncorr}$ with the soil moisture correction being included in the model.

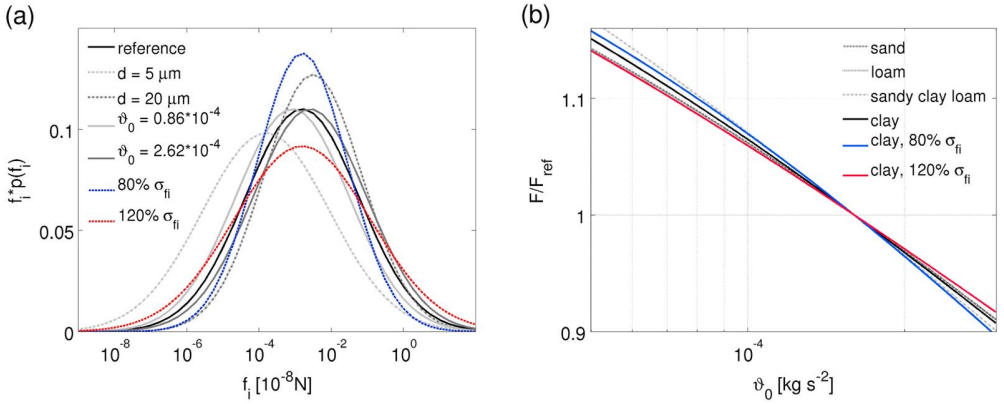

Figure 5. (a) Variation of $p(f_i)$ for varying particle diameter (5, 10, and 20 µm), varying $\bar{f}_i$ as specified by ϑ_0 ([0.5,3] kg s^{-2}), and modified σ_{f_i} (±20%). "Reference" refers to the settings described in section 2, shown for a particle diameter of 10 µm. (b) Senitivity of dust flux, F, to ϑ_0 shown relative to the dust flux obtained from the reference setting, F_{ref}. The sensitivity is shown for different soil types and σ_{f_i}.

5.1. Sensitivity of Dust Flux to Cohesive Force

Before soil moisture effects can be incorporated, the accuracy of the cohesive force parameterization must be assessed. Due to the limited understanding of this force and due to large variability in the data available from literature [e.g., *Zimon*, 1982; *Felicetti et al.*, 2007], no precise accuracy estimate can be provided. To evaluate the dust flux uncertainties arising from the cohesive force, a sensitivity experiment is conducted. Both, mean value, $\bar{f}_i$, and standard deviation, σ_{f_i}, are varied within a predefined range and the corresponding dust flux is calculated with equal boundary conditions. $\bar{f}_i$ is estimated from equation (7). For the sensitivity test, ϑ_0 has been varied between 0.5×10^{-4} and 3×10^{-4} kg s^{-2} (−70%, +90% compared to $\vartheta_{0\text{ref}} = 1.6$ kg s^{-2}) and σ_{f_i} is obtained from equation (8) and varied by ±20% . Figure 5a shows $p(f_i)$ for the particle diameters 5, 10, and 20 µm together with the results from variation of $\bar{f}_i$ and σ_{f_i}. As seen, the distribution shifts to larger values for increasing diameter and the standard deviation decreases. The reduction of σ_{f_i} results in a smaller contribution of small/large f_i, and intermediate values are of higher importance. The modification of $\bar{f}_i$ shifts the distribution to smaller or larger f_i. Figure 5b presents the relative dust flux F/F_{ref} for the soil types sand, loam, sandy clay loam, and clay. Note that according to our parameterization, the cohesive force does not depend on soil type but on particle diameter only. F_{ref} refers to dust emission flux obtained with the settings described in section 2. The different results for the four soil types arise from the differences in their particle size distributions. In general, the dust flux decreases for increasing $\bar{f}_i$ as in that case the lifting force, f, less frequently exceeds f_i. In contrast, an increase in σ_{f_i} may either increase or decrease the dust flux depending on f. For a given f, dust emission is proportional to the area $\int_{-\infty}^{f} p\left(f_i\right) \mathrm{d}f_i$; thus, the effect of σ_{f_i} on dust emission can be seen from the slope of the cumulative distribution function (cdf) of f_i, which increases with decreasing σ_{f_i}, and thus, the relative location of f to the intercept point between the cdfs of different σ_{f_i} reveals whether the dust flux increases or decreases. Our tests show that the variation of $\bar{f}_i$ by about 70–90% yields a change in dust flux by about 10–15%, while a 20% variation in σ_{f_i} only a change by about 1–2%.

5.2. Soil Moisture Correction

For moist soils, the cohesive force on average is larger than for dry soils. The variance of the cohesive force accounts for its fluctuations due to particle shape, surface roughness, Van-der-Waals force, electrostatic forces, etc. For dry soils, the variance is relatively large, while for wet soils, the capillary force becomes the dominant component of the cohesive force. Using wind tunnel experiments, *Chepil* [1956] found that soil erodibility is a function of the amount of water adsorbed on the particles. After comparison with earlier studies [e.g., *Haines*, 1925; *Fisher*, 1926; *Allberry*, 1950], Chepil concluded that the capillary cohesive forces are much higher than the adsorptive cohesive forces. *Chen et al.* [1996] confirmed this by concluding that "when soil moisture changed from film to capillary water, soil resistance to wind erosion transformed with a step-like pattern." *Zimon* [1982] compared theoretical results with experiments and concluded that "Under conditions of capillary condensation, adhesive forces are determined entirely by capillary forces since they are greater than all other components of the adhesive forces." We thus expect the cohesive force to become more and more deterministic with increasing soil moisture such that its value approaches the sum of mean

dry and capillary cohesion and its variance becomes negligible. In our CTDE scheme, the cohesive force is parameterized as log-normal distribution with mean value

$$M = \exp\left(\mu + \frac{\sigma_{f_i}^2}{2}\right) \tag{18}$$

where $\mu = \ln \bar{f}_i$ according to equation (6). Following a definition frequently used in hydrology [e.g., *Brooks and Corey*, 1964; *van Genuchten*, 1980], we specify the relative soil moisture as $(\theta - \theta_r)/(\theta_s - \theta_r)$, where θ is the volumetric soil moisture, θ_s that at saturation, and θ_r the air-dry soil moisture. Based on the aforementioned arguments, it seems reasonable to propose for shape parameter and mean value of $p(f_i)$

$$\sigma_{f_i,\mathrm{moist}}^2 = \left(1 - \left(\frac{\theta - \theta_r}{\theta_s - \theta_r}\right)^n\right) \sigma_{f_i,\mathrm{dry}}^2 \tag{19}$$

$$M_{\mathrm{moist}} = M_{\mathrm{dry}} + f_{i_c} \tag{20}$$

with f_{i_c} being the capillary cohesive force and n being a coefficient. n determines how rapidly the variance approaches zero. We suggest $n = 2$, but due to relatively dry conditions during the selected CTDE event, n is to be determined on a more detailed data basis including a wider moisture range and different soil textures. Assuming further that $M_{\mathrm{moist}} = \exp\left(\mu_{\mathrm{moist}} + \sigma_{f_i,\mathrm{moist}}^2/2\right)$ (compare equation (18)), it follows

$$\mu_{\mathrm{moist}} = \ln\left(\exp\left(\mu_{\mathrm{dry}} + \frac{\sigma_{f_i,\mathrm{dry}}^2}{2}\right) + f_{i_c}\right) - \frac{\sigma_{f_i,\mathrm{moist}}^2}{2}. \tag{21}$$

Thus, $p(f_i)$ can be recalculated with the adjusted μ and σ_{f_i}.

McKenna Neuman and Nickling [1989] and *McKenna Neuman* [2003] investigated the effect of soil moisture on particle entrainment by wind and developed a theory for quantification of the capillary cohesive force for sand particles by making assumptions for the particles' contact geometry. They obtained

$$f_{i_c} = G\frac{\pi T^2}{|\Delta P|} \tag{22}$$

with water surface tension T [N m^{-1}], pressure difference between soil water and atmosphere ΔP [N m^{-2}], and the dimensionless geometric coefficient G. *Fécan et al.* [1999] used this approach to develop a moisture correction for u_{*t}. The latter authors augmented the theory of *McKenna Neuman and Nickling* [1989] for other soil types by generalizing the parameterization to consider also the adsorptive film covering the particles. This film is relatively unimportant for sandy soils, but important for loam and clay soils, as a significant part of water is trapped in the adsorptive film for the latter soil types [*Fécan et al.*, 1999]. As the adsorptive forces are much weaker than the capillary forces [*Chepil*, 1956; *Chen et al.*, 1996], the maximum amount of water, which can be adsorbed onto the particles' surfaces, can be considered as the lower threshold before the cohesive forces increase profoundly due to soil moisture. This soil moisture threshold can be approximated by the air-dry soil moisture [*Fécan et al.*, 1999]. *Cornelis et al.* [2004a, 2004b] made a similar approach as *McKenna Neuman and Nickling* [1989] but used explicit formulations for dry and wet cohesive forces.

As the capillary cohesive force depends on the contact area between the particles, we expect f_{i_c} to increase with particle volume or particle mass, m_p, and with the soil water content. Following *Gardner* [1970] and *Fécan et al.* [1999], the relation between $|\Delta P|$ and capillary water, approximated as $(\theta - \theta_r)$, can be given as

$$|\Delta P| = a' \left(\theta - \theta_r\right)^{-b'} \tag{23}$$

with parameters a' and b'. Based on these considerations, we hypothesize

$$f_{i_c} \propto m_p \left(\theta - \theta_r\right)^b \tag{24}$$

where b is a constant. This hypothesis can be confirmed theoretically as follows.

Based on the balance of forces acting on a particle at rest, a relationship for the ratio of moist to dry threshold friction velocity, u_{*t}, can be derived (Appendix 2):

$$\frac{u_{*t}(\theta)}{u_{*t}(\theta_r)} = \left[1 + \frac{h_w}{\psi_s}\left(\frac{\theta - \theta_r}{\theta_s - \theta_r}\right)^b\right]^{0.5} \tag{25}$$

where h_w combines various constants as

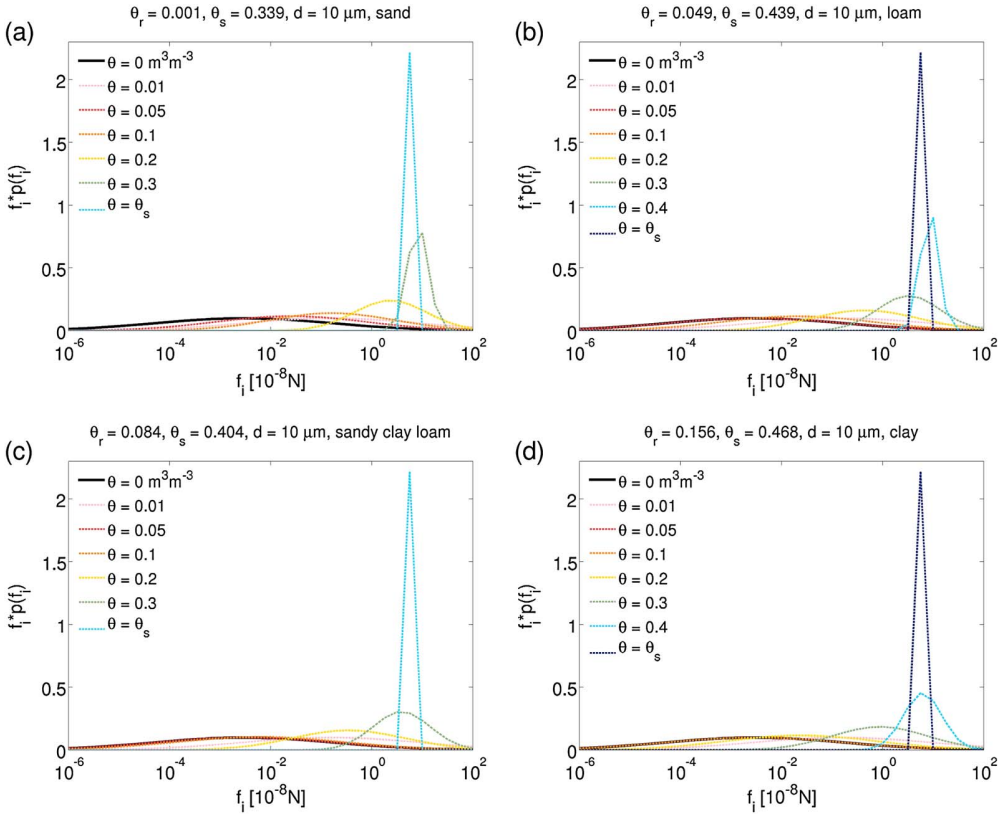

Figure 6. Soil moisture correction of $p(f_i)$ for particles with diameter 10 µm and volumetric soil moisture varying from dry conditions ($\theta = 0\,\mathrm{m^3m^{-3}}$) to saturation ($\theta \approx \theta_s$). Results are shown for the soil texture classes (a) sand, (b) loam, (c) sandy clay loam, and (d) clay. The values of θ_r and θ_s are given in the figure titles.

$$h_w = G\frac{\pi T^2}{\rho_w g}\frac{6\sin 2\xi}{\pi d^3(\rho_p - \rho)g\sin\xi} \tag{26}$$

ψ_s denotes the saturation capillary pressure head [m]. Equation (25) is consistent with the results of *Fécan et al.* [1999], as can be seen by setting

$$a = \frac{h_w}{\psi_s}\left(\theta_s - \theta_r\right)^{-b} \tag{27}$$

and converting gravimetric into volumetric soil moisture. By combining equations (B4) and (27), it follows that

$$f_{i_c} = \frac{G\pi T^2}{\rho_w g}\frac{a}{h_w}\left(\theta - \theta_r\right)^b. \tag{28}$$

Application of equation (26) and assumption of $\rho \ll \rho_p$ directly yields

$$f_{i_c} = a \cdot m_p g\frac{\sin\xi}{\sin 2\xi}\left(\theta - \theta_r\right)^b \tag{29}$$

with $m_p = \rho_p \pi d^3/6$ and a and b being empirical parameters, which are soil type dependent. For simplicity, we set $\xi = 45°$ representing a close-packed system (particle resting on four others) [*McKenna Neuman and Nickling*, 1989]. Equation (29) confirms the hypothesis given in equation (24). With this, f_{i_c} can be incorporated into the CTDE scheme with moisture correction (equations (20) and (21)). Figure 6 exemplifies the distributions $p(f_i)$ for particles of size 10 µm resulting from a variation of soil moisture for the soil texture classes sand, loam, sandy clay loam, and clay. The hydrological properties are obtained from Y. Shao and E. Jung (unpublished manuscript, 2000) (θ_r, a, and b) and from the Weather Research and Forecasting (WRF) model default soil parameters, adapted from U.S. Geological Survey (USGS) data (θ_s). Table 1 summarizes the

Table 1. Hydrological Parameters for Twelve Soil Types for Use in the Soil Moisture Correction[a]

	θ_r [m^3 m^{-3}]	θ_s [m^3 m^{-3}]	a	b
sand	0.001	0.339	21.19	0.68
loamy sand	0.003	0.421	33.03	0.71
sandy loam	0.037	0.434	44.87	0.85
loam	0.049	0.439	17.79	0.61
silty loam	0.061	0.467	20.81	0.66
silt	0.072	0.467	23.83	0.71
sandy clay loam	0.084	0.404	26.84	0.75
clay loam	0.095	0.465	29.86	0.80
silty clay loam	0.110	0.464	27.51	0.75
sandy clay	0.126	0.406	25.17	0.70
silty clay	0.141	0.468	22.82	0.64
clay	0.156	0.468	20.47	0.59

[a] θ_r, a, and b are obtained from Y. Shao and E. Jung (unpublished manuscript, 2000) and θ_s from USGS data.

hydrological parameters for 12 soil texture categories. It can be seen that the distribution shifts to larger cohesive forces with increasing soil moisture and becomes a delta function (within the limited bin resolution) at saturation. Depending on θ_r for the different soil types, the shifting starts at different soil moisture content. The distributions show a decreasing probability of very large cohesive forces with increasing moisture. This behavior seems realistic, when considering the decreasing stochasticity in these situations, but has not been confirmed by measurements. *Ravi et al.* [2004, 2006] showed that θ_r varies with atmospheric relative humidity (RH). The use of a constant θ_r for each soil type, as practiced in this study, is thus a simplification. The consideration of humidity-dependent θ_r could be realized without qualitative effect on the moisture correction suggested. However, as the relationship between θ_r and RH is unknown for the soils used in this study, the approximation with constant θ_r seems justified. Figure 7 shows the ratio F/F_{dry} for the four soil types, with F_{dry} being the emission flux at zero soil moisture. The vertical lines indicate θ_r (left) and θ_s (right), respectively (compare Table 1). Sand has a low water holding capacity and F is reduced instantly at small θ, whereas the decrease in F starts later for soil types with higher θ_r (e.g., sandy clay loam). In all examples, the atmospheric conditions were held constant by setting $u_* = 0.1\,\mathrm{m\,s^{-1}}$, $w_* = 3\,\mathrm{m\,s^{-1}}$, and $1/L = -0.063$. These values are typical for a convective atmospheric boundary layer.

In section 4, the model results (without soil moisture correction) were compared to the observations and α_{N0} was found to be scattered within a certain range. It is hypothesized that part of the scatter can be attributed to soil moisture effects. The CTDE scheme was rerun for these cases, but this time with moisture correction. As dust emission is now reduced by the correction procedure, the resulting model parameter increases and is expected to equal its dry value. Figure 4b shows the relative increase $\alpha_{N0,moist}/\alpha_{N0,uncorr}$. Cases with higher soil moisture experience a stronger correction than cases with lower moisture. For Case 8, $\theta = 0.08\,\mathrm{m^3\,m^{-3}}$ and α_{N0} is nearly doubled, whereas for Case 13, α_{N0} remains almost unchanged for $\theta = 0.03\,\mathrm{m^3\,m^{-3}}$. Due to the small initial value, e.g., for Case 8, the absolute change is still relatively low and can thus be barely recognized when plotted as in Figure 4a. The greatest changes can be seen for Cases 3 and 5, which have already high α_{N0} values without use of the moisture correction. Overall, the mean of α_{N0} increased from 1.98×10^4 to $2.35 \times 10^4\,\mathrm{m^{-2}}$. Again, Cases 16 and 17 were excluded for the reasons explained in section 4. The relative standard deviation increased by about 3% to 70.5% rather than decreased as we have hoped. A possible reason for this increase is that the soil moisture variation is very small for the 16 cases considered (0.03 to 0.08 m^3 m^{-3}), and consequently, the scatter of α_{N0} is already relatively small without accounting for the soil moisture effect. This makes a precise determination of n (equation (20)) impossible. Further, as discussed in section 4, the soil moisture measurements have been conducted at different soil depths (5 cm for Horqin and

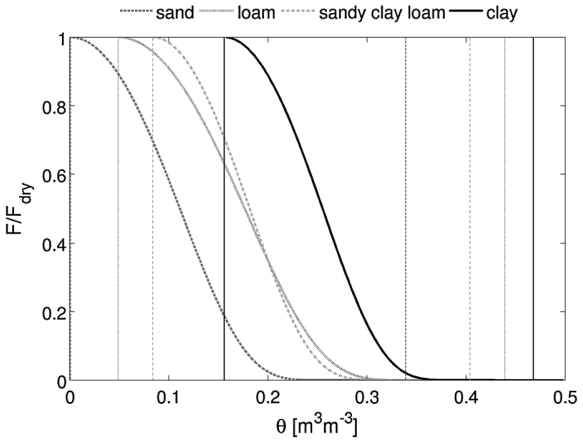

Figure 7. Relative decrease of dust emission flux with increasing soil moisture derived from the CTDE scheme. Vertical lines pairwise indicate (left) θ_r and (right) θ_s (compare Table 1).

1.1 cm for JADE). Further, the soil moisture observed at 5 cm depth may be not suitable for representing the wetness of the very top soil layer. Although the results shown in Figure 4b are not ideal, our hypothesis remains that the consideration of soil moisture effects would reduce the variation in α_{N0}. We note that our proposed moisture correction is preliminary and its evaluation remains subject to tests with data covering a wider soil moisture range.

5.3. Roughness Correction

In traditional dust emission models, the effect of surface roughness is treated by use of a drag partition theory: the presence of roughness elements reduces the shear stress on the exposed surface or, equivalently, increases the threshold friction velocity [e.g., *Raupach et al.*, 1993; *Shao and Yang*, 2008]. Following the previous studies, surface roughness can be quantified with two parameters, namely, the fraction of cover, η, and the frontal area index, λ, which is defined as the area of the roughness elements projected on the flow per unit ground area [*Shao*, 2008]. On the one hand, the cover fraction reduces the rate of emission by directly preventing particle movement:

$$F_{\text{corrected}} = (1-\eta)F_{\text{uncorrected}} \tag{30}$$

and on the other hand, roughness elements reduce the shear stress on the surface. According to the drag partition theory, the total (mean) drag can be partitioned into a ground surface drag τ_s, a pressure drag τ_r, and a canopy-surface drag τ_c [*Shao*, 2008]:

$$\tau = \tau_s + \tau_r + \tau_c. \tag{31}$$

For dust particle movement, the ground surface drag is to be considered and it is expected that the mean momentum flux is reduced in the presence of roughness elements. Thus, we suggest to correct the mean value of instantaneous momentum flux, μ_τ, as

$$\frac{\mu_{\tau,\text{veg}}}{\mu_\tau} = \frac{\tau_s}{\tau}. \tag{32}$$

Raupach et al. [1993] proposed

$$\frac{\tau_s}{\tau} = \frac{1}{1+\beta_r\lambda} \tag{33}$$

for ground-surface drag, with $\beta_r = C_r/C_s$ being the ratio of element to surface drag coefficients. In this study, $\beta_r = 90$ is used as recommended by Raupach et al. In the CTDE scheme, the proposed correction is employed as follows. First, the shape and scale parameters, α and β, for given atmospheric conditions are calculated as described in section 3. Second, the mean value μ_τ of the given Weibull distribution is obtained based on α and β as

$$\mu_\tau = \beta\Gamma\left(1+\alpha^{-1}\right). \tag{34}$$

Third, μ_τ is corrected according to equation (32), and finally, a corrected scale parameter β is determined as

$$\beta_{\text{veg}} = \frac{\mu_{\tau,\text{veg}}}{\Gamma\left(1+\alpha^{-1}\right)}. \tag{35}$$

Figure 8 shows the sensitivity of $p(\tau_f)$ to vegetation cover fraction. This test has been conducted with predefined atmospheric conditions (see section 5.2). In general, momentum flux decreases with increasing vegetation cover (Figure 8a). For $\eta > 0.1$, momentum flux only covers small values and dust emission is substantially reduced (Figure 8b). According to the presented roughness correction, dust emission is negligible for a vegetation fraction $\geq$0.2. Constraints for this value are discussed in the following. No test of the roughness correction could be performed, because for the Horqin site, data are insufficient for a reliable quantification of the rough surface and for the JADE site, the surface was almost bare for all four cases.

The above-proposed correction is preliminary and is subject to several important comments. First, we have assumed that the variance of $p(\tau_f)$ remains constant for different roughness conditions. The reduction of μ_τ basically accounts for changes of the mean wind due to roughness elements, e.g., trees. For CTDE, the mean wind is not as decisive as it is for saltation. Small-scale turbulence is expected to increase in the wake regions of roughness elements, which may play a role in turbulent dust emission. It is plausible to suggest that the

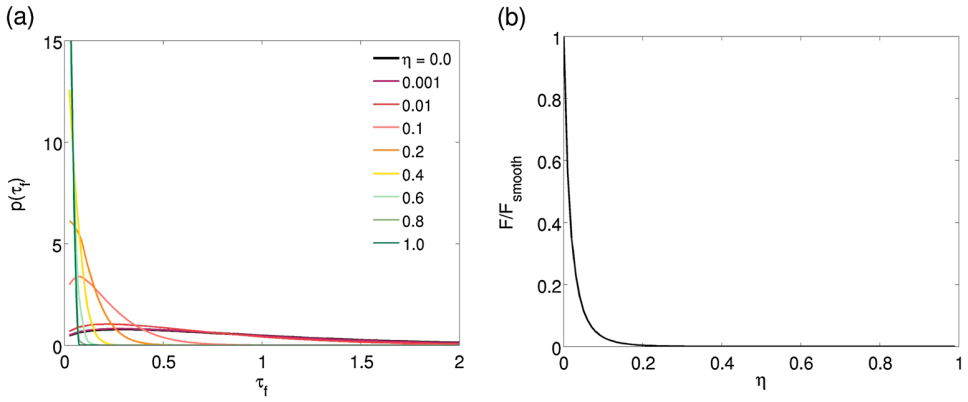

Figure 8. (a) Probability density function of instantaneous momentum flux, $p\left(\tau_f\right)$, with roughness correction for varying vegetation cover fractions η. (b) Sensitivity of dust emission flux to vegetation cover fraction.

variance may actually increase for certain rough surfaces. However, the quantification of the variance in dependence on λ and η requires further investigation. Second, the large-eddy simulations, from which we derived $p(\tau_f)$, did not consider the effects of roughness elements. Third, the inclusion of the roughness element effect on the variance of τ_f will probably lead to dust emission from surfaces with high cover fractions (e.g., $\lambda > 0.2$). At the Horqin site, for example, the cover fraction in the vicinity of the measurement station was about 0.5 [*Li et al.*, 2014], but dust emission was observed nevertheless. As the CTDE mechanism is not intrinsically related to mean wind shear, but to convective eddies on scales of 10 to 100 m, the heterogeneous distribution of vegetation would still permit dust emission. For example, while vegetation cover was generally high at the Horqin site, patches of surfaces were completely exposed, allowing for dust uplift. The importance of roughness element configuration on shear stress distribution has been studied by *Brown et al.* [2008]. The effect has also been found to affect horizontal saltation flux [*Li et al.*, 2013; *Dupont et al.*, 2014; *Webb et al.*, 2014]. The influence on CTDE is expected to be even more important, as the full shear stress distribution is relevant compared to the contribution of shear stresses $>u_{*t}$ considered for horizontal saltation flux.

6. Summary and Conclusions

An improved scheme for convective turbulent dust emission (CTDE) has been presented. Improvements have been made by developing a new parameterization of instantaneous momentum flux as well as corrections for soil moisture and surface roughness effects and by advancing the representations of cohesive force and particle size distribution. The probability density functions of instantaneous momentum fluxes, $p(\tau_f)$, have been derived from large-eddy simulations and then summarized using a similarity method. We have shown that $p(\tau_f)$ depends on atmospheric stability and can be approximated using a Weibull distribution. To reflect the impact of shear- and buoyancy-generated turbulence on τ_f, a combination of u_* and w_* is used as a scaling for τ_f. *Moeng and Sullivan* [1994] summarized three different scaling velocities, w_m, for boundary layer turbulence, namely, $w_m = (w_*^2 + 4u_*^2)^{1/2}$ [*Zeman and Tennekes*, 1977], $w_m = (w_*^3 + 25u_*^3)^{1/3}$ [*Driedonks*, 1982], and their own result $w_m = (w_*^3 + 5u_*^3)^{1/3}$. In this study, the optimal scaling velocity for τ_f in the context of using the Weibull approximation for $p(\tau_f)$ turns out to be $w_m = \left(w_*^3 + 19u_*^3\right)^{1/3}$.

Eighteen CTDE cases selected from field observations at Horqin (China) [*Li et al.*, 2014] and from the JADE observations (Australia) [*Ishizuka et al.*, 2008, 2014] have been used for model calibration and evaluation. Good agreements between the model predictions and observations have been found for most of the cases. Deficiency in model performance has been discovered in case of intermittent saltation, which is not represented by the CTDE scheme. For two cases, the model has been found to underestimate the observed flux at the beginning of the CTDE period. Three possible explanations have been suggested: (1) the model accuracy is reduced in case of small w_*, as the model is optimized for convective turbulent conditions; (2) dust was present in the air before CTDE started; and (3) dust emission was heterogeneous and not all emissions were captured by the instruments. However, it remains unclear whether one or more reasons indeed explain the model-observation differences.

The comparison with the field data has enabled the estimate of the model parameter α_{N0}. The mean value is found to be $\alpha_{N0} = 1.98 \times 10^4\ \mathrm{m}^{-2}$ and $2.35 \times 10^4\ \mathrm{m}^{-2}$, respectively, without and with soil moisture correction. We have argued that a soil moisture correction would decrease the scatter of α_{N0}, but no decrease in relative standard deviation (RSD) could be found. The RSD increased from about 68% to 71% when applying the soil moisture correction. Possible reasons for the lack in improvement may include (1) the small variation in soil moisture in the two data sets, (2) different measurement depths at the Horqin and JADE sites, and (3) inappropriate representation of the top soil moisture by the measurements at greater depths, e.g., at 5 cm. The skill of the proposed soil moisture correction is thus unclear until further tested against measurements which cover a wider soil moisture range. Nevertheless, we believe the soil moisture correction is necessary to remove part of the variations in α_{N0}. Preliminary ideas for roughness correction have been presented but not tested against data. While we have made considerable progress in constructing and evaluating the CTDE scheme, more tests are required and data which enable a more thorough model performance examination are desirable. Influences of surface crust and other environmental effects are also subject to future investigations. The implementation of the CTDE scheme in regional and global models is being planned to assess the importance of CTDE in the Earth system, and we expect that airborne dust generated by CTDE has significant impacts on radiation, ocean biogeochemistry, air quality, etc.

Appendix A: Parameterization of Instantaneous Momentum Flux: Frechét pdf

Figure A1 shows $p(\tau_f)$ fitted with Frechét distributions and the corresponding correlation coefficients. The overall characteristic is represented well, but the agreement decreases with atmospheric stability. The optimal scaling for the Frechét distributions was found with

$$s_F = \left(w_*^3 + 43u_*^3\right)^{2/3}. \tag{A1}$$

See also section 3.

Appendix B: Relation of Threshold Friction Velocity to Soil Moisture: Derivation

Based on the balance of forces acting on a particle at rest with resting angle ξ, it was found [*McKenna Neuman and Nickling*, 1989; *Shao*, 2008]

$$\frac{u_{*t}(\theta)}{u_{*t}(\theta_r)} = \left[1 + f_{i_c}\frac{6\sin 2\xi}{\pi d^3(\rho_p - \rho)g\sin\xi}\right]^{0.5}. \tag{B1}$$

Further, the relation between capillary pressure head ψ (height of equivalent water column, also called capillary suction) [m] and capillary pressure ΔP (or capillary potential) [Pa] [*Shao*, 2008] as well as the soil-water retention curve of *Brooks and Corey* [1964] are given by

$$\psi = \frac{\Delta P}{\rho_w g} \tag{B2}$$

$$\psi = \psi_s\left(\frac{\theta - \theta_r}{\theta_s - \theta_r}\right)^{-b}, \tag{B3}$$

with water density ρ_w, gravitational acceleration g, and saturation capillary pressure head ψ_s. ΔP represents the pressure difference between the soil water and the atmosphere [*Brooks and Corey*, 1964; *Shao*, 2008]. By applying equations (B2) and (B3) to equation (22), it can be deduced that

$$f_{i_c} = G\frac{\pi T^2}{\rho_w g|\psi_s|}\left(\frac{\theta - \theta_r}{\theta_s - \theta_r}\right)^{b}. \tag{B4}$$

It follows

$$\frac{u_{*t}(\theta)}{u_{*t}(\theta_r)} = \left[1 + \frac{h_w}{\psi_s}\left(\frac{\theta - \theta_r}{\theta_s - \theta_r}\right)^{b}\right]^{0.5} \tag{B5}$$

where h_w combines various constants as

$$h_w = G\frac{\pi T^2}{\rho_w g}\frac{6\sin 2\xi}{\pi d^3(\rho_p - \rho)g\sin\xi}. \tag{B6}$$

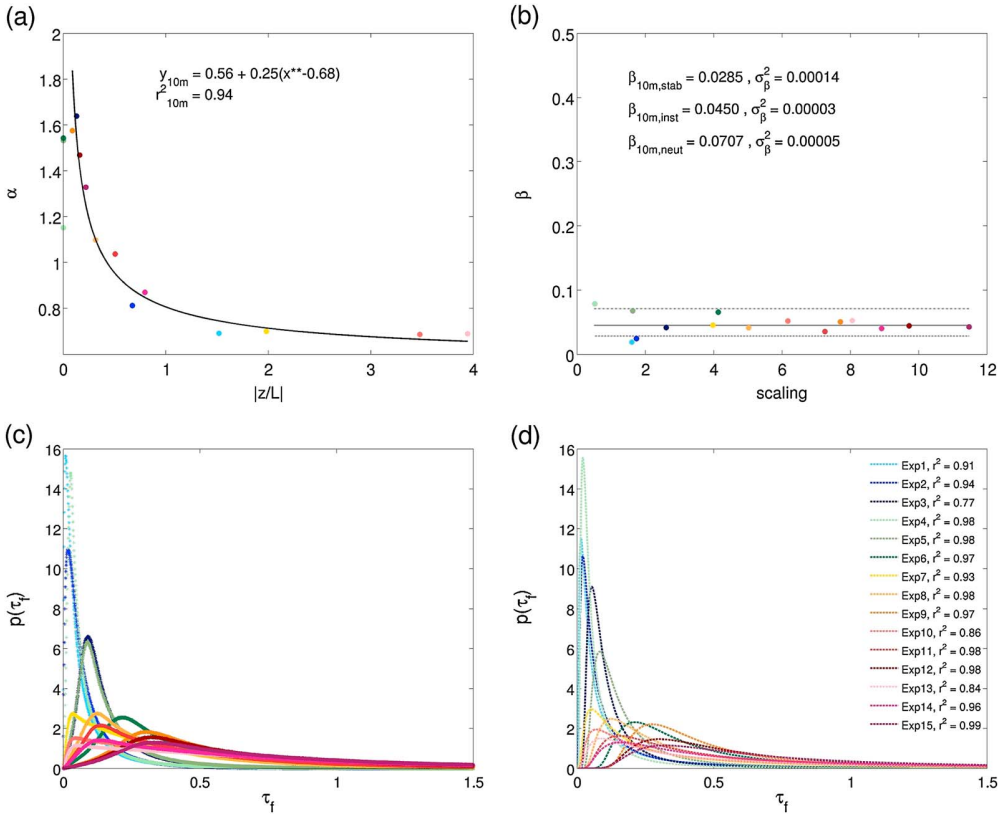

Figure A1. (a) Relationship between shape parameter α and stability parameter $|z/L|$ and coefficient of determination, r^2. (b) Mean values of scaling parameter β for different atmospheric stabilities and the corresponding variances σ_β. Probability density functions of instantaneous momentum flux (c) obtained from LES and (d) reproduced using Frechét distributions with the parameters obtained from equation (17) and the constant β approximation as shown in Figures A1a and A1b, except for neutral conditions, where the shape parameter has been taken from the fitting directly.

Acknowledgments
We wish to thank Philipp Schlüter for his assistance in data processing and three reviewers for valuable comments and suggestions, which helped to improve the manuscript. Users can access the data from the paper at request. Supplements to the model simulations and field data sets can be provided by the leading author (email: mklose@uni-koeln.de) in consultation with the coauthors. The work was partly supported by the National Natural Science Foundation of China (41075005) and by the Kakenhi Grants-in-Aid for Scientific Research (A) from the Japan Society for the Promotion of Science (17201008 and 20244078).

References

Alfaro, S. C., and L. Gomes (2001), Modeling mineral aerosol production by wind erosion: Emission intensities and aerosol size distributions in source areas, *J. Geophys. Res.*, *106*(D16), 18,075–18,084, doi:10.1029/2000JD900339.

Allberry, E. C. (1950), On the capillary forces in an idealized soil, *J. Agric. Sci.*, *40*, 134–142.

Allen, C. J. T., R. Washington, and S. Engelstaedter (2013), Dust emission and transport mechanisms in the central Sahara: Fennec ground-based observations from Bordj Badji Mokhtar, June 2011, *J. Geophys. Res. Atmos.*, *118*, 6212–6232, doi:10.1002/jgrd.50534.

Ansmann, A., M. Tesche, P. Knippertz, E. Bierwirth, D. Althausen, D. Müller, and O. Schulz (2008), Vertical profiling of convective dust plumes in southern Morocco during SAMUM, *Tellus B*, *61*, 340–353, doi:10.1111/j.1600-0889.2008.00384.x.

Brooks, R. H., and A. T. Corey (1964), *Hydraulic Properies of Porous Media, Hydrology Paper, 3*, Colorado State Univ., Fort Collins.

Brown, S., W. G. Nickling, and J. A. Gillies (2008), A wind tunnel examination of shear stress partitioning for an assortment of surface roughness distributions, *J. Geophys. Res.*, *113*, F02S06, doi:10.1029/2007JF000790.

Chen, W., D. Zhibao, L. Zhenshan, and Y. Zuotao (1996), Wind tunnel test of the influence of moisture on the erodibility of loessial sandy loam soils by wind, *J. Arid Environ.*, *34*(4), 391–402, doi:10.1006/jare.1996.0119.

Chepil, W. S. (1956), Influence of moisture on erodibility of soil by wind, *Soil Sci. Soc. Am. J.*, *20*, 288–292, doi:10.2136/sssaj1956.03615995002000020033x.

Chkhetiani, O. G., E. B. Gledzer, M. S. Artamonova, and M. A. Iordanskii (2012), Dust resuspension under weak wind conditions: Direct observations and model, *Atmos. Chem. Phys.*, *12*, 5147–5162, doi:10.5194/acp-12-5147-2012.

Corn, M. (1961), Adhesion of solid particles to solid surface, I. A review, *J. Air Pollut. Control Assoc.*, *11*(11), 523–537.

Cornelis, W. M., D. Gabriels, and R. Hartmann (2004a), A conceptual model to predict the deflation threshold shear velocity as affected by near-surface soil water: I. Theory, *Soil Sci. Soc. Am. J.*, *68*, 1154–1161.

Cornelis, W. M., D. Gabriels, and R. Hartmann (2004b), A parameterisation for the treshold shear velocity to initiate deflation of dry and wet sediment, *Geomorphology*, *59*, 43–51, doi:10.1016/j.geomorph.2003.09.004.

Descamps, I., J.-L. Harion, and B. Baudoin (2005), Taking-off model of particles with a wide size distribution, *Chem. Eng. Process.*, *44*, 159–166, doi:10.1016/j.geomorph.2003.09.004.

Driedonks, A. G. M. (1982), Models and observations of the growth of the atmospheric boundary layer, *Boundary Layer Meteorol.*, *23*, 283–306.

Dupont, S., G. Bergametti, and S. Simoëns (2014), Modeling aeolian erosion in presence of vegetation, *J. Geophys. Res. Earth Surf.*, *119*, 168–187, doi:10.1002/2013JF002875.

Fécan, F., B. Marticorena, and G. Bergametti (1999), Parameterization of the increase of the aeolian erosion threshold wind friction velocity due to soil moisture for arid and semi-arid areas, *Ann. Geophys.*, *17*, 149–157.
Felicetti, M. A., F. Piantino, J. R. Coury, and M. L. Aguiar (2007), Influence of removal time and particle size on the particle substrate adhesion force, *Braz. J. Chem. Eng.*, *25*(1), 71–82.
Fisher, R. A. (1926), On the capillary forces in an ideal soil. Correction of formulae given by W. B. Haines, *J. Agric. Sci.*, *16*, 492–505.
Gardner, W. R. (1970), Field measurement of soil water diffusivity, *Soil Sci. Soc. Am. Proc.*, *34*, 832–833.
Haines, W. B. (1925), Studies of the physical properties of soils. II. A note on the cohesion developed by capillary forces in an ideal soil, *J. Agric. Sci.*, *15*, 529–535.
Heintzenberg, J. (2008), The SAMUM-1 experiment over Southern Morocco: Overview and introduction, *Tellus B*, *61*, 2–11, doi:10.1111/j.1600-0889.2008.00403.x.
Ishizuka, M., M. Mikami, J. Leys, Y. Yamada, S. Heidenreich, Y. Shao, and G. H. McTainsh (2008), Effects of soil moisture and dried raindroplet crust on saltation and dust emission, *J. Geophys. Res.*, *113*(D24212), doi:10.1029/2008JD009955.
Ishizuka, M., M. Mikami, J. F. Leys, Y. Shao, Y. Yamada, and S. Heidenreich (2014), Power law relation between size-resolved vertical dust flux and friction velocity measured in a fallow wheat field, *Aeolian Res.*, *12*, 87–99, doi:10.1016/j.aeolia.2013.11.002.
Ito, J., H. Niino, and M. Nakanishi (2010), Large eddy simulation on dust suspension in a convective mixed layer, *SOLA*, *6*, 133–136, doi:10.2151/sola.2010-034.
Klose, M., and Y. Shao (2012), Stochastic parameterization of dust emission and application to convective atmospheric conditions, *Atmos. Chem. Phys.*, *12*, 7309–7320, doi:10.5194/acp-12-7309-2012.
Klose, M., and Y. Shao (2013), Large-eddy simulation of turbulent dust emission, *Aeolian Res.*, *8*, 49–58, doi:10.1016/j.aeolia.2012.10.010.
Kok, J. F., and N. O. Renno (2009), A comprehensive numerical model of steady state saltation (COMSALT), *J. Geophys. Res.*, *114*, D17204, doi:10.1029/2009JD011702.
Kosovic, B. (1997), Subgrid-scale modelling for the large-eddy simulation of high-Reynolds-number boundary layers, *J. Fluid Mech.*, *336*, 151–182.
Li, J., G. S. Okin, J. E. Herrick, J. Belnap, and M. E. Miller (2013), Evaluation of a new model of aeolian transport in the presence of vegetation, *J. Geophys. Res. Earth Surf.*, *118*, 288–306, doi:10.1002/jgrf.20040.
Li, X. L., M. Klose, Y. Shao, and H. S. Zhang (2014), Convective turbulent dust emission (CTDE) observed over Horqin Sandy Land area and validation of a CTDE scheme, *J. Geophys. Res. Atmos.*, *119*, doi:10.1002/2014JD021572.
Loosmore, G. A., and J. R. Hunt (2000), Dust resuspension without saltation, *J. Geophys. Res.*, *105*(D16), 20,663–20,671, doi:10.1029/2000JD900271.
Marticorena, B., and G. Bergametti (1995), Modeling the atmospheric dust cycle: 1. Design of a soil-derived dust emission scheme, *J. Geophys. Res.*, *100*(D8), 16,415–16,430, doi:10.1029/95JD00690.
McKenna Neuman, C. (2003), Effects of temperature and humidity upon the entrainment of sedimentary particles by wind, *Boundary Layer Meteorol.*, *108*, 61–89.
McKenna Neuman, C., and W. G. Nickling (1989), A theoretical and wind tunnel investigation of the effect of capillary water on the entrainment of sediment by wind, *Can. J. Soil Sci.*, *69*, 79–96.
Mirocha, J. D., J. K. Lundquist, and B. Kosovic (2010), Implementation of a nonlinear subfilter turbulence stress model for large-eddy simulation in the Advanced Research WRF model, *Mon. Weather Rev.*, *138*, 4212–4228.
Moeng, C.-H., and P. P. Sullivan (1994), A comparison of shear- and buoyancy-driven planetary boundary layer flows, *J. Atmos. Sci.*, *51*, 999–1022.
Phillips, M. (1980), A force balance model for particle entrainment into a fluid stream, *J. Phys. D Appl. Phys.*, *13*, 221–233.
Raupach, M. R., D. A. Gilette, and J. F. Leys (1993), The effect of roughness elements on wind erosion threshold, *J. Geophys. Res.*, *98*(D2), 3023–3029, doi:10.1029/92JD01922.
Ravi, S., P. D'Odorico, T. M. Over, and T. M. Zobeck (2004), On the effect of air humidity on soil susceptibility to wind erosion: The case of air-dry soils, *Geophys. Res. Lett.*, *31*, L09501, doi:10.1029/2004GL019485.
Ravi, S., T. M. Zobeck, T. M. Over, G. S. Okin, and P. D'Odorico (2006), On the effect of moisture bonding forces in air-dry soils on threshold friction velocity of wind erosion, *Sedimentology*, *53*, 597–609, doi:10.1111/j.1365-3091.2006.00775.x.
Shao, Y. (2004), Simplification of a dust emission scheme and comparison with data, *J. Geophys. Res.*, *109*, D10202, doi:10.1029/2003JD004372.
Shao, Y. (2008), *Physics and Modelling of Wind Erosion*, 2nd ed., 452 pp., Springer, Berlin, Germany.
Shao, Y., and H. Lu (2000), A simple expression for wind erosion threshold friction velocity, *J. Geophys. Res.*, *105*, 22,437–22,443, doi:10.1029/2000JD900304.
Shao, Y., and Y. Yang (2008), A theory for drag partition over rough surfaces, *J. Geophys. Res.*, *113*, F02S05, doi:10.1029/2007JF000791.
Shao, Y., M. Ishizuka, M. Mikami, and J. F. Leys (2011), Parameterization of size-resolved dust emission and validation with measurements, *J. Geophys. Res.*, *116*, D08203, doi:10.1029/2010JD014527.
Stout, J. E., and T. M. Zobeck (1997), Intermittent saltation, *Sedimentology*, *44*, 959–970.
van Genuchten, M. T. (1980), A closed-form equation for predicting the hydraulic conductivity of unsaturated soils, *Soil Sci. Soc. Am. J.*, *44*, 892–898.
Webb, N. P., G. S. Okin, and S. Brown (2014), The effect of roughness elements on wind erosion: The importance of surface shear stress distribution, *J. Geophys. Res. Atmos.*, *119*, 6066–6084, doi:10.1002/2014JD021491.
Zeman, O., and H. Tennekes (1977), Parameterization of the turbulent energy budget at the top of the daytime atmospheric boundary layer, *J. Atmos. Sci.*, *34*, 111–123, doi:10.1175/1520-0469(1977)034<0111:POTTEB>2.0.CO;2.
Zender, C. S., H. Bian, and D. Newman (2003), Mineral Dust Entrainment and Deposition (DEAD) model: Description and 1990s dust climatology, *J. Geophys. Res.*, *108*(D14), 4416, doi:10.1029/2002JD002775.
Zimon, A. D. (1982), *Adhesion of Dust and Powder*, 438 pp., Consultants Bureau, New York.

5 CTDE observations in the Horqin Sandy Land area

Reference:

Li, X. L., M. Klose, Y. Shao, and H. S. Zhang (2014), Convective Turbulent Dust Emission (CTDE) observed over Horqin Sandy Land area and validation of a CTDE scheme, *J. Geophys. Res. Atmos.*, *119*, 9980–9992, doi: 10.1002/2014JD021572

AGU PUBLICATIONS

JGR

Journal of Geophysical Research: Atmospheres

RESEARCH ARTICLE
10.1002/2014JD021572

Key Points:
- Characteristics of CTDE events
- Seasonal variations of observed CTDE events
- Validation of a new CTDE scheme

Correspondence to:
H. S. Zhang,
hsdq@pku.edu.cn

Citation:
Li, X. L., M. Klose, Y. Shao, and H. S. Zhang (2014), Convective turbulent dust emission (CTDE) observed over Horqin Sandy Land area and validation of a CTDE scheme, *J. Geophys. Res. Atmos.*, *119*, doi:10.1002/2014JD021572.

Received 28 JAN 2014
Accepted 8 AUG 2014
Accepted article online 27 AUG 2014

Convective turbulent dust emission (CTDE) observed over Horqin Sandy Land area and validation of a CTDE scheme

X. L. Li[1], M. Klose[2], Y. Shao[2], and H. S. Zhang[1]

[1]Laboratory for Climate and Ocean-Atmosphere Studies, Department of Atmospheric and Oceanic Sciences, School of Physics, Peking University, Beijing, China, [2]Institute for Geophysics and Meteorology, University of Cologne, Cologne, Germany

Abstract In this paper, a data set obtained from a sandstorm monitoring station located in Horqin Sandy Land area in northern China from December 2010 to November 2011 is used to investigate the seasonal variations and characteristics of convective turbulent dust emission (CTDE) and to validate a CTDE scheme. The observations show that CTDE events occur during the local daytime, with 85% of them between 08:00 and 15:00 local standard time. While a CTDE event may last for 0.5 to 8 h, the duration of 79% of the events is shorter than 3 h. CTDE occurs most frequently in summer and then in fall, less frequently in spring, and least in winter. The total CTDE flux in the year ($=1.63\times10^4\ \mu g\ m^{-2}\ s^{-1}$) is considerable and important to the background dust concentration and dust cycles from the view of a longer time scale. The CTDE dust flux, F_{obs}, falls into the range of 0–30 $\mu g\ m^{-2}\ s^{-1}$ and is positively correlated with the convective scaling velocity, w_*, but not so much with the friction velocity, u_*. A CTDE event was observed on 14 October 2011, which lasted for 7 h with a maximum of $F_{obs}=9.4\ \mu g\ m^{-2}\ s^{-1}$. This event is used to validate the CTDE scheme. A linear relationship between the predicted and the observed CTDE dust fluxes is found, and an important model parameter is calibrated for this sandy land.

1. Introduction

Dust emission can be generated through three mechanisms, namely, aerodynamic lift, saltation bombardment, and aggregate disintegration [*Shao*, 2001]. Saltation bombardment and aggregate disintegration are the two major mechanisms included in most of the existing dust emission parameterization schemes [e.g., *Marticorena and Bergametti*, 1995; *Alfaro and Gomes*, 2001; *Shao*, 2001, 2004]. Dust emission arising from direct aerodynamic entrainment is usually an order of magnitude smaller than that caused by the other two mechanisms [*Shao et al.*, 1993; *Loosmore and Hunt*, 2000] and often neglected [*Marticorena and Bergametti*, 1995; *Marticorena et al.*, 1997; *Alfaro and Gomes*, 2001; *Laurent et al.*, 2006; *Park et al.*, 2010]. However, weak dust emissions in the absence of saltation can occur frequently because there are always free dust particles which can be blown off the surface even by weak winds [*Shao*, 2008]. In particular, over heated loose sandy surfaces in desert regions, convective turbulence can generate strong localized shear stresses which result in dust emission in the absence of saltation [*Klose and Shao*, 2012]. This mechanism is referred to by the latter authors as convective turbulent dust emission (CTDE). While strong dust events are important to episodic increases in atmospheric dust concentration, CTDE is arguably more important in maintaining the background dust concentration and the continuous dust supply to the ocean to sustain the ocean biomass productivity [*Klose and Shao*, 2013]. Thus, CTDE contributes to global dust variability mainly on seasonal, annual, or longer time scales [*Chkhetiani et al.*, 2012]. The importance of CTDE is however yet to be fully quantified.

Dust emission without saltation has been observed in field and wind tunnel experiments [*Gillette and Sinclair*, 1990; *Shao et al.*, 1993; *Gillette et al.*, 1997, 2004; *Loosmore and Hunt*, 2000; *Golitsyn et al.*, 2003; *Chkhetiani et al.*, 2012]. Most of the field experiments on CTDE are carried out in desert regions [e.g., *Gillette and Sinclair*, 1990; *Gillette et al.*, 1997]. *Golitsyn et al.* [2003] suggested that CTDE is related to the local circulation in the boundary layer caused by the surface temperature heterogeneity and possibly connected with the electrical charge of dust particles. *Chkhetiani et al.* [2012] found that under weak wind conditions ($u_*<0.30\ m\ s^{-1}$), the deviations of mass concentration of fine dusts (0.15–0.50 μm) from their background values, increased proportionally to the temperature drop between the surface and the air at 0.2 m with an exponent of about 0.5, based on the observational data from an extensive sand area in Kalmykia. However, there are rare long-term field observations of CTDE to study its seasonal evolution and its characteristics over different soil conditions.

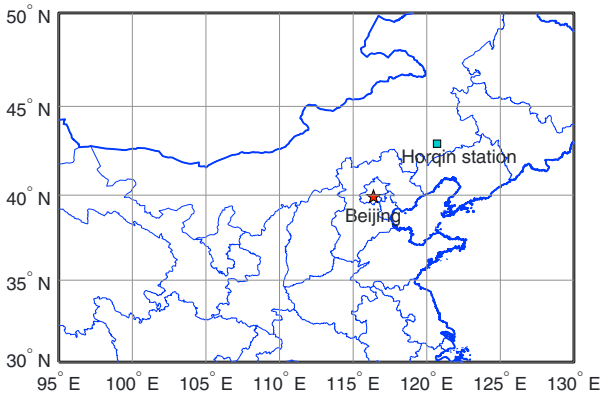

Figure 1. Location of the Horqin sandstorm monitoring station in Inner Mongolia of China.

The magnitude of dust emission by direct aerodynamic lift, F_a, is estimated in some dust emission schemes using empirical equations. For instance, the empirical equation, $F_a = au_*^n$, fitted by *Loosmore and Hunt* [2000] to their wind tunnel observations has been used by *Shao* [2004] and *Shao et al.* [2011], with $a = 3.6$ and $n = 3$ with the dimensions of u_* being (m s^{-1}) and of F_a (μg m^{-2} s^{-1}). It is noted that a and n must be different for different soil surfaces, and F_a a function of dust particle size, d. The empirical form of *Loosmore and Hunt* [2000] is very simple, but the empirical constants a and n are difficult to determine in general, and the wind tunnel experiments are only representative for neutral conditions. *Klose and Shao* [2012] recently developed a more comprehensive parameterization scheme of CTDE (CTDE scheme hereafter), which accounts for the stochastic nature of CTDE by using the statistical representations of soil particle size, interparticle cohesion, and instantaneous surface shear stress. This scheme can be used in regional and global atmospheric models [*Klose and Shao*, 2012, 2013]. Tests have been carried out to evaluate the CTDE scheme, and it has been found that the simulations using Weather Research and Forecasting/Chemistry combined with the CTDE scheme can capture the essence of the dust patterns and their diurnal variations [*Klose and Shao*, 2012]. The simulated results from a large-eddy dust model developed by *Klose and Shao* [2013] showed that large eddies can produce significant dust emissions along updraft convergence lines, at downdraft centers, and in areas of vortices. However, the CTDE scheme needs to be rigorously verified, especially as the magnitude of the simulated fluxes is subject to a model parameter which needs to be calibrated with reliable observations.

In this paper, a data set obtained from a sandstorm monitoring station located in Horqin Sandy Land area in northern China from December 2010 to November 2011 will be used to investigate the seasonal variations and characteristics of CTDE and to validate the CTDE scheme. In section 2, the information of the Horqin monitoring station and the data set are described, and several important parameters used in the study are calculated. In section 3, the characteristics of CTDE during a year and its relationship to u_* and w_* will be investigated and the CTDE scheme verified with the observations for several CTDE events. In section 4, conclusions and discussions are summarized.

2. Data and Method

2.1. Data Set From Horqin Station

A sandstorm monitoring station is located at Naiman Qi (42°56′N, 120°42′E) in Inner Mongolia of China and at the eastern edge of Horqin Sandy Land area (Figure 1). The main dust source region is extended to the west and north and an urban region at tens of kilometers to the south of the station. The mean annual precipitation in this region is about 300–400 mm, belonging to the semiarid climate.

The Horqin station has a 20 m observational tower, and the observations included wind direction, wind speed at heights of 2, 4, 16, and 20 m; air temperature and humidity at heights of 2, 4, 8, and 16 m; radiation components, soil moisture, and soil temperature at depths of 5, 20, and 50 cm; precipitation at surface, and dust (particulate matter 10 (PM_{10})) concentration at heights of 3 and 18 m. All the measurements were continuously recorded with a sample interval of 10 min, and then the original 10 min mean data were dealt with a procedure of 30 min running mean, because this duration is necessary for integrating the major time scales of turbulence occurring in the atmospheric surface boundary layer [*Wieringa*, 1993]. The detailed information about the observation items and instrument setting has been listed in *Li and Zhang* [2012].

2.1.1. Surface Cover

The Horqin Sandy Land area is covered by gentle undulating, shifting and semishifting dunes, and fixed dunes. The vegetation at the Horqin site consisted largely of low open shrubs dominated by *Caragana*

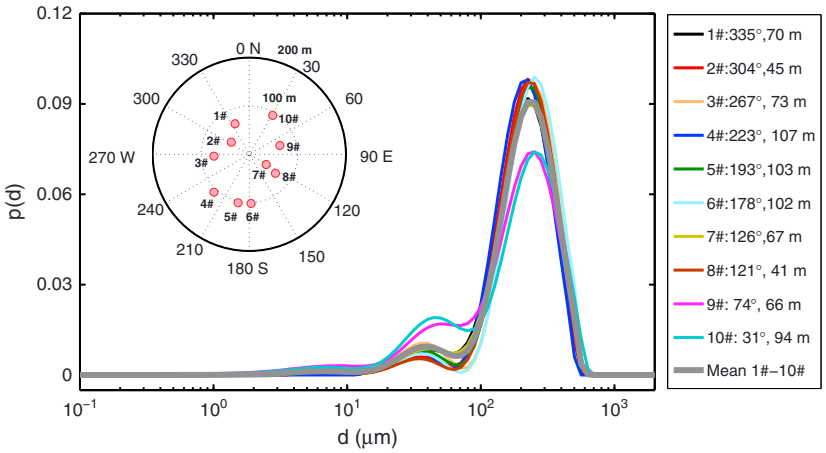

Figure 2. Minimally dispersed particle size distributions of the surface soil at the Horqin site. The right upper subplot shows the 10 positions where the samples were collected, relative to the observational tower at the center.

microphylla, *Salix gordejevii*, and *Artemisia halodendron* [*Zhao et al.*, 2007]. The vegetation condition at the site had improved year by year since the local government prohibited grazing from 2003. The average height of the vegetation during the observation period from December 2010 to November 2011 was about 30 cm and the fraction of roughness cover, c_f, about 0.5. While the vegetation appeared to be dense in the area around the station within a few hundred meters, the surface cover was heterogeneous with exposed patches of scale of 100 m. The vegetation over the larger area surrounding the site was generally poorer.

2.1.2. Particle Size Distribution

Surface soil samples were collected from 10 different positions around the site, as shown in Figure 2. Plant residue was first removed from the soil samples by sieving ($d > 2$ mm) before the minimally and fully dispersed soil mass/volume particle size distributions (psd) were analyzed in laboratory with a particle size analyzer based on laser diffraction light scattering technology (Mastersizer 2000, Malvern Ins., England), using methods A and B as described by *Shao et al.* [2011], respectively. In method A, water was used for sample dispersion with no application of ultrasonic action. In method B, sodium hexametaphosphate 0.2% solution was used for sample dispersion, and 60 s ultrasonic action was applied to the sample. Based on method A, the soil at the station is composed of 90.61% sand ($63 < d \leq 2000$ μm), 9.03% silt ($4 < d \leq 63$ μm), and 0.36% clay ($d \leq 4$ μm) on average, and it is regarded to be the minimally dispersed psd, $p_m(d)$, (Figure 2). Based on method B, the soil contains 86.73% sand, 11.34% silt, and 1.93% clay, and it is assumed to be the fully dispersed psd, $p_f(d)$ (not shown). Soil texture around the site was regarded as sand soil corresponding to $p_m(d)$ and loamy sand soil corresponding to $p_f(d)$, respectively, based on the United States Department of Agriculture classification. It is noted that only $p_m(d)$ is used in the CTDE scheme, because wind speed is usually weak during CTDE events, and the surface remains close to its natural condition as there is no substantial mechanical disturbance. However, some discrepancy still existed between the theoretical $p_m(d)$ and the measured one based on method A. But this discrepancy can be compensated with a smaller α_{N0}, an unknown model parameter that relates to the soil capability to generate CTDE and can be determined with observations.

The minimally dispersed soil psd $p_m(d)$ can be approximated as the sum of lognormal distributions:

$$d \times p_m(d) = \sum_{j=1}^{N} \frac{w_j}{\sqrt{2\pi}\sigma_j} \exp\left[-\frac{(\ln d - \ln D_j)^2}{2\sigma_j^2}\right] \quad (1)$$

where w_j is the weight for the jth mode of the psd and D_j and σ_j are the parameters for the lognormal distribution of the jth mode. These parameters in equation (1) were determined by fitting the averaged observed data (thick gray line in Figure 2) by using the robust fitting with bisquare weighting method in MATLAB software [*Klose et al.*, 2014] and has been listed in Table 1.

Table 1. Lognormal Distribution Parameters for the Minimally Dispersed Soil psd at the Horqin Site

$p_m(d)$	Mode1	Mode2	Mode3	Mode4
w	0.1909	0.0111	0.0965	0.7015
ln(D)	5.8134	1.8344	3.6682	5.3267
σ	0.2675	0.4357	0.4877	0.4003

It is to note that the CTDE scheme is sensitive to soil psd. The simulated CTDE flux increased by about 67% when the weight for the second mode w_2 increased and w_3 decreased to 0.01 in Table 1. This indicates the importance of using the real soil psd for CTDE simulation.

2.1.3. Surface Roughness Length

The aerodynamic roughness length, z_0, is derived by fitting the wind speed under near-neutral conditions to the logarithmic wind profile. Such conditions usually occurred with large wind speed and low-temperature gradient in the surface layer. The near-neutral data were selected with wind speed exceeding 4 m s^{-1} at 4 m height and the temperature difference between two adjacent observation heights (2, 4, 8, and 16 m for temperature) being less than 0.2°C, that is the accuracy of temperature measurement. Under the above circumstances, the bulk Richardson number R_i was estimated close to zero, representing the near-neutral atmospheric conditions.

$$R_i = \frac{g}{\overline{\theta}} \frac{\left(\partial \overline{\theta}/\partial z\right)}{\left(\partial \overline{U}/\partial z\right)^2} \tag{2}$$

where g (=9.8 m s^{-2}) is the gravitational acceleration and $\partial\overline{\theta}/\partial z$ and $\partial\overline{U}/\partial z$ are the gradients of the 30 min running mean potential temperature $\overline{\theta}$ and wind speed $\overline{U}$, respectively.

To explore the effects of wind direction and vegetation growth on z_0, z_0 was estimated separately for the prevailing wind directions (north and south) and different seasons (Figure 3). The values of z_0 under northerly wind directions did not change much during the year, on average ranging between 0.034 m in spring and 0.048 m in fall, while z_0 under southerly wind directions decreased from winter (0.153 m) to fall (0.076 m). The seasonal variation in z_0 values existed probably because the plants had more and larger leaves in fall with their growing during the year which resulted in a zero plane displacement d above the surface. However, the

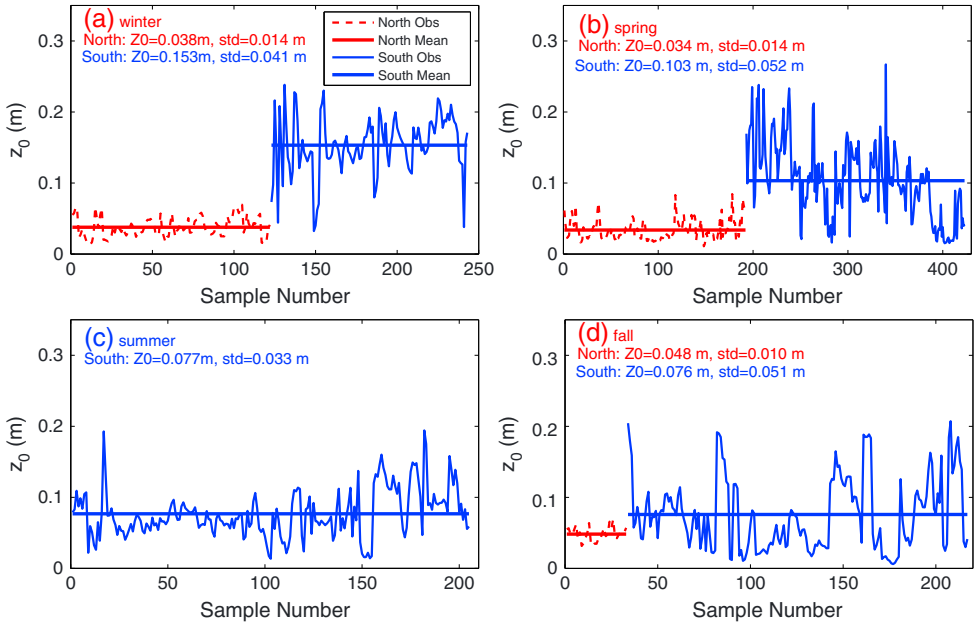

Figure 3. Roughness length z_0 at the Horqin site for southerly (wind direction from 90° to 270°) and northerly winds, derived from the wind profiles under near-neutral conditions in (a) winter (December, January, and February), (b) spring (March, April, and May), (c) summer (June, July, and August), and (d) fall (September, October, and November).

Table 2. Values of Roughness Length, z_0, and Their Standard Deviation for Different Seasons[a] and Wind Directions[b]

	Winter		Spring		Summer		Fall	
z_0 (m)	North	South	North	South	North[c]	South	North	South
Mean(z_0)	0.038	0.153	0.034	0.103	0.034	0.077	0.048	0.076
SD(z_0)	0.014	0.041	0.014	0.052		0.033	0.010	0.051

[a]Winter: December 2010 to February 2011, spring: March–May 2011, summer: June–August 2011, and fall: September–November 2011.
[b]South: wind direction between 90° and 270° and north otherwise.
[c]No samples of near-neutral conditions could be selected; z_0 under north wind conditions in summer was taken as that in spring.

value of d was very small compared with z_0 at the site; hence, d was set to be zero for the simplification of z_0 calculation, which contributed to a larger z_0, especially in fall. Additionally, the values of z_0 under northerly wind directions were smaller than those under southerly winds throughout the study period, which is much likely influenced by the conditions of the farmlands to the south. In conclusion, z_0 at the Horqin site is wind direction and season dependent, and the z_0 values used in this study are listed in Table 2.

2.1.4. Friction Velocity and Convective Velocity Scale

Using the 30 min running mean wind and temperature data, friction velocity, u_*, the scaling potential temperature, θ_*, and Obukhov length, L, can be computed following the Monin–Obukhov similarity theory using equations (3)–(5) [*Zhang et al.*, 2007].

$$u_* = \kappa \overline{U}(z)\left[\ln\left(\frac{z_u}{z_0}\right) - \Psi_M\left(\frac{z_u}{L}\right) + \Psi_M\left(\frac{z_0}{L}\right)\right]^{-1} \tag{3}$$

$$\theta_* = \kappa\left(\overline{\theta}_2 - \overline{\theta}_1\right)\left[\ln\left(\frac{z_{\theta 2}}{z_{\theta 1}}\right) - \Psi_H\left(\frac{z_{\theta 2}}{L}\right) + \Psi_H\left(\frac{z_{\theta 1}}{L}\right)\right]^{-1} \tag{4}$$

$$L = \frac{-\overline{\theta}u_*^3}{\kappa g\left(\overline{w'\theta'}\right)_s} = \frac{1}{2}\frac{\left(\overline{\theta_1} + \overline{\theta_2}\right)u_*^2}{\kappa g\theta_*} \tag{5}$$

where κ (=0.4) is the von Karman constant, $\overline{U}$ and $\overline{\theta}$ are the same as those in equation (2), Ψ_M and Ψ_H are the surface layer stability correction functions for momentum and heat, respectively, $\left(g/\overline{\theta}\right)\left(\overline{w'\theta'}\right)_s$ is the buoyancy heat flux at the surface, and z_a is the observational height of the quantity a. Here $z_{\theta 1} = 4$ m, $z_{\theta 2} = 16$ m, z_0 is the roughness length, and $z_u = 10$ m with $\overline{U}$ being the mean wind speed at 4 m and 16 m heights.

Convective velocity scale, w_*, can be calculated from

$$w_* = \left[gz_i\overline{\theta}\left(\overline{w'\theta'}\right)_s\right]^{1/3} = \left[-gz_i\overline{\theta}u_*\theta_*\right]^{1/3} \tag{6}$$

where z_i is the convective boundary layer height. For daytime, z_i was estimated by using the revised Carson scheme [*Carson*, 1973] and setting the initial boundary layer height z_{i0} as 300 m. This value was located in the middle of the z_{i0} range (200–450 m) determined based on the temperature soundings at 08:00 LST (local standard time, hereafter) at Tongliao station (42°16′N, 118°59′E) for 14 dust days in spring 2011 at Horqin [*Li and Zhang*, 2012].

Additionally, the sensible heat flux, H_s, can be calculated based on u_* and w_*:

$$H_s = -\rho c_p u_*\theta_* \tag{7}$$

where ρ is the air density and c_p (=1004.04 J kg^{-1} K^{-1}) is the specific heat at constant pressure. The bulk Richardson number R_i can also be written as the function of the ratio w_*/u_*, as $R_i = -\frac{kz\varphi_h}{z_i{\varphi_m}^2}\left(\frac{w_*}{u_*}\right)^3$, with φ_h and φ_m associated with the atmospheric stability z/L, and $z = 10$ m in this study.

2.1.5. Dust Emission Flux

With the assumption that the particles smaller than 10 μm are light enough to follow air movements perfectly [*Gillette et al.*, 1972; *Zhang et al.*, 2007; *Sow et al.*, 2009], dust emission flux, F_{obs}, can be calculated as

$$F_{\text{obs}} = \kappa u_*\left(\overline{C_2} - \overline{C_1}\right)\left[\ln\left(\frac{z_{c2}}{z_{c1}}\right) - \Psi_C\left(\frac{z_{c2}}{L}\right) + \Psi_C\left(\frac{z_{c1}}{L}\right)\right]^{-1} \tag{8}$$

where $\overline{C}$ is the 30 min running mean dust (PM_{10}) mass concentration, the observational heights $z_{c1} = 3$ m and $z_{c2} = 18$ m, and the function Ψ_C has the same expression form as Ψ_H.

2.2. Convective Turbulent Dust Emission Scheme

The CTDE scheme was developed by *Klose and Shao* [2012, 2013] and has been improved recently by *Klose et al.* [2014]. Dust emission can be generated when the aerodynamic lifting force, f, arising from the instantaneous surface shear stress overcomes the resistant forces of the interparticle cohesive force, f_i, and the gravitational force, f_g, acting on dust particles. Both f and f_i can be parameterized using probability density functions, i.e., $p(f)$ and $p(f_i)$ in the CTDE scheme. For given particular values of f and f_i, the modeled dust emission flux $\widetilde{F_{\mathrm{mod}}}$ can be calculated from

$$\widetilde{F_{\mathrm{mod}}} = \begin{cases} \dfrac{\alpha_N}{2\delta}\left[-w_t m_p + T_p\left(f - f_i\dfrac{d}{\delta}\right)\right], & f > f_g + f_i, \delta > d \\ 0 & else \end{cases} \tag{9}$$

with viscous sublayer thickness, δ, particle terminal velocity, w_t, particle mass, m_p, and particle response time, T_p. These model internal variables can be directly calculated in the model [*Klose and Shao*, 2012]. The parameter α_{N} (unit: m^{-2}) is the integrated particle number concentration over the viscous sublayer per unit area and is related to the dust particle size. The value of α_{N} is positively correlated with an empirical constant α_{N0} (unit: m^{-2}):

$$\alpha_N = \alpha_{N0}\left(\frac{d}{d_{\mathrm{ref}}}\right)^{-3} \tag{10}$$

where $d_{\mathrm{ref}} = 10\ \mu\mathrm{m}$ is the particle size for which the scheme is calibrated [*Klose et al.*, 2014]. The parameter α_{N0} represents the mean soil capability to release dusts during CTDE process to some extent and need to be calibrated with observations.

For given distribution functions for the lifting force $p(f)$ and interparticle cohesive force $p_j(f_i)$ corresponding to particle size d_j, dust emission flux can be obtained as

$$F_{\mathrm{mod},j} = \int_0^{\infty}\left[\int_0^{f}\widetilde{F_{\mathrm{mod}}}\cdot p_j(f_i)\cdot df_i\right]p(f)\cdot df \tag{11}$$

With particle size ranging from 0 to its maximum d_{max}, the dust emission flux F_{mod} is regarded as

$$F_{\mathrm{mod}} = \int_0^{d_{\mathrm{max}}} F_{\mathrm{mod},j}\, p_A(d_j)\cdot\delta d_j \tag{12}$$

where $d_{\mathrm{max}} = 20\ \mu\mathrm{m}$ in the current model version and $p_A(d_j)$ are the area particle size distribution obtained from known $p_m(d)$ in Table 1, as introduced by *Klose et al.* [2014], and δ indicates the differential.

In this study, the input parameters for the CTDE scheme are derived from field measurements, including the minimally dispersed particle size distribution $p_m(d)$, friction velocity u_*, convective velocity scale w_*, Obukhov length L, fraction of roughness cover c_f, as well as the soil water content (swc) (unit: $\mathrm{v\,v}^{-1}$) at 5 cm depth. Among these input parameters, w_*, u_*, and L are used to determine $p(f)$ that is followed as the Weibull distribution under different atmospheric stability conditions (represented with z/L) [*Klose and Shao*, 2013]; $p_m(d)$, c_f, and swc determine $p_j(f_i)$ together. All the input parameters were used directly or calculated with the 30 min running mean data.

3. Measurements of CTDE and Validation of the CTDE Scheme

3.1. Seasonal Variations of CTDE Control Parameters

Figure 4 shows the temporal variations of the convective velocity scale w_* and the sensible heat flux H_s from December 2010 to November 2011 at the Horqin site. Lower values of w_* and H_s occurred in winter with most of w_* values less than $1.5\ \mathrm{m\,s}^{-1}$ and H_s values below $200\ \mathrm{W\,m}^{-2}$ (w_* is set to zero for $H_s < 0$). Both w_* and H_s reached a minimum in January and then increased gradually with time. During summer, w_* and H_s were generally large but sometimes small during periods of rainfall or cloudy weather when short-wave solar

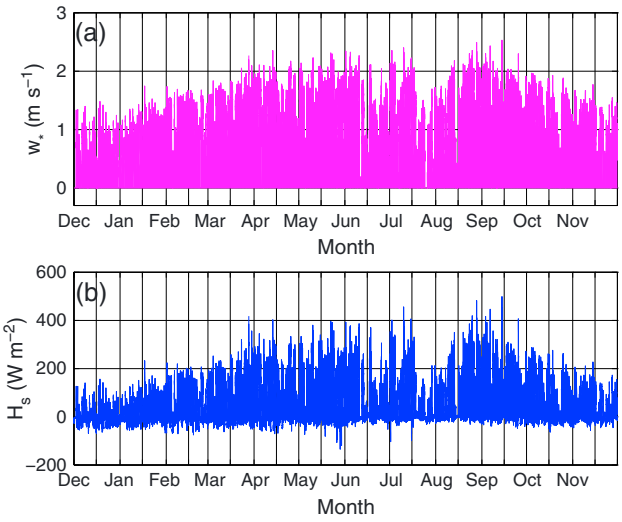

Figure 4. Temporal variations of (a) convective velocity scale w_* and (b) sensible heat flux H_s at the Horqin site from December 2010 to November 2011.

radiation at the surface was reduced and/or latent heat flux increased. The highest values of w_* (>2.5 m s^{-1}) and H_s (close to 500 W m^{-2}) occurred in late August and early September when the surface was warm and rainfall occurred less frequently.

The time series of friction velocity u_* and dust emission flux F_{obs} during the study period are shown in Figure 5. Dust emission occurred in every month of the year, but was most frequent in spring, mainly due to the strong spring wind. Negative F_{obs} usually means dust deposition, which occurred most frequently in summer, with the fraction of negative F_{obs} in the total summertime F_{obs} as 0.35. The lack of F_{obs} usually resulted from the failure of dust concentration measurements due to the power cut at the station or lower temperature environment (<−30°C) in winter. *Li and Zhang* [2012] obtained the relationship between the observed hourly mean F_{obs} and u_* as well as w_* during 14 dust emission events mainly caused by saltation bombardment and/or aggregate disintegration (Saltation-bombardment and/or aggregation-disintegration dust emission, written as SADE events hereafter) in spring 2011 at the same Horqin site. They fitted F_{obs} as positively correlated with the third power approximately of u_* and u_*' (=u_* + 0.08 w_*), that is a new velocity scale representing both dynamic and thermal effects by turbulence, in which w_* carries only a small weight. However, they did not explore these turbulent effects on CTDE events.

3.2. Characteristics of Observed CTDE at Horqin Site

3.2.1. Identification of CTDE Periods

Figure 6 shows the relationship between F_{obs} and u_* during a CTDE case occurred on 28 March 2011 and a SADE case on 31 March 2011. Obvious difference between the CTDE and SADE cases can be identified: (i) for the SADE case, dust emission occurred only for u_*, exceeding the threshold friction velocity, u_{*t}, which was estimated to be 0.40 m s^{-1} in this case by defining u_{*t} as the value of u_* when both of the dust concentration at 3 m height (not shown here) and F_{obs} begin to increase with increasing u_*, which lasts for half an hour at least, while for the CTDE case, dust was emitted also for u_* (0.20–0.40 m s^{-1}) smaller than u_{*t}; (ii) in the CTDE case, the intensity of dust emission was weaker and the duration shorter compared to the SADE case; the CTDE case lasted from 11:00 to 12:50 and the SADE case in periods of 10:00–12:10 and 17:00–20:00; and (iii) the CTDE case was accompanied by large sensible heat fluxes (shown as color bar).

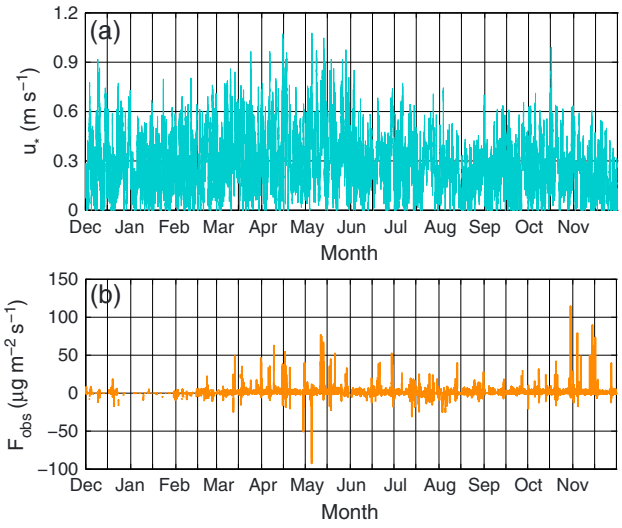

Figure 5. Same as Figure 4 but for (a) the friction velocity u_* and (b) the observed dust emission flux F_{obs}.

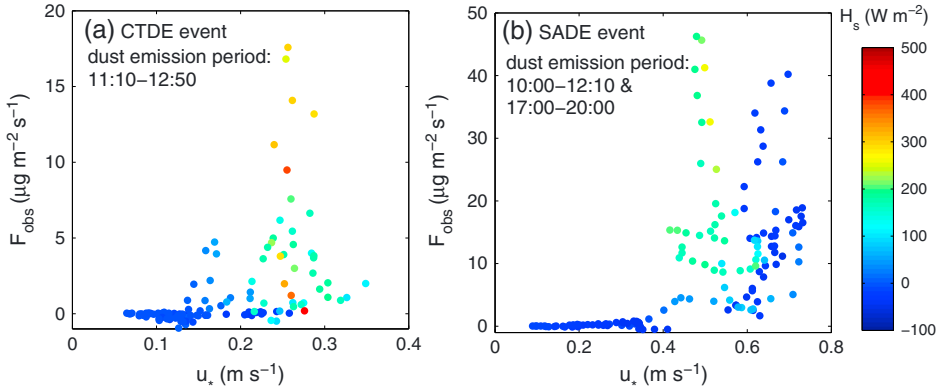

Figure 6. Scatterplots of dust flux, F_{obs}, against friction velocity, u_*, during (a) the CTDE case on 28 March and (b) the SADE case on 31 March 2011. The color bar represents the sensible heat flux.

Based on the basic characteristics of CTDE and SADE, the CTDE cases can therefore be identified using the criteria of (i) $u_* < u_{*t}$, in order to make sure that sand saltation cannot occur; (ii) $F_{obs} > 0\,\mu g\,m^{-2}\,s^{-1}$, for excluding the effects of dust advection and deposition; (iii) $w_* > 0\,m\,s^{-1}$, to guarantee the convective turbulent conditions; and (iv) dust concentration at 3 m height increased continuously for 30 min at least, which excludes those very short cases. Here the value of u_{*t} in the first criteria was taken as $0.40\,m\,s^{-1}$, which is the lowest value of u_{*t} ($0.40–0.65\,m\,s^{-1}$) for 14 SADE events in spring 2011 determined based on the aforementioned u_{*t} definition. The detailed information about the 14 SADE events can be found in *Li and Zhang* [2012]. Finally, a total of 505 CTDE events were identified at the Horqin site for the study period.

Similarly, the criteria for SADE cases were also given, including $u_* > u_{*t}$, where u_{*t} is taken as $0.50\,m\,s^{-1}$, in the middle of the u_{*t} range, as well as the same second and fourth rules for CTDE cases above. A total of 262 SADE cases were selected eventually, while only 19 SADE events lasted longer than 3 h.

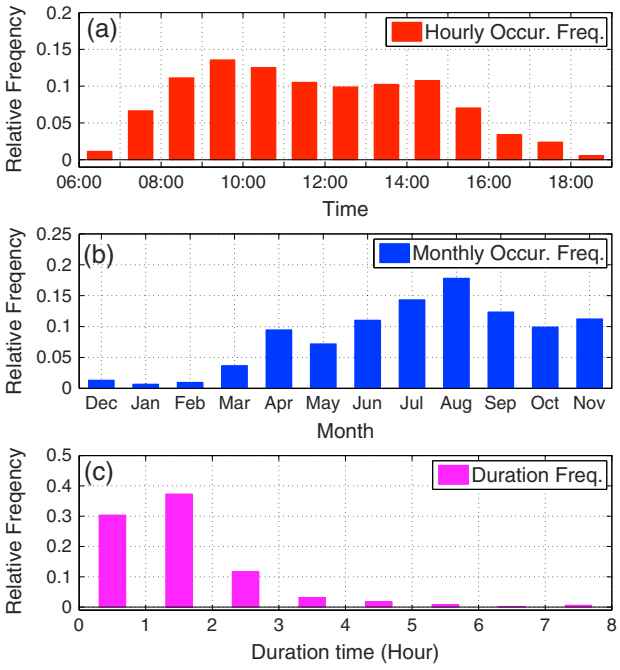

Figure 7. The relative distribution of the (a) hourly and (b) monthly occurrence frequency of CTDE events from December 2010 to November 2011 and (c) their durations.

3.2.2. Statistics of CTDE Events

Figure 7 shows the relative distribution of the hourly occurrence frequency, f_h, and the monthly occurrence frequency, f_m, of the CTDE events as well as their durations. The f_h is defined as

$$f_h(i) = \frac{N_{hi}}{N_t} \tag{13}$$

where N_{hi} is the number of the CTDE data points located the ith hour ($i = 1, 2, \ldots 24$), N_t ($= 4647$, one point per 10 min) is the total number of the CTDE data points. Similarly, f_m, is defined as

$$f_m(j) = \frac{N_{mj}}{N_t} \tag{14}$$

where N_{mj} is the number of CTDE data points located in the jth month, $j = 1, 2, \ldots 12$.

It is found that CTDE events might occur during the period between 06:00 and

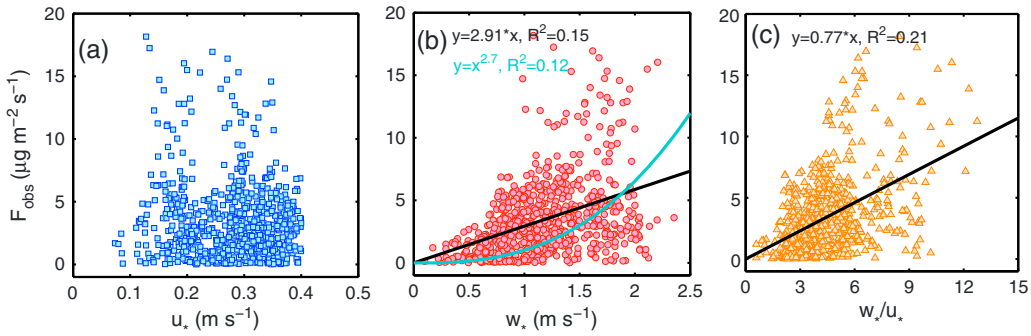

Figure 8. The relationships of (a) F_{obs}—u_*, (b) F_{obs}—w_*, and (c) F_{obs}—w_*/u_* for the CTDE events that started to develop in the time period 06:00–08:00 with initial $|F_{obs}| < 1.0\,\mu g\,m^{-2}\,s^{-1}$. The fitting results and correlation coefficients of F_{obs} and w_* as well as F_{obs} and w_*/u_* are shown.

19:00, but mostly between 08:00 and 15:00 with the sum of f_h over the time period exceeding 85% (Figure 7a). The duration of the CTDE events was usually less than 3 h; the most frequent duration was 1–2 h with a frequency of 37%, the next most frequent was 0.5–1 h (30%) (Figure 7c). It is found in Figure 7b that CTDE can occur throughout the year, with the highest f_m in summer (June, July, and August). CTDE events occurred less frequently in fall (September, October, and November) and then in spring (March, April, and May), although sensible heat fluxes appeared larger than that in summer (Figure 4b). The reason for this is that dust events were overwhelmingly attributed to SADE in spring and fall due to strong wind, making purely CTDE events less frequent. The smallest f_m occurred in winter (December, January, and February), mainly due to the frozen soil which effectively suppressed all the types of dust emission [*Li and Zhang*, 2012].

To be sure, the cumulative occurrence time of all CTDE cases during the year was as 1.9 times longer as that of SADE cases, and the cumulative dust emission flux of all CTDE cases ($1.63 \times 10^4\,\mu g\,m^{-2}\,s^{-1}$) was slightly smaller than that of SADE cases ($1.94 \times 10^4\,\mu g\,m^{-2}\,s^{-1}$). This indicates that CTDE is very significant for the regional and global dust cycle from the view of a longer time scale and should be paid more attention to in the future.

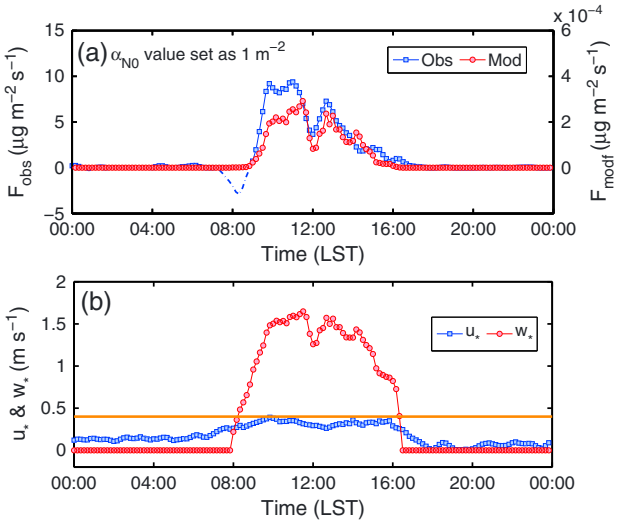

Figure 9. Variations in (a) the false modeled dust emission flux F_{modf} with setting $\alpha_{N0} = 1\,m^{-2}$ and the observed one F_{obs} and (b) u_* and w_* during the CTDE event on 14 October 2011.

3.2.3. Relationship of F_{obs} and w_*, u_* During CTDE Cases

Figure 8 shows the scatterplots of F_{obs}—u_*, F_{obs}—w_*, and F_{obs}—w_*/u_* for the CTDE events that began between 06:00 and 08:00. The selected events satisfy the requirement that F_{obs} at the start of the event was close to zero ($<1.0\,\mu g\,m^{-2}\,s^{-1}$), in order to exclude the effects arising from dust advection and deposition. The relationship between F_{obs} and u_* for CTDE cases was not as obvious as that for SADE cases, in which F_{obs} is usually observed to be positively correlated with the power of u_*. This result implies that CTDE is less related to the mean wind shear (Figure 8a). Unlike the relationship between F_{obs} and u_*, a positive correlation of F_{obs}—w_* can be seen in Figure 8b. F_{obs} was mostly less than $3.0\,\mu g\,m^{-2}\,s^{-1}$ for $w_* < 0.5\,m\,s^{-1}$, while for $w_* > 1.0\,m\,s^{-1}$,

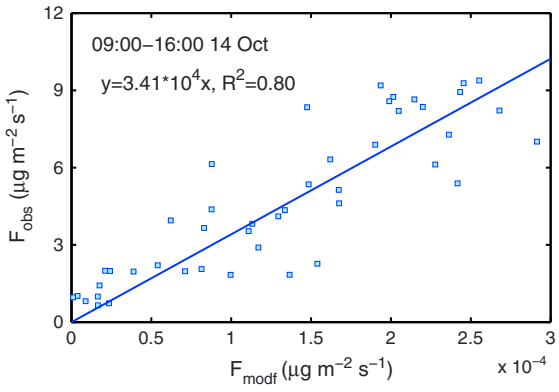

Figure 10. Comparison between F_{modf} with setting $\alpha_{N0} = 1$ and F_{obs} during the CTDE event on 14 October 2011.

F_{obs} frequently exceeded 10.0 μg m^{-2} s^{-1}. Two fitting equations were given in Figure 8b, one is $F_{obs} = 2.91 \times w_*$ with the correlation coefficient $R^2 = 0.15$ and the other $F_{obs} = w_*^{2.7}$ with $R^2 = 0.12$. Although the data points appeared scattering, it still confirmed the hypothesis that strong convective turbulence can generate dust emission. Meanwhile, it was also found that F_{obs} increased with w_*/u_* basically with most of the w_*/u_* values ranging between 3 and 6 (Figure 8c). The fitting equation was also given as $F_{obs} = 0.77 \times w_*/u_*$ with $R^2 = 0.21$. This means that CTDE tends to develop under unstable atmospheric conditions; larger w_*/u_* values correspond to smaller negative R_i values.

3.3. Validation of CTDE Scheme With Observation

A CTDE event occurred on 14 October 2011. This event had a long duration of 7 h from 09:00 to 16:00. It can be found in Figure 9b that $u_* < 0.4$ m s^{-1} (yellow line) and $w_* > 0$ m s^{-1} during the CTDE event, and the maximum w_* was 2.4 m s^{-1}. Figure 9a shows the variations of the observed dust emission flux, F_{obs}, and the false modeled one, F_{modf}, with setting $\alpha_{N0} = 1$ during this CTDE event. It can be found that the simulated results well reflected the variation of F_{obs},; however, the magnitude of F_{modf} was much smaller than that of F_{obs} before α_{N0} was calibrated. CTDE started to develop at about 09:00 and remained significant from 10:00 to 11:30. A second peak of CTDE occurred at about 13:00. The negative F_{obs} values (dashed line in Figure 9a) before the CTDE event started represented the dust deposition, but the deposition was weak and only lasted for a short time period.

The parameter α_{N0} represents the mean soil capability to release dusts during CTDE process to some extent. Hence, the value of α_{N0} should be different under various dust source regions. Now it is urgently required to determine α_{N0} at the Horqin Sand Land area at first, by estimating the ratio of F_{obs}/F_{modf}. Figure 10 shows the

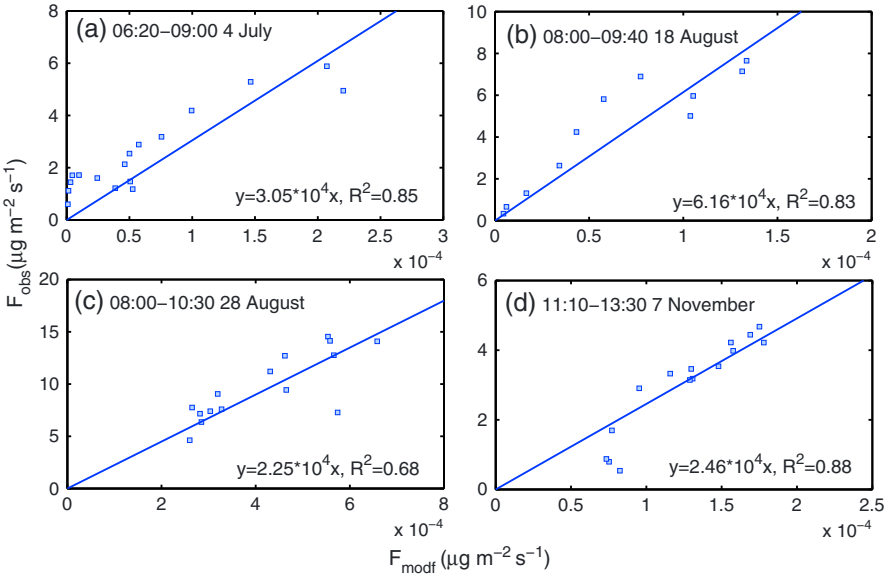

Figure 11. Same as Figure 10 but for the CTDE events occurred during (a) 06:20–09:00 on 4 July, (b) 08:00–09:40 on 18 August, (c) 08:00–10:30 on 28 August, and (d) 11:10–13:30 on 7 November 2011, respectively.

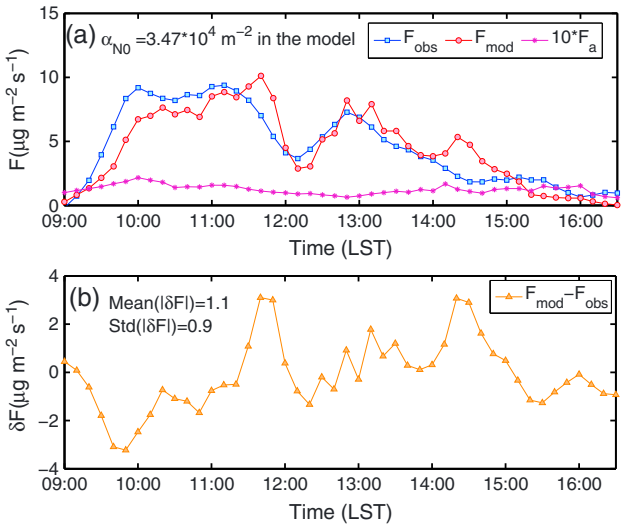

Figure 12. (a) Comparison between F_{mod} and F_{obs} values as well as 10 times of the results from the empirical equation $F_a = 3.6\times u_*^3$ and (b) the difference between F_{mod} and F_{obs} during the CTDE event on 14 October 2011, with setting $\alpha_{N0} = 3.47\times10^4\ m^{-2}$ in the model.

comparison between F_{obs} and F_{modf} for the CTDE event from 09:00 to 16:00 on 14 October 2011. A linear relationship between the F_{obs} and F_{modf} values has been found

$$F_{obs} = 3.41\times10^4 F_{modf} \quad (15)$$

with the correlation coefficient $R^2 = 0.80$. Hence, the value of α_{N0} was determined to be $3.41\times10^4\ m^{-2}$ for the CTDE case on 14 October 2011 at Horqin. This value is much higher than the preliminary estimate of $\alpha_N = 785.2\ m^{-2}$, which was estimated by the comparison of modeled dust concentration with lidar observations in the Taklimakan Desert [*Klose and Shao*, 2012]. However, this value is not recommended anymore, because the CTDE scheme has been updated at some aspects such as the calculation of $p(f)$, and the lidar data have large uncertainties [*Klose et al.*, 2014].

In order to verify the α_{N0} value derived from the 14 October 2011 CTDE case, four more events, occurred, respectively, during 06:20–09:00 on 4 July, 08:00–09:40 on 18 August, 08:00–10:30 on 28 August, and 11:10–13:30 on 7 November 2011, have been analyzed (Figure 11). These events occurred in summer and fall when CTDE usually occurs. Based on the same method to determine α_{N0}, for these four CTDE cases, the values of α_{N0} varied from $2.25\times10^4\ m^{-2}$ for the 18 November case to $6.16\times10^4\ m^{-2}$ for the 28 August case, and their R^2 values mostly reached 0.80 (Figure 11). Therefore, the order of the α_{N0} magnitude at Horqin can be sure to be 10^4, and the averaged α_{N0} ($3.47\times10^4\ m^{-2}$) of all the five CTDE cases was determined to be used in the CTDE scheme for Horqin Sandy Land area.

Figure 12a shows the variations of F_{obs} and the modeled result F_{mod} with setting α_{N0} to be $3.47\times10^4\ m^{-2}$ during the 14 October case. The temporal evolution of this CTDE event is well reproduced by simulation, and the values of F_{mod} were close to F_{obs} at most of the time. Meanwhile, the aforementioned empirical equation $F_a = 3.6\times u_*^3$ was also used to estimate the CTDE flux during the 14 October case. It is to note that F_a has been amplified 10 times in Figure 12a because it was too small to see clearly. It can be found that the result from this empirical equation substantially underestimated and hardly reflected the variation of F_{obs}, because CTDE flux indeed has no obvious relationship with u_* at all (as shown in Figure 8a).

Figure 12b shows the discrepancies between F_{mod} and F_{obs} during the CTDE period 09:00–16:00 on 14 October 2011. The discrepancies exist in particular appears to be a phase difference between the model and the observations. For this case, the predicted emission was slightly lower than the observed. At about 14:20, an emission maximum was predicted but not observed. An overall good agreement between the model and the observations has been achieved. The absolute difference between F_{mod} and F_{obs}, $|\delta F|$, was mostly less than $4.0\ \mu g\ m^{-2}\ s^{-1}$, and the mean $|\delta F|$ value was $1.1\ \mu g\ m^{-2}\ s^{-1}$. Additionally, the modeled results of the other four CTDE cases with $\alpha_{N0} = 3.47\times10^4\ m^{-2}$ were also good. The mean value of $|\delta F|$ was the smallest for the 4 July case ($0.9\ \mu g\ m^{-2}\ s^{-1}$) and the largest for the 28 August case ($4.6\ \mu g\ m^{-2}\ s^{-1}$), as shown in Table 3.

Table 3. Difference Between F_{mod} and F_{obs} During Four CTDE Events With Setting $\alpha_{N0} = 3.47\times10^4\ m^{-2}$ in the Model

δF ($\mu g\ m^{-2}\ s^{-1}$)	4 Jul	18 Aug	28 Aug	7 Nov
Mean($\|\delta F\|$)	0.9	2.0	4.6	1.4
SD$\|\delta F\|$	0.6	1.3	2.7	0.5

4. Conclusions and Discussions

Convective turbulent dust emission (CTDE) is an important form of aerodynamic dust emission by turbulence, which may profoundly influence the regional and global dust budgets on seasonal, annual, or longer time scales. In this paper, a data set from a sandstorm monitoring station located in Horqin Sandy Land area from December 2010 to November 2011 was used to investigate the seasonal variations and characteristics of CTDE and to validate the CTDE scheme improved recently by *Klose et al.* [2014].

A total of 505 CTDE events were identified based on the criteria of $u_* < u_{*t}$ ($=0.40\,\mathrm{m\,s^{-1}}$), $F_{obs} > 0\,\mu\mathrm{g\,m^{-2}\,s^{-1}}$, and $w_* > 0\,\mathrm{m\,s^{-1}}$, as well as that the dust concentration at the lower level increased during CTDE periods which lasted at least for 30 min. The observations showed that CTDE occurred during local daytime between 06:00 and 19:00, with 85% between 08:00 and 15:00. The duration of the CTDE events ranged from 0.5 to 8 h but of 79% shorter than 3 h. CTDE occurred most frequently in summer and then in fall, less frequently in spring and least in winter. The order of the magnitude of CTDE fluxes was mostly 0–10 $\mu\mathrm{g\,m^{-2}\,s^{-1}}$, typically several $\mu\mathrm{g\,m^{-2}\,s^{-1}}$ and at times up to 30 $\mu\mathrm{g\,m^{-2}\,s^{-1}}$. F_{obs} had a good positive correlation with the atmospheric stability, represented by, e.g., w_* or w_*/u_*, but no clear correlation with u_*. F_{obs} was generally less than 3.0 $\mu\mathrm{g\,m^{-2}\,s^{-1}}$ when $w_* < 0.5\,\mathrm{m\,s^{-1}}$ and increased with w_*; for $w_* > 1.0\,\mathrm{m\,s^{-1}}$, F_{obs} exceeded 10.0 $\mu\mathrm{g\,m^{-2}\,s^{-1}}$. A CTDE event was observed on 14 October 2011 in Horqin Sandy Land area, which lasted for 7 h with a maximum of $F_{obs} = 9.4\,\mu\mathrm{g\,m^{-2}\,s^{-1}}$. This event was used to validate the CTDE scheme. A linear relationship was found between the predicted and observed dust fluxes. From the F_{obs}/F_{modf} ratio, the model parameter α_{N0} was estimated to be $3.41 \times 10^4\,\mathrm{m^{-2}}$ for Horqin Sandy Land area. The performance of the CTDE scheme was verified with four other CTDE cases, which yielded the values of α_{N0} ranging from 2.25×10^4 to $6.16 \times 10^4\,\mathrm{m^{-2}}$. The mean value of $\alpha_{N0} = 3.47 \times 10^4\,\mathrm{m^{-2}}$ is then used in the model to predict the 14 October case. Although discrepancies exist, a good overall agreement between the CTDE and the observations is found.

The results quantitatively indicate the significant importance of CTDE to the regional and global dust cycles from the view of a longer time scale. The cumulative CTDE occurrence time during the year was as 1.9 times longer as that of SADE cases, and the cumulative CTDE flux ($1.63 \times 10^4\,\mu\mathrm{g\,m^{-2}\,s^{-1}}$) was considerable in comparison with SADE flux ($1.94 \times 10^4\,\mu\mathrm{g\,m^{-2}\,s^{-1}}$). In relative dust research, CTDE should be paid more attention to in the future.

Acknowledgments

This work was jointly funded by the National Program on Key Basic Research Project of China (973) (2010CB428501), R&D Special Fund for Public Welfare Industry (meteorology) by Ministry of Finance and Ministry of Science and Technology (GYHY201006014), the National Natural Science Foundation of China (41475007), as well as the Research Fund for the Doctoral Program of Higher Education (20110001130010). The work was also supported by the PhD Students' Short-term Overseas Research Program from the Graduate School of the Peking University. We wish to thank L. P. Zhou, School of Earth and Space Sciences, Peking University, for helping us in measuring the soil particle size distributions. Users can access the field data from the paper at request by the corresponding author (e-mail: hsdq@pku.edu.cn).

References

Alfaro, S. C., and L. Gomes (2001), Modeling mineral aerosol production by wind erosion: Emission intensities and aerosol size distributions in source areas, *J. Geophys. Res.*, *106*(D16), 18,075–18,084, doi:10.1029/2000JD900339.

Carson, D. J. (1973), The development of a dry, inversion-capped, convectively unstable boundary layer, *Q. J. R. Meteorol. Soc.*, *99*, 450–467.

Chkhetiani, O. G., E. B. Gledzer, M. S. Artamonova, and M. A. Iordanskii (2012), Dust resuspension under weak wind conditions: Direct observations and model, *Atmos. Chem. Phys.*, *12*, 5147–5162, doi:10.5194/acp-12-5147-2012.

Gillette, D. A., and P. C. Sinclair (1990), Estimation of suspension of alkaline material by dust devils in the United States, *Atmos. Environ., Part A*, *24*(5), 1135–1142.

Gillette, D. A., I. H. Blifford, and C. R. Fenster (1972), Measurements of aerosol size distributions and vertical fluxes of aerosols on land subject to wind erosion, *J. Appl. Meteorol.*, *11*, 977–987.

Gillette, D. A., D. W. Fryrear, T. E. Gill, T. Ley, T. A. Cahill, and E. A. Gearhart (1997), Relation of vertical flux of particles smaller than 10 μm to total aeolian horizontal mass flux at Owens Lake, *J. Geophys. Res.*, *102*(D22), 26,009–26,015, doi:10.1029/97JD02252.

Gillette, D. A., R. E. Lawson Jr., and R. S. Thompson (2004), A "test of concept" comparison of aerodynamic and mechanical resuspension mechanisms for particles deposited on field rye grass (*Secale cercele*). Part 1. Relative particle flux rates, *Atmos. Environ.*, *38*, 4789–4797.

Golitsyn, G. S., I. G. Granberg, A. V. Andronova, V. M. Ponomarev, S. S. Zilitinkevich, V. V. Smirnov, and M. Y. Yablokov (2003), Investigation of boundary layer fine structure in arid regions, *Water Air Soil Pollut. Focus*, *3*(2), 245–257, doi:10.1023/A:1023207027200.

Klose, M., and Y. Shao (2012), Stochastic parameterization of dust emission and application to convective atmospheric conditions, *Atmos. Chem. Phys.*, *12*, 7309–7320, doi:10.5194/acp-12-7309-2012.

Klose, M., and Y. Shao (2013), Large-eddy simulation of turbulent dust emission, *Aeolian Res.*, *8*, 49–58.

Klose, M., Y. P. Shao, X. L. Li, H. S. Zhang, M. Ishizuka, M. Mikami, and J. F. Leys (2014), Further development of a parameterization for convective turbulent dust emission and evaluation based on field observations, *J. Geophys. Res. Atmos.*, doi:10.1002/2014JD021688.

Laurent, B., B. Marticorena, G. Bergametti, and F. Mei (2006), Modeling mineral dust emissions from Chinese and Mongolian deserts, *Global Planet. Change*, *52*(1–4), 121–141.

Li, X. L., and H. S. Zhang (2012), Temporal variations in dust concentration and dust emission observed over Horqin Sandy Land area from December 2010 to November 2011, *Atmos. Environ.*, *61*, 56–65.

Loosmore, G. A., and J. R. Hunt (2000), Dust resuspension without saltation, *J. Geophys. Res.*, *105*(D16), 20,663–20,672, doi:10.1029/2000JD900271.

Marticorena, B., and G. Bergametti (1995), Modeling the atmospheric dust cycle: 1. Design of a soil-derived dust emission scheme, *J. Geophys. Res.*, *100*(D8), 16,415–16,430, doi:10.1029/95JD00690.

Marticorena, B., G. Bergametti, B. Aumont, Y. Callot, C. N'Doumé, and M. Legrand (1997), Modeling the atmospheric dust cycle: 2. Simulation of Saharan dust sources, *J. Geophys. Res.*, *102*(D4), 4387–4404, doi:10.1029/96JD02964.

Park, S. U., A. Choe, E. H. Lee, M. S. Park, and X. Song (2010), The Asian Dust Aerosol Model 2 (ADAM2) with the use of Normalized Difference Vegetation Index (NDVI) obtained from the Spot4/vegetation data, *Theor. Appl. Climatol.*, *101*, 191–208, doi:10.1007/s00704-009-0244-4.

Shao, Y. (2001), A model for mineral dust emission, *J. Geophys. Res.*, *106*(D17), 20,239–20,254, doi:10.1029/2001JD900171.

Shao, Y. (2004), Simplification of a dust emission scheme and comparison with data, *J. Geophys. Res.*, *109*, D10202, doi:10.1029/2003JD004372.

Shao, Y. (2008), *Physics and Modelling of Wind Erosion*, Atmos. Oceanogr. Sci. Libr., vol. 37, Kluwer Acad., Dordrecht, Netherlands.

Shao, Y., M. R. Raupach, and P. A. Findlater (1993), Effect of saltation bombardment on the entrainment of dust by wind, *J. Geophys. Res.*, *98*(D7), 12,719–12,726, doi:10.1029/93JD00396.

Shao, Y., M. Ishizuka, M. Mikami, and J. F. Leys (2011), Parameterization of size-resolved dust emission and validation with measurements, *J. Geophys. Res.*, *116*, D08203, doi:10.1029/2010JD014527.

Sow, M., S. C. Alfaro, J. L. Rajot, and B. Marticorena (2009), Size resolved dust emission fluxes measured in Niger during 3 dust storms of the AMMA experiment, *Atmos. Chem. Phys.*, *9*(12), 3881–3891, doi:10.5194/acp-9-3881-2009.

Wieringa, J. (1993), Representative roughness parameters for homogeneous terrains, *Boundary Layer Meteorol.*, *63*, 323–363.

Zhang, H. S., H. Zhu, Y. Peng, L. Kang, J. Chen, and S.-U. Park (2007), Experiment on dust flux during dust storm periods over sand desert area, *Acta Meteorol. Sin.*, *22*(2), 239–247.

Zhao, H. L., R. L. Zhou, Y. Z. Su, H. Zhang, L. Y. Zhao, and S. Drake (2007), Shrub facilitation of desert land restoration in the Horqin sand land of Inner Mongolia, *Ecol. Eng.*, *31*(1), 1–8.

6 Relevance of CTDE in the Earth system

The previous Chapters showed that CTDE occurs frequently under convective atmospheric conditions and produces dust emission fluxes of the order of $1\text{ - }100\,\mu\mathrm{g\,m^{-2}\,s^{-1}}$. Compared to SADE, which can be of the order of magnitude $1000\,\mu\mathrm{g\,m^{-2}\,s^{-1}}$ (e.g. *Gillette*, 1977; *Nickling and Gillies*, 1993; *Ishizuka et al.*, 2014) at intermediate to high friction velocities (e.g. $u_* > 0.4\,\mathrm{m^{-1}s^{-2}}$), these amounts appear to be small. We hypothesized that the long-term contribution of CTDE to the regional or global dust budget may nevertheless be significant, because it occurs more frequently than SADE, e.g. everyday in arid regions in summer. Hence, the relevance of CTDE in the Earth system remains to be assessed.

The long-term investigation of CTDE based on observational data is difficult in particular at the regional to global scales. The CTDE dust load is arguably too low to be recognized in satellite imagery or if high enough, cannot be distinguished from SADE dust load. In situ observations of CTDE are typically based on several assumptions, for example horizontal homogeneity, predefined vertical concentration profiles, etc., depending on the instruments used. Further, in situ observations would be site specific and provide a poor indicator of the long-term budget and regional or global significance of CTDE. From their observations, *Li et al.* (2014) found that the occurrence time of CTDE was about twice that of SADE and the accumulated CTDE flux was approximately 84 % compared to the SADE flux, suggesting that both mechanisms are important. However, these results may vary for different regions.

Here we apply our newly developed CTDE model to estimate a regional long-term CTDE budget. Using a modeling approach has the advantages of a high temporal resolution, flexible domain size, and availability of 3D/4D fields of all atmospheric/land-surface quantities of interest. There are of course also several constraints: (1) Results are subject to the validity of the model; (2) The model results are highly sensitive to the input data, e.g. vegetation cover, soil texture, atmospheric fields; (3) The model resolution may influence the atmospheric flow fields, e.g. through inappropriate representation of topography, leading to biased atmospheric conditions. In case of the CTDE model, constraint (1) mainly refers to the model parameter α_{N0} and to the correction methods for moisture and roughness effects. α_{N0} changes the emissions only proportionally rather than affecting their spatial distribution and relative spatial intensity. The roughness and moisture corrections affect both amount and spatial distribution of emissions. As the roughness correction method has not been validated so far, roughness effects are only accounted for in terms of vegetation cover fraction (*Klose et al.*, 2014a, Eq. 30). The remaining roughness corrections are not used for the budget study presented here. Their inclusion would potentially yield a spatial redistribution and reduction of dust emissions in some areas. The moisture correction proposed by *Klose et al.* (2014a) is used for the dust budget estimation, although it has only been tested against a small dataset. Soil moisture is, however, more dynamically variable compared to vegetation roughness elements and we thus consider the results with moisture correction more robust than without.

6.1. Dust event time series

Australia was chosen as the study region. The Australian topography is relatively smooth compared to e.g. North Africa or Asia and there exists a well-established dust-observation network (*Leys et al.*, 2008). *Shao et al.* (2013) analyzed 3- to 6-hourly synoptic records from the global Met Office Integrated Data Archive System (MIDAS) Land and Marine Surface Stations data (*UK Meteorological Office*, 2013), available from the British Atmospheric Data Centre (BADC). The authors calculated the time series of dust event frequency for a 39-year period for weak dust events (dust in suspension and blowing dust, present weather code ww = 6, 7), strong dust events (dust storm, ww = 9, 30 - 32, and severe dust storm, ww = 33 - 35) and other dust events (dust devil, ww = 8, thunderstorm with dust, ww = 98, and dust events during the past 3 or 6 hours, past weather code W_1 or $W_2 = 3$). We used this dataset and the analysis methods of *Shao et al.* (2013) in this study to select a time period for model simulation. To identify a time period with active CTDE, the

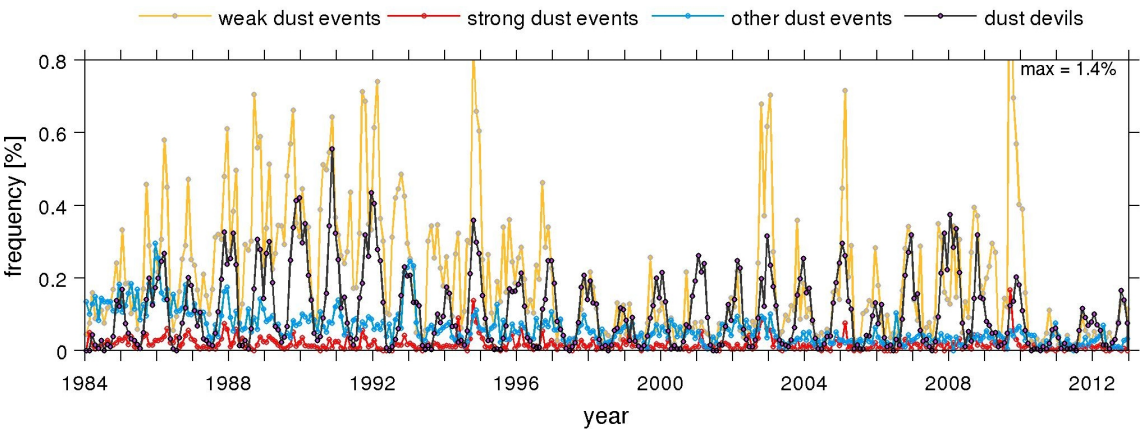

Fig. 6.1.: Time series of dust event frequency calculated from synoptic station data following *Shao et al.* (2013). Dust events are categorized based on present weather (ww) and past weather (W_1, W_2) reports into (1) dust in suspension and blowing dust (ww = 6, 7); (2) dust storm events (ww = 9, 30 - 35); (3) thunderstorm with dust storm or dust storm during last 3 or 6 hours (ww = 98, W_1 or W_2 = 3); (4) dust devils (ww = 8).

monthly mean frequency of ww = 8 (dust devils) has been computed separately. Only the stations that were available already in 1984 were used for calculation of the time series to avoid biases resulting from a varying number of stations. See *Shao et al.* (2013) for detailed information on the dataset used, the analysis method and uncertainty discussions. Although CTDE is not conclusively represented by dust devils, reports of the latter are used here as an indicator of CTDE strength. This approximation is justified, as dust devils are part of CTDE.

Figure 6.1 shows the dust devil frequency together with the frequencies of weak, strong and other dust events (*Shao et al.*, 2013) for Australia from 1984 to 2012, where the category "other dust events" now only contains ww = 98 and W_1 or W_2 = 3. A clear seasonal dependence of dust devil occurrence can be recognized. This is related to stronger surface heating and convection in summer. Peak dust devil frequencies were typically between 0.1 and 0.3 %, but up to almost 0.6 % in 1991. The years 1990–1992 show extraordinary high dust devil frequencies, accompanied by relatively frequent thunderstorm and past weather dust reports. During the recent years, 2008 shows the highest dust devil occurrence together with exceptional low frequencies of both strong and other (thunderstorm, past weather) dust events. The occurrence frequency of weak dust events is also relatively low ($\approx$ 0.3 %) compared to e.g. 1.4 % in 2009. In 2009, the highest strong dust event frequency of 0.17 % was recorded, presumably leading to the large number of suspended and blowing dust (weak dust event) reports. The high dust devil frequency together with low dust storm occurrence in 2008 provides excellent conditions for an as-

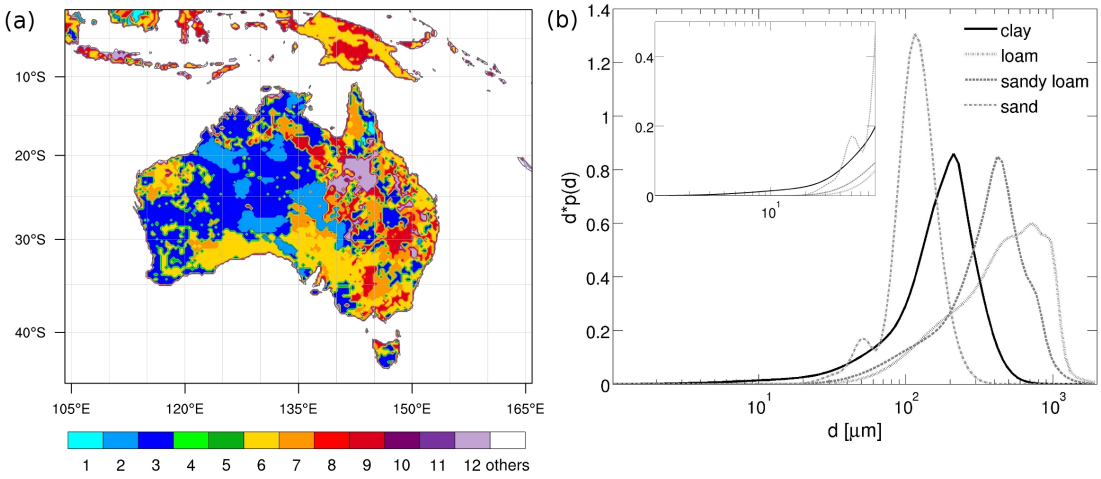

Fig. 6.2.: (a) Dominant soil types in the model domain based on the USGS soil texture classification. The twelve classes are: 1 sand, 2 loamy sand, 3 sandy loam, 4 silt loam, 5 silt, 6 loam, 7 sandy clay loam, 8 silty clay loam, 9 clay loam, 10 sandy clay, 11 silty clay, and 12 clay. (b) Minimally dispersed particle-size distributions based on the coefficients given in Table 6.1 for clay, loam, sandy loam, and sand. The insert shows the size-range 0-80 μm.

sessment of the significance of CTDE for the regional dust budget. With outlook on a comparison of the model results to e.g. dust concentration observations, we preferred a time period with a frequent occurrence of convective dust events and a small fraction of strong dust events. The different dust event types cannot be distinguished in the dust concentration measurements and thus the contribution of dust events other than CTDE should be as small as possible for a model-observations comparison. On this basis, the period 01 July 2007 00 UTC to 01 July 2008 00 UTC has been chosen as time period for the model simulations. The choice of a one-year analysis period allows for the investigation of seasonal CTDE development and gives the opportunity of a yearly budget estimate.

6.2. Model setup

Model input data crucial for dust emission calculation, such as vegetation fraction, dust source areas, and soil psd, were predefined for the region and time period chosen. Monthly averaged vegetation cover data were created as model input based on a MODIS-based vegetation fractional cover product developed by *Guerschman et al.* (2012) (`http://www.clw.csiro.au/publications/science/2012/SAF-MODIS-fractional-cover.pdf`). Monthly maps of potential dust source areas (*Butler et al.*, 2013) were implemented in the model, where a dust source is defined as area with $> 50\,\%$ bare soil (*Leys*, 1991) based on the fractional

	p_1			p_2			p_3			p_4		
	w	$\overline{\ln d}$	σ	w	$\overline{\ln d}$	σ	w	$\overline{\ln d}$	σ	w	$\overline{\ln d}$	σ
sand	0.03	3.62	0.28	0.28	4.99	0.30	0.05	3.93	0.14	0.64	4.72	0.24
loamy sand	0.50	6.07	0.40	0.20	4.33	0.40	0.22	5.28	0.35	0.08	6.64	0.22
sandy loam	0.02	6.66	0.10	0.05	6.07	0.12	0.32	5.18	0.75	0.60	6.07	0.41
silt loam	0.03	5.21	0.19	0.50	4.33	0.45	0.31	3.58	1.07	0.17	4.14	0.19
silt	0.03	5.21	0.19	0.50	4.33	0.45	0.31	3.58	1.07	0.17	4.14	0.19
loam	0.07	6.90	0.10	0.10	6.67	0.16	0.50	5.57	0.73	0.33	6.30	0.35
sandy clay loam	0.50	5.17	0.31	0.25	4.62	0.28	0.01	4.91	0.10	0.24	5.02	0.93
silty clay[1]	1.26	4.80	0.38	0.81	5.25	0.30	0.45	5.12	1.26	0.	0.	0.
clay loam	0.18	6.31	0.21	0.42	6.08	0.40	0.33	5.59	0.77	0.06	6.58	0.10
sandy clay[1]	0.31	4.14	0.17	0.96	3.95	1.78	1.03	4.31	0.43	0.	0.	0.
silty clay	0.27	4.92	0.20	0.06	4.58	0.16	0.14	3.90	0.81	0.53	4.53	0.49
clay	0.24	4.59	0.63	0.06	3.31	1.17	0.03	5.39	0.10	0.67	5.31	0.39

Tab. 6.1.: Coefficients for minimally-dispersed particle-size distributions as assigned to the 12 USGS soil texture classes. Each psd is composed of four lognormal distributions p_1, p_2, p_3, and p_4.

cover estimated by *Guerschman et al.* (2009). Psd data obtained from Australian soil samples are used in this study. The psd data were funded as part of the "Caring for Our Country – DustWatch Australia Wind erosion extent and severity mapping for Australia" project (*Butler et al.*, 2013). The psds were determined based on the minimally and fully dispersed techniques and were assigned to the 12 USGS (U.S. Geological Survey) soil texture classes (*Butler et al.*, 2013, and *Butler*, 2014, personal communication) (Figure 6.2a). In the model, each psd is composed of three or four lognormal distributions. The coefficients for each psd, namely weight w, mean value $\overline{\ln d}$, and standard deviation σ, are given in Table 6.1. No psd data for silt were available, therefore the same coefficients are used as for silt loam. The coefficients for silty clay and sandy clay were taken from *McDonald et al.* (1990). The weights of the latter were not normalized, therefore the psds are normalized after computation. Only the minimally dispersed psds are used in the CTDE scheme, as the disturbance on the soil is considered to be small due to the weak mean winds. Figure 6.2b shows the psds for the soil types clay, loam, sandy loam, and sand. It can be seen that the abundance of particles $< 20\,\mu$m is greatest for clay, leading to the largest modeled dust emission rates as detailed in Section 6.3.

[1] Coefficients from *McDonald et al.* (1990)

eddy viscosity	horizontal Smagorinsky first order closure (*Smagorinsky*, 1963; *Deardorff*, 1972)
boundary layer	Yonsei University scheme (*Hong et al.*, 2006)
microphysics	Purdue Lin scheme (*Lin et al.*, 1983; *Rutledge and Hobbs*, 1984; *Chen and Sun*, 2002)
longwave radiation	RRTM (*Mlawer et al.*, 1997)
shortwave radiation	Goddard shortwave scheme (*Chou and Suarez*, 1994)
surface layer	revised MM5 scheme (*Jimenez et al.*, 2012)
land-surface model	unified Noah (*Tewari et al.*, 2004)
cumulus physics	Grell 3D ensemble (*Grell*, 1993; *Grell and Devenyi*, 2002)
dust dry deposition	GOCART (*Ginoux et al.*, 2001)

Tab. 6.2.: WRF/Chem-Dust model settings chosen for the one-year simulation.

The CTDE scheme was coupled to the Weather Research and Forecasting (WRF) Model (*Skamarock et al.*, 2008) Version 3.51 with Chemistry (*Grell et al.*, 2005), herein referred to as WRF/Chem-Dust. The one-year period was modeled as consecutive 3.5-day model runs. Hereby we aimed to ensure a good reliability of the meteorological parameters with at the same time a well-developed WRF physics representation after model spin up and a relatively small number of model runs to save processing time between the simulations. Depending on the days in each month, the length of the last simulation of each month varies from 2.5 - 4.5 days. The consecutive runs were designed such that they have an overlap of 12 h used as model spin up time. The model initial and boundary conditions were obtained from the National Centers for Environmental Prediction (NCEP) Final Analysis (FNL) product at 1° horizontal resolution and the boundary conditions were updated every 6 hours. The initial dust concentrations for all model runs except for the first were obtained from the corresponding time step of the previous simulation. A 30 km horizontal resolution was used together with 39 vertical layers up to the 50 hPa level. A summary of the physics and dynamics parameterizations chosen in this study is given in Table 6.2. Dust emission and concentration output is given for four size bins: 0 - 2.5, 2.5 - 5, 5 - 10, and 10 - 20 μm.

6.3. Seasonal evolution and regional CTDE budget

Figure 6.3 shows the potential dust source regions (gray shading) (see Section 6.2) and monthly averaged values of 12 LST (local standard time) (UTC + 10 h) emission flux. Regions of the Interim Biographic Regionalisation for Australia (IBRA) Version 7 (*Commonwealth of Australia*, 2012), available from `http://www.environment.gov.au/topics/land/national-reserve-system/science-maps-and-data/australias-bioregions-ibra`, are overlaid as reference (for details see Figure 6.4). A clear seasonal dependence can be recognized due to the stronger surface heating in summer and accordingly more intensive convective turbulence. Dust emissions are mostly constrained to a few areas within the Mitchell Grass Downs (western Queensland) and central Australia (Finke and Stony Plains) in the winter months June and July. Few emissions occur in Pilbara (Western Australia). Emission regions spread during the other seasons and are widest and strongest during spring and summer. In general, noon-time emission magnitudes are a few tens $\mu g\,m^{-2}\,s^{-1}$ in most regions, but are found to be of the order of magnitude of $100\,\mu g\,m^{-2}\,s^{-1}$ in western Queensland. The largest emissions during the simulation year occurred in October 2007, associated with low average rainfall and vegetation cover as well as favorable weather conditions such as high pressure and temperature (compare Figure 6.6a); in particular at the Mitchell Grass Downs with emission fluxes of more than $200\,\mu g\,m^{-2}\,s^{-1}$. This region has clay-rich vertosols which foster large emissions due to their fine texture (Figure 6.2b). In clay-rich areas, crust formation and disturbance through e.g. agriculture are pivotal for dust-particle abundance. This is, however, not accounted for in the model (see Chapter 7.2). Regions with sandy loam (central Australia) and sandy clay loam (southeast Australia) soils also appear to promote dust emission (compare Figure 6.2a).

Emissions in the southern Channel Country and across New South Wales peak in January to March. The tendency for dust emissions to be large in spring for north-eastern Australia and in summer for south-eastern Australia is consistent with earlier studies on land erodibility (*Webb et al.*, 2009) and dust seasonality (*McTainsh et al.*, 1998), and is mostly related to rainfall influences on soil moisture and vegetation cover.

The monthly average dust load is shown in Figure 6.5. Due to the small emissions in July 2007 and June 2008, the atmospheric dust load is only few $mg\,m^{-2}$ during these months. However, the dust extends over most of Australia and is transported over the oceanic regions to the northwest (NW) and southeast (SE) of the continent. These two transport pathways persist for most months. This pattern is consistent with previous studies on Australian dust transport and has been first suggested by *Bowler* (1976). *McGowan*

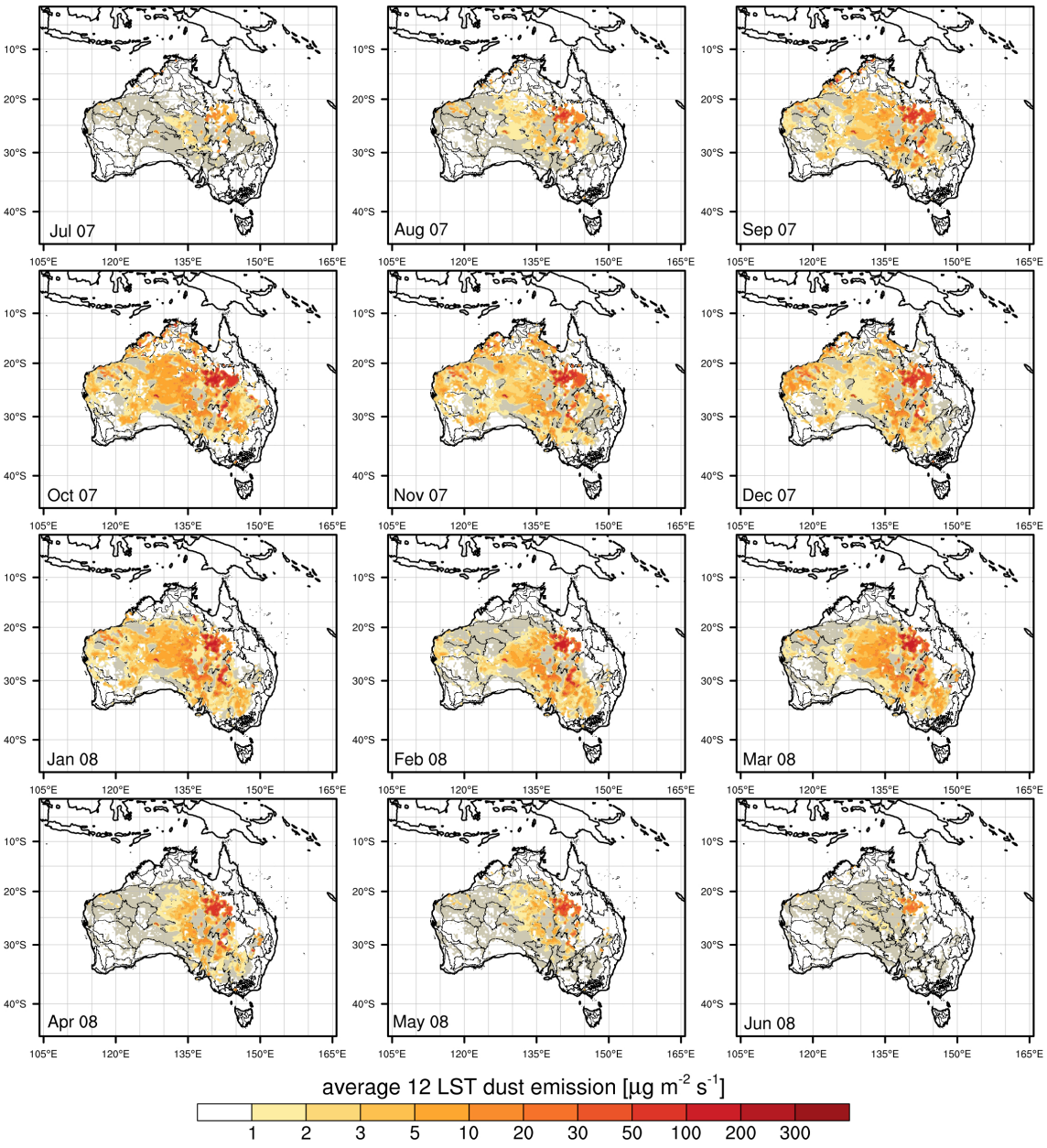

Fig. 6.3.: Monthly average of 12 LST (UTC + 10 h) dust emission flux [$\mu g\,m^{-2}\,s^{-1}$] of particles with sizes $d < 20\,\mu m$ together with potential dust sources defined as areas with a fraction of bare soil $> 50\,\%$ (gray shading).

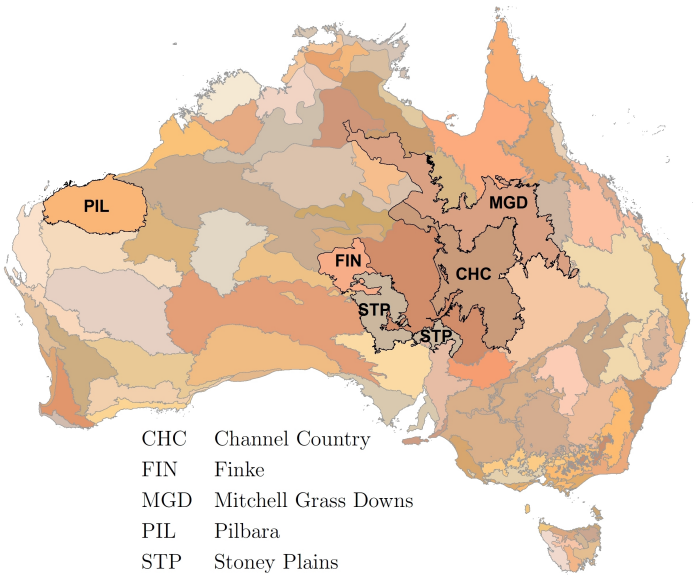

Fig. 6.4.: Interim Biographic Regionalisation for Australia (IBRA) Version 7 (*Commonwealth of Australia*, 2012). Only the names of the regions referred to in this Chapter are given. For more information see http://www.environment.gov.au/topics/land/national-reserve-system/science-maps-and-data/australias-bioregions-ibra.

and Clark (2008) identified similar dust transport pathways in a seasonal climatology of forward trajectories for dust originating in the central Lake Eyre basin. In our study, dust transport is found to be oriented to the northeast (NE) (Dec and Jan) in addition to the NW/SE corridor in the winter months and tends to align zonally in Feb. These results differ from those of *McGowan and Clark* (2008), because we considered areal dust sources instead of a point source and only one year instead of a climatological mean. The local synoptic situation is therefore decisive for dust transport in contrast to climatological flow patterns.

From September to March, the dust load is much larger over most of the continent (50 - 200 mg m^{-2}) than in the winter months, exceeding 500 mg m^{-2} in regions of persistent high emissions. Even over most oceanic regions in the simulation domain, dust loadings of more than 20 mg m^{-2} are predicted. The extent of the monthly averaged dust load does not necessarily represent the dust plume widths at particular dates. The atmospheric residence time of small dust particles is, however, known to be several days to several weeks (e.g. *Prospero*, 1999). This suggests that wide spread average dust loadings also denote wide extents of instantaneous dust loadings. The simulation results confirmed this (not shown) especially during daytime when emission is active. Dust concentration in the

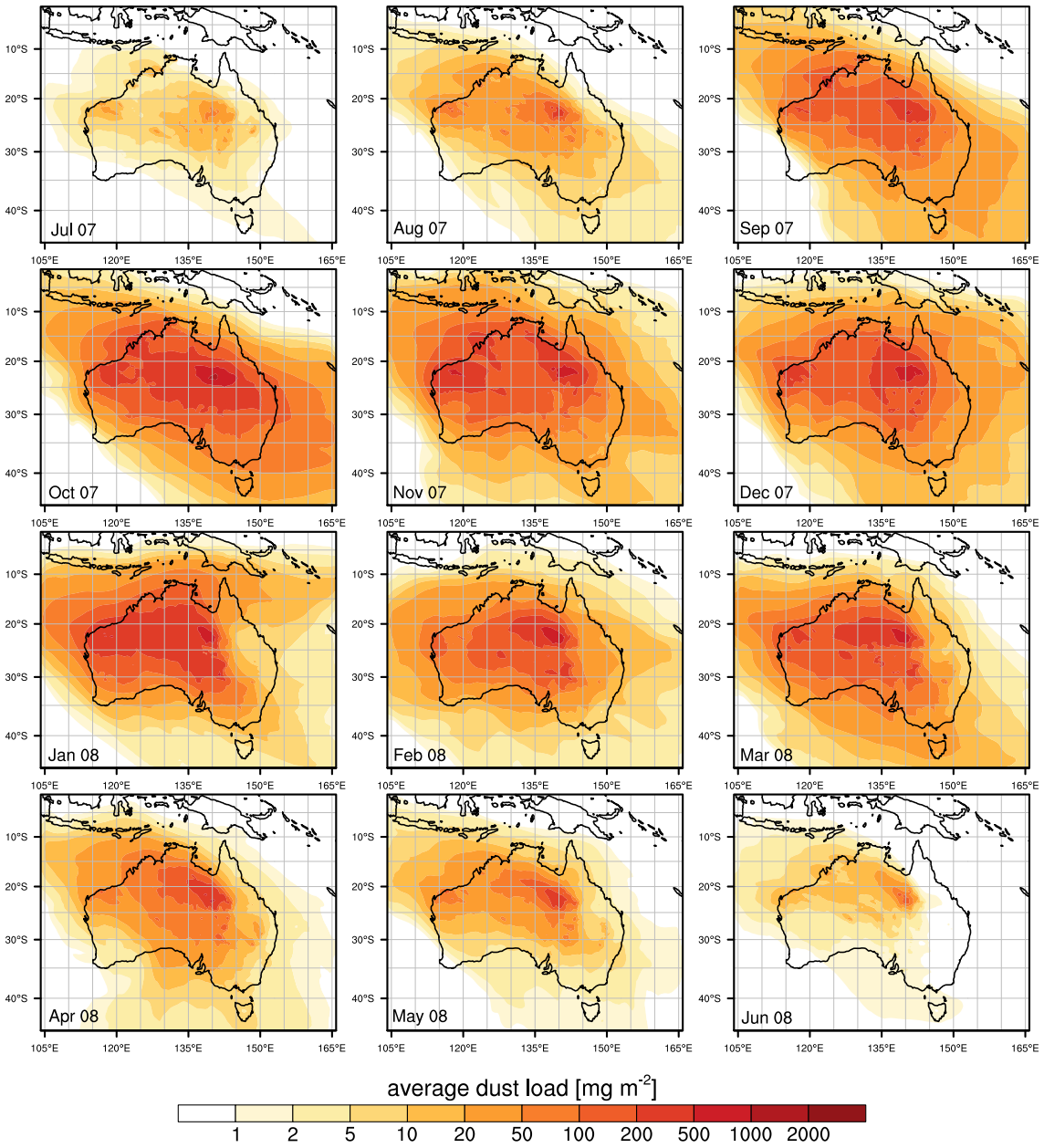

Fig. 6.5.: Monthly average dust load [mg m^{-2}] ($d < 20\,\mu$m) obtained from the one-year simulation.

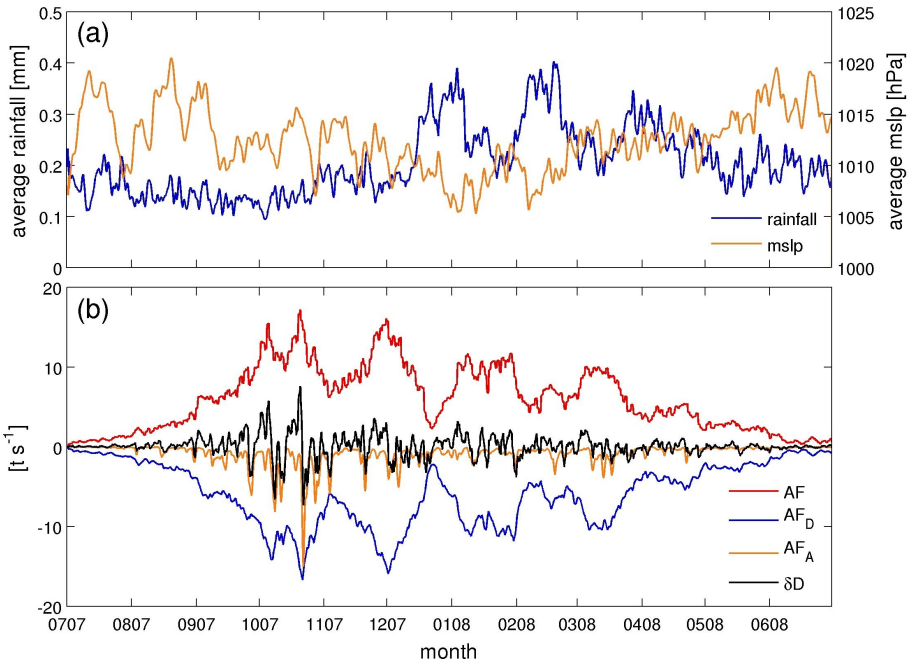

Fig. 6.6.: Daily running mean of (a) domain averaged hourly rainfall and mean-sea-level pressure (mslp) and (b) hourly domain integrated emission AF, deposition AF_D (dry deposition and gravitational settling), advection in u and v direction AF_A, and temporal change of dust load δD [$\mathrm{t\,s^{-1}}$].

lowest model layer is mostly of the order of magnitude 10 - 100 $\mu\mathrm{g\,m^{-3}}$ during daytime (not shown). It is smaller at non-dust source regions and at times of the order of 1000 $\mu\mathrm{g\,m^{-3}}$ close to and at the time of active dust emission, i.e. within the Mitchell Grass Downs and northern Channel Country.

Once airborne, well-developed convective turbulence can mix dust particles throughout the planetary boundary layer, favoring a long atmospheric residence time and long-range transport in the simulations. Dust is transported over most of the continent and wide oceanic regions, confirming our hypothesized generation of a background dust concentration.

A regional dust budget has been calculated from the model results according to Eq.(25) in *Klose and Shao* (2012):

$$\delta D = AF + AF_D + AF_A \tag{6.1}$$

where AF, AF_D, and AF_A are the domain integrated emission, total deposition, and advection through the lateral boundaries. δD is the change with time of domain integrated

dust load. The total deposition is calculated as sum of dry deposition and gravitational settling. Wet deposition is currently not included in the model, potentially leading to an overestimation of dust atmospheric residence time. Figure 6.6 shows daily running means of (a) domain averaged hourly rainfall and mean-sea-level pressure (mslp) and (b) the budget components given in Equation (6.1) computed from the hourly model output. As also seen from Figure 6.3, the strongest emissions occur in October and November/December with about $15\,\mathrm{t\,s^{-1}}$. Somewhat smaller emissions of about $10\,\mathrm{t\,s^{-1}}$ are found in January and March. Periods of large CTDE occur with low average rainfall and tend to coincide with high pressure, which can lead to stronger irradiation and better-developed convective turbulence. Advection is mostly small during the simulation period. In total, 188 t of dust were emitted by CTDE during the one-year period and 29 t were advected through the boundaries of the simulation domain. 184 t were deposited inside the study domain, 32 t of which were deposited to the ocean.

This study provides the first long-term quantitative estimate of CTDE on a regional scale, allowing for assessment of the significance of the process. *Shao et al.* (2011) summarized estimates of yearly global and regional dust emissions produced by modeling studies based on the saltation bombardment process. The estimates of yearly global emission range from 1019 (*Miller et al.*, 2004) to $3321\,\mathrm{Tg\,yr^{-1}}$ (*Takemura et al.*, 2000). It must be noted that the considered dust-particle size range differs between the studies, e.g. $d < 8\,\mu\mathrm{m}$ in *Miller et al.* (2004) and $d < 20\,\mu\mathrm{m}$ in *Takemura et al.* (2000), leading to naturally larger mass-fluxes for a broader size range. In this study, PM20 ($d < 20\,\mu\mathrm{m}$) dust emissions are considered. We therefore compare our results to the estimates of *Takemura et al.* (2000), $3321\,\mathrm{Tg\,yr^{-1}}$, *Tanaka and Chiba* (2006), $1877\,\mathrm{Tg\,yr^{-1}}$, and *Tegen et al.* (2002), $1100\,\mathrm{Tg\,yr^{-1}}$, who consider similar sizes. Relative to these studies, the Australian CTDE provided about 6, 10, and 17 %, respectively, compared to the annual global dust emissions and 7 - 15 % relative to the annual global dust dry deposition. The latter percentages refer to the results of *Takemura et al.* and *Tanaka and Chiba*. The post-calibrated dust emissions estimates of *Tegen et al.* were used for comparison here, therefore no corresponding dust deposition estimate can be given. The higher percentages for dry deposition compared to emission result from the lack of wet deposition in our model simulations, leading to a larger contribution of dry deposition.

For Australia, *Tanaka and Chiba* (2006) predicted annual dust emissions of $106\,\mathrm{Tg\,yr^{-1}}$, smaller than the value of $188\,\mathrm{Tg\,yr^{-1}}$ obtained in this study. This might have several reasons: (1) CTDE is overestimated in the present study due to potential overestimation of the model parameter α_{N0} and disuse of a comprehensive roughness correction; (2) Dust

emissions are underestimated by *Tanaka and Chiba* (2006). After comparing their modeled dust concentration to observations, *Tanaka and Chiba* state that "dust concentration at the stations in the southern hemisphere tend to be underestimated"; (3) The coarse resolution of the global model of *Tanaka and Chiba* (2006) of $1.8° \times 1.8°$ might not appropriately represent the local circulations; (4) Dust emissions during July 2007 - June 2008 might have been stronger than the average emissions during 1990 - 1995 calculated by *Tanaka and Chiba*. Assumption (4) is supported by mostly below-average rainfall within the most emissive areas during the period (*Bureau of Meteorology*, 2008, 2009). A more detailed discussion will be given in Section 7.2.

Unfortunately, we cannot state conclusively which of the above factors led to the differences in our estimates. In fact, no clear answer on the accuracy of the CTDE estimates can be obtained from the above comparison. A more detailed comparison with observations will be needed. It was demonstrated, however, that even if CTDE is overestimated by the model, its contribution to the regional and global dust budgets can be significant.

7 Conclusions

A new mechanism of direct aerodynamic dust emission was identified and is referred to as "Convective Turbulent Dust Emission" (CTDE). The process differs from the dust emission mechanisms of saltation bombardment and aggregates disintegration in that it is initiated by buoyancy driven large-eddy momentum fluxes. CTDE is thus a stochastic process. It is herein assumed that due to the stochastic nature of the inter-particle cohesive forces, a fraction of loose dust particles is always readily available for direct entrainment by the aerodynamic lifting forces.

A gap between the observation of dust events and their representation in numerical models was recognized (Chapter 1). Although frequently observed, no detailed process description or generally applicable parameterization scheme of CTDE existed for use in regional atmospheric models. To bridge this gap, we aimed to address five research objectives in the framework of this thesis:

1. Investigation and definition of the CTDE mechanism;
2. Development of a comprehensive CTDE parameterization scheme;
3. Evaluation of the CTDE scheme based on field observations;
4. Implementation of the scheme into a regional atmospheric model; and
5. Assessment of the CTDE relevance in the Earth system.

All five research aims were addressed in this study. The CTDE mechanism was investigated from theory, numerical experiments, and field observations. A CTDE parameterization

scheme was proposed and further developed based on new insights. The scheme was calibrated and tested against observations and was implemented into a regional atmospheric model to assess the relevance of CTDE in the Earth system. The following section summarizes the research outcomes, before the study is concluded with a final discussion and a research outlook.

7.1. Summary

In Chapter 2 (*Klose and Shao*, 2012), Objectives 1 - 4 were addressed. The characteristics of CTDE were specified and first developments of a comprehensive CTDE parameterization scheme were introduced. As it is induced by convective turbulence, CTDE is described as stochastic process. In the scheme, CTDE was obtained based on the balance of aerodynamic lifting and inter-particle cohesive forces. Both forces were represented as probability density functions (pdfs), thereby accounting for the stochastic nature of CTDE. The lifting force is based on instantaneous momentum flux and was estimated as joint pdf of the turbulent wind components with the parameters being obtained from Monin-Obukhov similarity theory. The inter-particle cohesive forces were described as log-normal distribution. The mean and variance of the distribution were based on empirical data. The scheme was implemented into the regional model WRF/Chem and was applied for the first time to a regional CTDE simulation. The model results were calibrated and tested against lidar data and a preliminary three-day budget estimate was provided. The typical magnitude of CTDE was found to be 1 - 10 $\mu g\,m^{-2}\,s^{-1}$, at times up to 50 $\mu g\,m^{-2}\,s^{-1}$.

Chapter 3 (*Klose and Shao*, 2013) focused on Objectives 1 and 2. The CTDE parameterization scheme was improved by accounting for particle settling and was coupled to the WRF-LES model. In LES, instantaneous momentum flux can be explicitly calculated and does not need to be parameterized. WRF-LES could therefore be used to further investigate the CTDE process. LES experiments were conducted for 15 different atmospheric stability and background wind conditions. We could demonstrate that large eddies can effectively transport localized momentum fluxes to the surface, strong enough to emit dust. CTDE was found to occur predominantly in large-eddy updraft convergence lines, at downdraft centers, and in the area of vortices. Statistics on instantaneous momentum flux and dust emission were calculated from the LES results, confirming the stochasticity of the process.

Various scheme improvements and the scheme calibration were presented in Chapter 4 (*Klose et al.*, 2014a), thereby handling Objectives 1 and 3. The scheme was improved in that (1) A new similarity theory for instantaneous momentum flux was developed based on the results of Chapter 3. In this approach, the pdf of instantaneous momentum flux is directly estimated from macroscopic atmospheric measures, i.e. friction velocity u_*, convective scaling velocity w_*, and Obukhov length L, which are available diagnostic quantities in most regional atmospheric models. This reduced the computing time considerably; (2) The parameterization of the inter-particle cohesive force was changed from empirical to semi-empirical by employing a theory-based formulation for the mean cohesive force; (3) The representation of particle-size distribution was modified. Instead of using the mass psd as typically obtained from soil-sample analysis and as applied in most dust emission schemes, area psd is now used. It is thereby accounted for the fact that surface shear stress acts on particle-area rather than on particle volume; (4) Through comparison with particle-size resolved dust flux observations, a size-dependence of the model parameter α_N was discovered and accounted for in the scheme; (5) Correction methods to account for moisture and roughness effects were proposed. The improved scheme was calibrated against field observations from China and Australia. The dust emission scheme was applied for 18 CTDE cases identified from the data and overall good agreements were found. Model weak points occurred (I) in the case of intermittent saltation, which is currently not represented in the model; and (II) if convective turbulence is not fully developed as the scheme is optimized for unstable conditions. Observation uncertainties my arise from (a) biased dust concentration measurements, e.g. when dust is present in the atmosphere before the CTDE period starts, and correspondingly biased dust flux estimates obtained with a flux-gradient method; and (b) spatial heterogeneity of dust concentration in the surroundings of the instrument. The roughness correction is preliminary and was not tested against data.

In Chapter 5 (*Li et al.*, 2014), the characteristics of CTDE were investigated from the perspective of field observations (Objective 1). CTDE typically occurred at daytime from spring to autumn, predominantly between 08:00 and 15:00 LST, when surface radiative heating is strongest. CTDE events lasted up to 8 hours but mostly < 3 hours. From the field observations, no relationship between CTDE dust flux and friction velocity u_*, but a positive correlation with w_*/u_* has been observed, the latter indicating the contribution of buoyancy generated turbulence relative to shear driven turbulence. The measurements confirmed that CTDE is typically $1\text{ - }10\,\mu\mathrm{g\,m^{-2}\,s^{-1}}$, but can reach a few tens at favorable conditions (compare Chapters 2 and 4). During the measurement period, CTDE occurred 1.9 times more frequently than SADE (saltation bombardment and aggregates disintegra-

tion dust emission), accumulating to a total emission of more than 80 % compared to that of SADE. The measurements were also used for calibration (Objective 3) of the model parameter α_N.

Objectives 4 and 5 were addressed in Chapter 6. For the first time, a long-term budget study on CTDE at regional scale was introduced. A one-year simulation of CTDE was conducted for Australia with the regional model WRF/Chem-Dust. A strong seasonality of CTDE was detected corresponding to weather conditions favorable to CTDE, such as low rainfall together with low vegetation cover as well as relatively high pressure and associated strong surface heating and high temperatures in summer. The largest emissions occurred in spring and early summer. 188 t of dust were emitted by CTDE during the study year in Australia, representing 6 - 17 % compared to the estimate of annual global emissions. Once emitted, the dust was mixed through the atmospheric boundary layer, generating a low but persistent background dust concentration. 32 t of CTDE dust were deposited to the ocean, covering a wide area around Australia. Though no accuracy assessment on the long-term quantitative CTDE estimate could be given yet, the large amounts of emitted dust, the long atmospheric residence time, and the corresponding long-range transport confirm the significance of the process.

We could demonstrate that we successfully developed a CTDE parameterization scheme that is generally applicable for modeling at different scales: site-based (Chapter 4, 5), on large-eddy scale (Chapter 3), and regional (Chapter 6). Global applications are also possible under the premise that the necessary input parameters, such as u_*, w_*, L, η, θ, as well as soil type, are provided. The presented model enabled us to assess the long-term CTDE contribution to the regional dust budget, underlining the relevance of the process.

7.2. Discussion and outlook

In this study, a detailed description of the process of "Convective Turbulent Dust Emission" was provided. The LES experiments (Chapter 3) have fundamentally contributed to our understanding of the process. The field observations (Chapter 5) demonstrated a correlation between dust emission and convective turbulence, supporting the theory presented in this study. The good agreement of the modeled to observed dust emission (Chapter 4) implies that the CTDE mechanism is captured by the parameterization scheme.

The CTDE magnitude has been found to be typically of the order 1 - 10 $\mu g\,m^{-2}\,s^{-1}$ and at times $\propto 100\,\mu g\,m^{-2}\,s^{-1}$. This magnitude is in good accordance with other stud-

ies. In their wind tunnel experiments, *Loosmore and Hunt* (2000) observed fluxes of $0\text{-}16\,\mu g\,m^{-2}\,s^{-1}$ in the absence of saltation. *Nickling and Gillies* (1993) report emission fluxes of similar magnitude for weak wind conditions (e.g. $u_* < 0.25\,m\,s^{-1}$) from their observations in Mali. In Australia, *Nickling et al.* (1999) measured slightly larger fluxes of $10\text{-}100\,\mu g\,m^{-2}\,s^{-1}$, which again are in good agreement with the JADE data and the results of our regional model.

The modeled surface dust concentrations during the study year were of the order of magnitude $10\text{-}100\,\mu g\,m^{-3}$, in good agreement with the background aerosol concentration observed by *Lu and Shao* (2001) at Birdsville, Australia, in February 1996. Even concentrations of few $100\,\mu g\,m^{-3}$ have been observed occasionally. So far, no comparison between the simulation results and observations for 2007/2008 was made. A well-established network of dust observations for Australia exists (DustWatch Australia, *Leys et al.*, 2008). PM10 dust concentration measurements as well as meteorological observations are available for 41 sites (`http://www.dustwatch.edu.au/`), providing an excellent basis for evaluation of the model results.

Global models predict annual global emissions of about $1000\text{-}3000\,Tg\,yr^{-1}$ for dust particles of size $d < 20\,\mu m$ (e.g. *Takemura et al.*, 2000; *Tanaka and Chiba*, 2006; *Tegen et al.*, 2002) and annual emissions for Australia of $106\,Tg\,yr^{-1}$ (*Tanaka and Chiba*, 2006). According to this, the Australian CTDE comprised 6 - 17 % compared to the global and 180 % relative to the Australian dust emission estimates during the study period July 2007 - June 2008. Other studies (e.g. *Luo et al.*, 2003; *Zender et al.*, 2003; *Miller et al.*, 2004) suggest Australian annual emissions in the range of $37\text{-}148\,Tg\,yr^{-1}$, but for smaller particle-size ranges. Still, the magnitudes are smaller than estimated in this study. Also, the CTDE percentage relative to the global estimate is large given that only Australian CTDE was considered. Potential reasons were suggested in Section 6.3 and will be detailed in the following.

- In our CTDE model, we only accounted for fractional vegetation cover. No comprehensive drag partition scheme was used. Although roughness elements can also enhance surface shear stress in their wake regions due to increased small-scale turbulence, the implementation of a more detailed roughness correction would likely lead to the reduction of CTDE on average.
- The global models typically have a coarse spatial and temporal resolution and depend on numerous simplifications. For example, *Luo et al.* (2003) use the dust emission scheme of *Marticorena and Bergametti* (1995) in which the dust emission flux is considered propor-

tional to horizontal saltation flux with the proportionality depending on soil clay content (see Chapter 1.1). Their assumption of a globally constant soil clay content of 20 % potentially resulted in biased dust emission estimates. The coarse spatial resolution mostly affects the atmospheric flow field as well as the representation of surface parameters. For example, the global model of *Tegen et al.* (2002) has a relatively high spatio-temporal resolution of the surface parameters (0.5° horizontal and 6 h temporal resolution), but a coarser horizontal resolution of the atmospheric flow field (1.25°). *Tegen et al.* found that the peak wind speeds were not captured in the flow field, supposedly leading to an underestimation of dust emission in their uncalibrated results. This effect might also apply for other global models despite their calibration for particular sites, especially as the modeled flow field is crucial for the dust concentration predictions used for calibration. In the model of *Tanaka and Chiba* (2006), the saltation bombardment dust emission model of *Shao et al.* (1996) was used. This scheme has been calibrated with wind tunnel data and was found by *Tanaka and Chiba* and in earlier studies (*Lu and Shao*, 2001) to produce Australian dust concentrations which are smaller than observed. For other regions, *Tanaka and Chiba* found different effects, e.g. a likely dust emission overestimation in the Sahara and underestimation in the Taklimakan desert. One possible reason was suggested by the authors to be the coarse model resolution (about 1.8° horizontal grid size in *Tanaka and Chiba*'s simulation) with associate insufficient representation of the local circulations and surface parameters. *Takemura et al.* (2000) used even larger grid sizes of about 5.6°. Although the model resolution we used (30 km) was also relatively coarse from the perspective of regional modeling, it is finer than in global models, leading to a better representation of the atmospheric flow.

- Additionally, the most emissive regions in Australia received mostly below average rainfall during July 2007 - June 2008 (*Bureau of Meteorology*, 2008, 2009), likely leading to increased dust fluxes compared to the climatological mean. This assumption is strengthened by increasing land erodibility at parts of the domain during the previous years (*Webb et al.*, 2009). The latter authors found the erodibility to be related to interannual/interdecadal climate variability. Its increase might thus have continued to the investigation period of our study as supported by the precipitation deficiency at that time (*Bureau of Meteorology*, 2008, 2009).

The newly developed CTDE scheme was shown to be generally applicable for local and regional applications. Only a few atmospheric quantities are required as input variables such as friction velocity u_*, convective scaling velocity w_*, and Obukhov length. Additionally, information on soil texture, vegetation cover, and soil moisture is needed.

The model was found to work well in general, but we met several research limitations during the development of the CTDE scheme:

1. Intermittent saltation, which can occur at friction velocities below the threshold (*Stout and Zobeck*, 1997), is not yet included in the model. In this study, CTDE is defined as direct aerodynamic entrainment. This means that intermittent saltation is strictly speaking not part of the CTDE process. However, the large surface shear stresses generated by convective turbulence will not only lift loose dust particles, but also the larger and heavier sand-sized grains and aggregates (compare Figure 1.1b and Figure 3 in Chapter 4). Accordingly, CTDE cannot be separated from emission due to intermittent saltation bombardment and the latter should be accounted for in the CTDE parameterization scheme.

2. The proposed moisture correction was only tested against a small soil moisture-range based on the Horqin and JADE data and the measurements were taken at different heights in the two datasets. This led to uncertainties in the determination of the model parameter α_N.

3. No test of the roughness correction could be performed. While the surface at the JADE site was almost bare, data at the Horqin site was insufficient for a reliable quantification of the rough surface. Therefore, we only accounted for the fractional cover in our simulations. The additional consideration of roughness distribution would potentially lead to a spatial and temporal redistribution of dust emissions and likely produce more reliable results. Data of fractional cover as well as spatial roughness element distribution are required for the development and testing of a comprehensive drag-partition parameterization.

4. Dust emission is limited by the supply of dust particles at the soil surface. However, no method to account for this effect is available so far. As the availability of free dust particles is an important assumption in our CTDE scheme, the results are sensitive to dust-particle abundance. Data supporting the development of a corresponding parameterization are needed.

The discussed limitations suggest priorities for future research. Studies on the modeling of intermittent saltation exist (e.g. *Dupont et al.*, 2013), but have not yet been included in dust emission parameterizations in regional models. An inclusion of intermittent saltation bombardment due to convective turbulence would lead to more robust CTDE estimates. Data which enable a thorough model-performance examination for moist and rough surfaces are required to overcome the lack of accurate moisture and roughness

effect representations in the model. Further, the investigation of surface crust and dust-particle abundance is crucial for reliable dust emission modeling, not only CTDE. This is of particular importance in areas with large clay contents such as the Mitchell Grass Downs in Australia. Although model limitations are recognized, we demonstrated that the new CTDE model has the capacity of CTDE prediction, suggesting its use for studies on various research questions, the most important of which are highlighted in the following.

Chapter 6 showed that a low but persistent dust concentration can be generated by CTDE. Due to the strong vertical mixing by atmospheric turbulence, the dust particles can have long atmospheric residence times. The long-lasting presence of dust aerosols will probably intensify the negative shortwave radiative forcing at the surface, arguable also yielding a negative feedback in CTDE. A study on the feedback between CTDE and radiation is planned.

The long atmospheric residence time of CTDE generated dust also allows for the transport to remote oceanic regions, which is of particular importance for atmospheric nutrient supply, e.g. iron. As noted in Chapter 1, *Cropp et al.* (2013) investigated the climatological link between dust and phytoplankton blooms in proximity to the Australian continent by comparing ocean receptivity with dust deposition. From their data, *Cropp et al.* found that ocean receptivity and dust deposition are often nonsynchronous. By comparison of *Cropp et al.*'s ocean receptivity and the CTDE dust loadings predicted in our study (Chapter 6), a much stronger oceanic biological response is expected due to wider regions being affected by dust transport and deposition. This underlines the need for a detailed numerical assessment of both episodic strong dust events and continuous CTDE events for investigation of the link between phytoplankton growth and dust-iron supply.

The development of a unified dust emission scheme by combination of SADE and CTDE parameterization schemes would facilitate investigations like the suggested and would arguable improve dust emission predictions. A unified dust emission scheme would be a perfect basis for evaluation of the magnitude and frequency characteristics of dust emission with regard to dust impacts on climate, biogeochemical cycles, dust transport pathways, and air quality. The necessary background and numerical tool were provided in this study.

A Supplementary material

Title: Large-eddy simulation of CTDE

Available at: http://dx.doi.org/10.5880/SFB806.5

Description:

The video shows results of a large-eddy simulation of CTDE based on (*Klose and Shao*, 2013, Exp10). Modeled dust concentration is visualized with a volume rendering approach. A particle-tracing is applied to illustrate a dust devil occurring in the simulation. Colors indicate the direction of particle movement. The visualization was done with DeskVOX, a visualization package developed at the Regional Computing Center Cologne. The video is licensed under CC BY 3.0 (`https://creativecommons.org/licenses/by/3.0/`).

Reference:

Klose, M., S. Zellmann, Y. Shao, and U. Lang (2014b), Large-eddy simulation of Convective Turbulent Dust Emission, doi: 10.5880/SFB806.5

References

Alfaro, S. C., and L. Gomes (2001), Modeling mineral aerosol production by wind erosion: Emission intensities and aerosol size distributions in source areas, *J. Geophys. Res.*, *106*(D16), 18,075–18,084.

Allen, C. J. T., R. Washington, and S. Engelstaedter (2013), Dust emission and transport mechanisms in the central sahara: Fennec ground-based observations from Bordj Badji Mokhtar, June 2011, *J. Geophys. Res.*, *118*, 6212–6232, doi: 10.1002/jgrd.50534.

Ansmann, A., M. Tesche, P. Knippertz, E. Bierwirth, D. Althausen, D. Müller, and O. Schulz (2009), Vertical profiling of convective dust plumes in southern morocco during SAMUM, *Tellus*, *61B*, 340–353, doi: 10.1111/j.1600-0889.2008.00384.x.

Bagnold, R. A. (1941), *The Physics of Blown Sand and Desert Dunes*, 265 pp., Methuen, London.

Balme, M., and R. Greeley (2006), Dust devils on Earth and Mars, *Rev. Geophys.*, *44*, RG3003, doi: 10.1029/2005RG000188.

Bangert, M., A. Nenes, B. Vogel, D. Barahona, V. A. Karydis, P. Kumar, C. Kottmeier, and U. Blahak (2012), Saharan dust event impacts on cloud formation and radiation over Western Europe, *Atmos. Chem. Phys.*, *12*, 4045–4063, doi: 0.5194/acp-12-4045-2012.

Boucher, O., D. Randall, P. Artaxo, C. Bretherton, G. Feingold, P. Forster, V.-M. Kerminen, Y. Kondo, H. Liao, U. Lohmann, P. Rasch, S. K. Satheesh, S. Sherwood, B. Stevens, and X. Y. Zhang (2013), Clouds and Aerosols, in *Climate Change 2013: The Physical Science Basis. Contribution of Working Group I to the Fifth Assessment Report of the Intergovernmental Panel on Climate Change*, edited by T. F. Stocker, D. Quin, G.-K. Plattner, M. Tignor, S. K. Allen, J. Boschung, A. Nauels, Y. Xia, V. Bex, and P. M. Midgley, Cambridge University Press, Cambridge, United Kingdom and New York, NY, USA.

Bowler, J. M. (1976), Aridity in Australia: age, origins and expression in aeolian landforms and sediments, *Earth-Sci. Rev.*, *12*, 179–310.

Boyd, P. W., D. S. Mackie, and K. A. Hunter (2010), Aerosol iron deposition to the surface ocean – Modes of iron supply and biological responses, *Marine Chemistry*, *120*, 128–143, doi: 10.1016/j.marchem.2009.01.008.

Bristow, C. S., K. A. Hudson-Edwards, and A. Chappell (2010), Fertilizing the Amazon and equatorial Atlantic with West African dust, *Geophys. Res. Lett.*, *37*, L14807, doi: 10.1029/2010GL043486.

Bureau of Meteorology (2008), Annual Climate Summary 2007, *Climate Analysis Section, National Climate Centre, Bureau of Meteorology*, Melbourne, April, 2008.

Bureau of Meteorology (2009), Annual Climate Summary 2008, *Climate Analysis Section, National Climate Centre, Bureau of Meteorology*, Melbourne, March 2009.

Butler, H., J. Leys, C. Strong, and G. McTainsh (2013), *Caring for our Country*, Wind erosion extent and severity maps for Australia, Final Report May 2013.

Cavazos, C., M. C. Todd, and K. Schepanski (2009), Numerical model simulation of the Saharan dust event of 6–11 March 2006 using the Regional Climate Model version 3 (RegCM3), *J. Geophys. Res.*, *114*(D12109), doi: 10.1029/2008JD011078.

Chen, S.-H., and W.-Y. Sun (2002), A one-dimensional time dependent cloud model, *J. Meteor. Soc. Japan*, *80*, 99–118.

Chkhetiani, O. G., E. B. Gledzer, M. S. Artamonova, and M. A. Iordanskii (2012), Dust resuspension under weak wind conditions: direct observations and model, *Atmos. Chem. Phys.*, *12*, 5147–5162, doi: 10.5194/acp-12-5147-2012.

Chou, M.-D., and M. J. Suarez (1994), An efficient thermal infrared radiation parameterization for use in general circulation model, *NASA Tech. Memo. 104606*, *3*, 85pp.

Claquin, T., M. Schulz, and Y. J. Balkanski (1999), Modeling the mineralogy of atmospheric dust sources, *J. Geophys. Res.*, *104*(D18), 22,243–22,256.

Commonwealth of Australia (2012), Interim Biogeographic Regionalisation for Australia (IBRA), Version 7, Available from `http://www.environment.gov.au/topics/land/national-reserve-system/science-maps-and-data/australias-bioregions-ibra`, IBRA version 7 was developed through co-operative efforts of the Australian Government Department of Sustainability, Environment, Water, Population and Communities and State/Territory land management agencies.

Cropp, R. A., A. J. Gabric, M. Levasseur, G. H. McTainsh, A. Bowie, C. S. Hassler, C. S. Law, H. McGowan, N. Tindale, and R. V. Rossel (2013), The likelihood of observing dust-stimulated

phytoplankton growth in waters proximal to the australian continent, *Journal of Marine Systems*, *117 – 118*, 43 – 52, doi: http://dx.doi.org/10.1016/j.jmarsys.2013.02.013.

Deardorff, J. W. (1972), Numerical investigation of neutral and unstable planetary boundary layers, *J. Atmos. Sci.*, *29*, 91 – 115, doi: 10.1175/1520-0469(1972)029⟨0091:NIONAU⟩2.0.CO;2.

DeMott, P. J., K. Sassen, M. R. Poellot, D. Baumgardner, D. C. Rogers, S. D. Brooks, A. J. Prenni, and S. M. Kreidenweis (2003), African dust aerosols as atmospheric ice nuclei, *GRL*, *30*(14).

Derbyshire, E. (2007), Natural minerogenic dust and human health, *AMBIO*, *36*(1), 73–77, doi: 10.1579/0044-7447(2007)36[73:NMDAHH]2.0.CO;2.

Descamps, I., J.-L. Harion, and B. Baudoin (2005), Taking-off model of particles with a wide size distribution, *Chemical Engineering and Processing*, *44*, 159–166, doi: 10.1016/j.geomorph.2003.09.004.

Dupont, S., G. Bergametti, B. Marticorena, and S. Simoëns (2013), Modeling saltation intermittency, *J. Geophys. Res. Atmos.*, *118*, 7109–7128, doi: 10.1002/jgrd.50528.

Field, P. R., O. Möhler, P. Connolly, M. Krämer, R. Cotton, A. J. Heymsfield, H. Saathoff, and M. Schnaiter (2006), Some ice nucleation characteristics of Asian and Saharan desert, *ACP*, *6*, 2991–3006.

Formenti, P., S. Caquineau, K. Desboeufs, A. Klaver, S. Chevaillier, E. Journet, and J. L. Rajot (2014), Mapping the physico-chemical properties of mineral dust in western africa: mineralogical composition, *Atmos. Chem. Phys. Discuss.*, *14*, 10,241 – 10,310, doi: 10.5194/acpd-14-10241-2014.

Fung, I. Y., S. K. Meyn, I. Tegen, S. C. Doney, J. G. John, and J. K. B. Bishop (2000), Iron supply and demand in the upper ocean, *Global Biogeochem. Cycles*, *14*(1), 281–295, doi: 10.1029/1999GB900059.

Garrison, V. H., E. A. Shinn, W. T. Foreman, D. W. Griffin, C. W. Holmes, C. A. Kellogg, M. S. Majewski, L. L. Richardson, K. B. Ritchie, and G. W. Smith (2003), African and Asian dust: from desert soils to coral reefs, *BioScience*, *53*(5), 469–480, doi: 10.1641/0006-3568(2003)053[0469:AAADFD]2.0.CO;2.

Gillette, D. A. (1977), Fine particulate emissions due to wind erosion, *Trans. Am. Soc. Agricultural Engrs.*, *20*, 890–897.

Gillette, D. A., and R. Passi (1988), Modeling dust emission caused by wind erosion, *J. Geophys. Res.*, *93*(D11), 14,233–14,242, doi: 10.1029/JD093iD11p14233.

Ginoux, P., M. Chin, I. Tegen, J. M. Prospero, B. Holben, O. Dubovik, and S.-J. Lin (2001), Sources and distributions of dust aerosols simulated with the GOCART model, *J. Geophys.*

Res., *106*(D17), 20,255–20,273.

Gledzer, E. B., I. G. Granberg, and O. G. Chkhetiani (2009), Convective aerosol fluxes near the ground surface, *Doklady Earth Science*, *426*(4), 652–657, doi: 10.1134/S1028334X09040321.

Grell, G. A. (1993), Prognostic evaluation of assumptions used by cumulus parameterizations, *Mon. Wea. Rev.*, *121*, 764–787.

Grell, G. A., and D. Devenyi (2002), A generalized approach to parameterizing convection combining ensemble and data assimilation techniques, *Geophys. Res. Lett.*, *29*(14), doi: 10.1029/2002GL015311.

Grell, G. A., S. E. Peckham, R. Schmitz, S. A. McKeen, G. Frost, W. C. Skamarock, and B. Eder (2005), Fully coupled "online" chemistry within the WRF model, *Atmos. Environ.*, *39*, 6957–6975, doi: 10.1016/j.atmosenv.2005.04.027.

Griffin, D. W. (2007), Atmospheric movement of microorganisms in clouds of desert dust and implications for human health, *Clin. Microbiol. Rev.*, *20*(3), 459–477, doi: 10.1128/CMR.00039-06.

Guerschman, J. P., M. J. Hill, L. J. Renzullo, D. J. Barrett, A. S. Marks, and E. J. Botha (2009), Estimating fractional cover of photosynthetic vegetation, non-photosynthetic vegetation and bare soil in the australian tropical savanna region upscaling the EO-1 Hyperion and MODIS sensors, *Remote Sensing of Environment*, *113*(5), 928–945, doi: 10.1016/j.rse.2009.01.006.

Guerschman, J. P., M. Oyarzabal, T. J. Malthus, T. M. McVicar, G. Byrne, L. A. Randall, and J. B. Stewart (2012), Evaluation of the modis-based vegetation fractional cover product, *CSIRO Land and Water Science Report*, Canberra, April 2012.

Heinold, B., I. Tegen, S. Bauer, and M. Wendisch (2011), Regional modelling of Saharan dust and biomass-burning smoke: Part 2: Direct radiative forcing and atmospheric dynamic response, *Tellus*, *4*(63B), 800–813, doi: 10.1111/j.1600-0889.2011.00574.

Hong, S.-Y., Y. Noh, and J. Dudhia (2006), A new vertical diffusion package with an explicit treatment of entrainment processes, *Mon. Wea. Rev.*, *134*, 2318–2341.

Hoose, C., U. Lohmann, R. Erdin, and I. Tegen (2008), The global influence of dust mineralogical composition on heteogeneous ice nucleation in mixed-phase clouds, *Environ. Res. Lett.*, *3*(2), 025,003, doi: doi:10.1088/1748-9326/3/2/025003.

Ishizuka, M., M. Mikami, J. F. Leys, Y. Shao, Y. Yamada, and S. Heidenreich (2014), Power law relation between size-resolved vertical dust flux and friction velocity measured in a fallow wheat field, *Aeolian Research*, *12*, 87–99, doi: 10.1016/j.aeolia.2013.11.002.

Isono, K. (1955), On ice-crystal nuclei and other substances found in snow crystals, *J. Meteor.*, *12*, 456–462, doi: 10.1016/j.aeolia.2013.11.002.

Ito, J., H. Niino, and M. Nakanishi (2010), Large eddy simulation on dust suspension in a convective mixed layer, *SOLA*, *6*, 133–136, doi: 10.2151/sola.2010-034133.

Jickells, T. D., Z. S. An, K. K. Andersen, A. R. Baker, G. Bergametti, N. Brooks, J. J. Cao, P. W. Boyd, R. A. .Duce, K. A. Hunter, H. Kawahata, N. Kubilay, J. laRoche, P. S. Liss, N. Mahowald, J. M. Prospero, A. J. Ridgwell, I. Tegen, and R. Torres (2005), Global iron connections between desert dust, ocean biogeochemistry, and climate, *Science*, *308*, 67–71, doi: 10.1126/science.1105959.

Jimenez, P. A., J. Dudhia, J. F. Gonzales-Rouco, J. Navarro, J. P. Montavez, and E. Garcia-Bustamante (2012), A revised scheme for the WRF surface layer formulation, *Mon. Wea. Rev.*, *140*, 898–918.

Kandler, K., L. Schütz, C. Deutscher, M. Ebert, H. Hofmann, S. Jäckel, R. Jaenicke, P. Knippertz, K. Lieke, A. Massling, A. Petzold, A. Schladitz, B. Weinzierl, A. Wiedensohler, S. Zorn, and S. Weinbruch (2009), Size distribution, mass concentration, chemical and mineralogical composition and derived optical parameters of the boundary layer aerosol at Tinfou, Morocco, during SAMUM 2006, *Tellus*, *61B*, 32–50, doi: 10.1111/j.1600-0889.2008.00385.x.

Karydis, V. A., P. Kumar, D. Barahona, I. N. Sokolik, and A. Nenes (2011), On the effect of dust particles on global cloud condensation nuclei and cloud droplet number, *J. Geophys. Res.*, *116*, D23204, doi: 10.1029/2011JD016283.

Kellogg, C. A., and D. W. Griffin (2006), Aerobiology and the global transport of desert dust, *Trends in Ecology and Evolution*, *21*(11), 638–644, doi: 10.1016/j.tree.2006.07.004.

Klose, M., and Y. Shao (2012), Stochastic parameterization of dust emission and application to convective atmospheric conditions, *Atmos. Chem. Phys.*, *12*(12), 7309–7320, doi: 10.5194/acp-12-7309-2012.

Klose, M., and Y. Shao (2013), Large-eddy simulation of turbulent dust emission, *Aeolian Research*, *8*, 49–58, doi: 10.1016/j.aeolia.2012.10.010.

Klose, M., Y. Shao, M. K. Karremann, and A. H. Fink (2010), Sahel dust zone and synoptic background, *Geophys. Res. Lett.*, *37*, L09802, doi: 10.1029/2010GL042816.

Klose, M., Y. Shao, X. L. Li, H. S. Zhang, M. Ishizuka, M. Mikami, and J. F. Leys (2014a), Further development of a parameterization for convective turbulent dust emission and evaluation based on field observations, *J. Geophys. Res. Atmos.*, *119*, 10,441–10,457, doi: 10.1002/2014JD021688.

Klose, M., S. Zellmann, Y. Shao, and U. Lang (2014b), Large-eddy simulation of Convective Turbulent Dust Emission, doi: 10.5880/SFB806.5.

Koch, J., and N. O. Renno (2005), The role of convective plumes and vortices on the global aerosol budget, *Geophys. Res. Lett.*, *32*, L18806, doi: 10.1029/2005GL023420.

Kok, J. F. (2011), A scaling theory for the size distribution of emitted dust aerosols suggests climate models underestimate the size of the global dust cycle, *Proc. Natl. Acad. Sci. USA*, D17204, doi: 10.1073/pnas.1014798108.

Kok, J. F., N. M. Mahowald, S. Albani, G. Fratini, J. A. Gillies, M. Ishizuka, J. F. Leys, M. Mikami, M.-S. Park, S.-U. Park, R. S. van Pelt, D. S. Ward, and T. M. Zobeck (2014), An improved dust emission model with insights into the global dust cycle's climate sensitivity, *Atmos. Chem. Phys. Discuss.*, doi: 10.5194/acpd-14-6361-2014.

Kumar, P., I. N. Sokolik, and A. Nenes (2011), Measurements of cloud condensation nuclei activity and droplet activation kinetics of fresh unprocessed regional dust samples and mineral, *Atmos. Chem. Phys.*, *11*, 3527–3541.

Leys, J., G. McTainsh, C. Strong, S. Heidenreich, and K. Biesaga (2008), DustWatch: using community networks to improve wind erosion monitoring in Australia, *Earth Surf. Proc. Landforms*, *33*, 1912–1926.

Leys, J. F. (1991), Towards a better model of the effect of prostate vegetation cover on wind erosion, *Vegetatio*, *91*, 48–58.

Li, X. L., M. Klose, Y. Shao, and H. S. Zhang (2014), Convective Turbulent Dust Emission (CTDE) observed over Horqin Sandy Land area and validation of a CTDE scheme, *J. Geophys. Res. Atmos.*, *119*, 9980–9992, doi: 10.1002/2014JD021572.

Lin, Y.-L., R. D. Farley, and H. D. Orville (1983), Bulk parameterization of the snow field in a cloud model, *J. Climate Appl. Meteor.*, *22*, 1065–1092.

Loosmore, G. A., and J. R. Hunt (2000), Dust resuspension without saltation, *J. Geophys. Res.*, *105*(D16), 20,663–20,671, doi: 10.1029/2000JD900271.

Lu, H., and Y. Shao (2001), Toward quantitative prediction of dust storms: an integrated wind erosion modelling system and its applications, *Env. Modelling & Software*, *16*, 233–249.

Luo, C., N. M. Mahowald, and J. del Corral (2003), Sensitivity study of meteorological parameters on mineral aerosol mobilization, transport and distribution, *J. Geophys. Res.*, *108*(4447).

Mahowald, N. M., A. R. Baker, G. Bergametti, N. Brooks, R. A. Duce, T. D. Jickells, N. Kubilay, J. M. Prospero, and I. Tegen (2005), Atmospheric global dust cycle and iron inputs to the ocean, *Global Biogeochem. Cycles*, *19*(GB4025), doi: 0.1029/2004GB00240.

Marticorena, B., and G. Bergametti (1995), Modeling the atmospheric dust cycle: 1. Design of a soil-derived dust emission scheme, *J. Geophys. Res.*, *100*(D8), 16,415–16,430.

Martin, J. H. (1990), Glacial-interglacial CO_2 change: The iron hypothesis, *Paleoceanography*, *5*(1), 1–13.

Martin, J. H., and S. E. Fitzwater (1988), Iron deficiency limits phytoplankton growth in the

north-east Pacific subarctic, *Nature*, *331*(6153), 341–343.

Martin, J. H., K. H. Coale, K. S. Johnson, S. E. Fitzwater, R. M. Gordon, S. J. Tanner, C. N. Hunter, V. A. Elrod, J. L. Nowicki, T. L. Coley, R. T. Barber, S. Lindley, A. J. Watson, J. V. Scoy, C. S. Law, M. I. Liddlcoat, R. Ling, T. Stanton, J. Stockel, C. Collins, A. Anderson, R. Bidigare, M. Ondrusek, M. Latasa, F. J. Millero, K. Lee, W. Yao, J. Z. Zhang, G. Friederich, C. Sakamoto, F. Chavez, K. Buck, Z. Kolber, R. Greene, P. Falkowski, S. W. Chisholm, F. Hoge, R. Swift, J. Yungek, S. Turner, P. Nightingale, A. Hatton, P. Liss, and N. W. Tindale (1994), Testing the iron hypothesis in ecosystems of the equatorial pacific ocean, *Nature*, *371*, 123—-129.

McDonald, R., R. Isbell, J. Speight, J. Walker, and M. Hopkins (1990), *Australian soil and land survey field handbook*, 2nd edn. ed., Inkata Press, Melbourne.

McGowan, H., and A. Clark (2008), Identification of dust transport pathways from Lake Eyre, Australia using Hysplit, *Atmos. Environ.*, *42*, 6915–6925.

McTainsh, G. H., A. W. Lynch, and E. K. Tews (1998), Climatic controls upon dust storm occurrence in eastern Australia, *Journal of Arid Environments*, *39*, 457–466.

McTainsh, G. H., Y.-C. Chan, H. McGowan, J. Leys, and K. Tews (2005), The 23rd October 2002 dust storm in eastern Australia: characteristics and meteorological conditions, *Atmos. Environ.*, *39*, 1227–1236.

Miller, R., I. Tegen, and Z. Perlwitz (2004), Surface radiative forcing by soil dust aerosols and the hydrologic cycle, *J. Geophys. Res.*, *109*(D04203), doi: 10.1029/2003JD004085.

Mlawer, E. J., S. J. Taubmann, P. D. Brown, M. J. Iacono, and S. A. Clough (1997), Radiative transfer for inhomogeneous atmospheres: RRTM, a validated correlated-k model for the longwave, *J. Geophys. Res.*, *102*(D14), 16,663–16,682.

Nickling, W. G., and J. A. Gillies (1993), Dust emission and transport in Mali, West Africa, *Sedimentology*, *40*, 859–868.

Nickling, W. G., G. H. McTainsh, and J. F. Leys (1999), Dust emission from the Channel Country of western Queensland, Australia, *Z. Geomorph. N.F.*, *116*, 1–17.

Nickovic, S., A. Vukovic, M. Vujadinovic, V. Djurdjevic, and G. Pejanovic (2012), Technical Note: High-resolution mineralogical database of dust-productive soils for atmospheric dust modeling, *Atmos. Chem. Phys.*, *12*, 845–855, doi: 10.5194/acp-12-845-2012.

Oke, A. M. C., N. J. Tapper, and D. Dunkerley (2007), Willy-willies in the australian landscape: The role of key meteorological variables and surface conditions in defining frequency and spatial characteristics, *J. Arid Environ.*, *71*, 201–215, doi: 10.1016/j.jaridenv.2007.03.008.

Okin, G. S., N. Mahowald, O. A. Chadwick, and P. Artaxo (2004), Impact of desert dust on the biogeochemistry of phosphorus in terrestrial ecosystems, *Global Biogeochem. Cycles*, *18*,

GB2005, doi: 10.1029/2003GB002145.

Prospero, J. M. (1999), Long-range transport of mineral dust in the global atmosphere: Impact of African dust on the environment of the southeastern United States, *Proc. Natl. Acad. Sci. USA*, *96*, 3396–3403.

Renno, N. O., V. J. Abreu, J. Koch, P. H. Smith, O. K. Hartogensis, H. A. R. D. Bruin, D. Burose, G. T. Delory, W. M. Farrell, C. J. Watts, J. Garatuza, M. Parker, and A. Carswell (2004), MATADOR 2002: A pilot field experiment on convective plumes and dust devils, *J. Geophys. Res.*, *109*, E07001, doi: 10.1029/2003JE002219.

Rosenfeld, D., Y. Rudich, and R. Lahav (2001), Desert dust suppressing precipitation: A possible desertification feedback loop, *Proc. Natl. Acad. Sci. USA*, *98*(11), 5975–5980, doi: 10.1073/pnas.101122798.

Rosenfeld, D., S. Sherwood, R. Wood, and L. Donner (2014), Climate effects of aerosol-cloud interactions, *Science*, *343*, 379–380, doi: 10.1126/science.1247490.

Rutledge, S. A., and P. V. Hobbs (1984), The Mesoscale and Microscale Structure and Organization of Coulds and Precipitation in Midlatutude Cyclones. XII: A Diagnostic Modeling Study of Precipitation Development in Narrow Cold-Frontal Rainbands, *J. Atmos. Sci.*, *41*(20), 2949–2972.

Sassen, K. (2005), Dusty ice clouds over Alaska, *Nature*, *434*, 456.

Shao, Y. (2001), A model for mineral dust emission, *J. Geophys. Res.*, *106*(D17), 20,239–20,254.

Shao, Y. (2004), Simplification of a dust emission scheme and comparison with data, *J. Geophys. Res.*, *109*, D10202, doi: 10.1029/2003JD004372.

Shao, Y. (2008), *Physics and Modelling of Wind Erosion*, 2 ed., 452 pp., Springer–Verlag, Berlin.

Shao, Y., M. R. Raupach, and P. A. Findlater (1993), The effect of saltation bombardment on the entrainment of dust by wind, *J. Geophys. Res.*, *98*, 12,719–12,726.

Shao, Y., M. R. Raupach, and J. F. Leys (1996), A model for predicting aeolian sand drift and dust entrainment on scales from paddock to region, *Aust. J. Soil Res.*, *34*, 309–342.

Shao, Y., A. H. Fink, and M. Klose (2010), Numerical simulation of a continental-scale Saharan dust event, *J. Geophys. Res.*, *115*, D13205, doi: 10.1029/2009JD012678.

Shao, Y., K.-H. Wyrwoll, A. Chappell, J. Huang, Z. Lin, G. H. McTainsh, M. Mikami, T. Y. Tanaka, X. Wang, and S. Yoon (2011), Dust cycle: An emerging core theme in Earth system science, *Aeolian Research*, *2*, 181–204, doi: 10.1016/j.aeolia.2011.02.001.

Shao, Y., M. Klose, and K.-H. Wyrwoll (2013), Recent global dust trend and connections to climate forcing, *J. Geophys. Res. Atmos.*, *118*, 1–12, doi: 10.1002/jgrd.50836.

Shinn, E. A., G. W. Smith, J. M. Prospero, P. Betzer, M. L. Hayes, V. Garrison, and R. T. Barber (2000), African dust and the demise of Carribbean coral reefs, *Geophys. Res. Lett.*, *27*(19), 3029–3032, doi: 10.1029/2000GL011599.

Sinclair, P. C. (1969), General characteristics of dust devils, *J. Appl. Meteor.*, *8*, 32–45, doi: 10.1175/1520-0450(1969)008⟨0032:GCODD⟩2.0.CO;2.

Skamarock, W. C., J. B. Klemp, J. Dudhia, D. O. Gill, D. M. Barker, M. G. Duda, X.-Y. Huang, W. Wang, and J. G. Powers (2008), A Description of the Advanced Research WRF Version 3, *NCAR Technical Note*, `http://www.mmm.ucar.edu/wrf/users/docs/arw_v3.pdf`.

Smagorinsky, J. (1963), General circulation experiments with the primitive equations; I. Basic experiment, *Mon. Wea. Rev.*, *91*(3), 99–164.

Sokolik, I. N., and O. B. Toon (1996), Direct radiative forcing by anthropogenic airborne mineral aerosols, *Nature*, *381*, 681–683.

Sokolik, I. N., and O. B. Toon (1999), Incorporation of mineralogical composition into models of the radiative properties of mineral aerosol from UV to IR wavelength, *J. Geophys. Res.*, *104*(D8), 9423–9444.

Stout, J. E., and T. M. Zobeck (1997), Intermittent saltation, *Sedimentology*, *44*, 959–970.

Takemura, T., H. Okamoto, Y. Maruyama, Y. Namaguti, A. Higurashi, and T. Nakajima (2000), Global three-dimensional simulation of aerosol optical thickness distribution of various origins, *J. Geophys. Res.*, *105*(D14), 17,853–17,873.

Tanaka, T. Y., and M. Chiba (2006), A numerical study of the contributions of dust source regions to the global dust budget, *Global Planet. Change*, *52*, 88–104.

Tegen, I., and A. A. Lacis (1996), Modeling of particle size distribution and its influence on the radiative properties of mineral dust, *J. Geophys. Res.*, *101*(D14), 19,237–19,244.

Tegen, I., S. P. Harrison, K. Kohfeld, I. C. Prentice, M. Coe, and M. Heimann (2002), Impact of vegetation and preferential source areas on global dust aerosol: Results from a model study, *J. Geophys. Res.*, *107*(4576).

Tegen, I., E. Bierwirth, B. Heinold, J. Helmert, and M. Wendisch (2010), Effect of measured surface albedo on modeled saharan dust solar radiative forcing, *J. Geophys. Res.*, *115*(D24312).

Tewari, M., F. Chen, W. Wang, J. Dudhia, M. A. LeMone, K. Mitchell, M. Ek, G. Gayno, J. Wegiel, and R. H. Cuenca (2004), Implementation and verification of the unified NOAH land surface model in the WRF model, *20th conference on weather analysis and forecasting/16th conference on numerical weather prediction*, pp. 10–15.

UK Meteorological Office (2013), Met Office Integrated Data Archive System (MIDAS) Land and Marine Surface Stations Data (1853–current), Available from `http://badc.nerc.ac.uk/view/`

`badc.nerc.ac.uk__ATOM__dataent_ukmo-midas`.

Webb, N. P., H. A. McGowan, S. R. Phinn, G. H. McTainsh, and J. F. Leys (2009), Simulation of the spatiotemporal aspects of land erodibility in the northeast Lake Eyre Basin, Australia, 1980-2006, *J. Geophys. Res.*, *114*(F01013), doi: 10.1002/2008JF001097.

Zender, C. S., H. Bian, and D. Newman (2003), Mineral dust entrainment and deposition (DEAD) model: Description and 1990s dust climatology, *J. Geophys. Res.*, *108*(D14).

Zimon, A. D. (1982), *Adhesion of dust and powder*, 438 pp., Consultants Bureau, New York.

List of abbreviations

CTDE	Convective Turbulent Dust Emission
HNLC	high-nitrate-low-chlorophyll
IBRA	Interim Biographic Regionalisation for Australia
IPCC AR5	International Panel on Climate Change Fifth Assessment Report
JADE	Japan-Australian Dust Experiment
LES	large-eddy simulation
LST	local standard time
MOST	Monin-Obukhov Similarity Theory
mslp	mean-sea-level pressure
PBL	planetary boundary layer
pdf	probability density function
PM10, PM20	particulate matter with diameter $d < 10\,\mu$m and $d < 20\,\mu$m
psd	particle-size distribution
RH	relative humidity
SADE	emission due to saltation bombardment and aggregates disintegration
TOA	top of the atmosphere
USGS	U.S. Geological Survey
UTC	universal time code
WRF	Weather Research and Forecasting

List of symbols

AF, AF_D, AF_A	domain integrated dust emission, deposition, and advection [$\mathrm{M\,T^{-1}}$]
D	viscous sublayer thickness; δ in (*Klose and Shao*, 2012); [m]
F	dust emission flux [$\mu\mathrm{g\,m^{-2}\,s^{-1}}$]
G	geometric coefficient for capillary cohesive force []
H	heat flux [$\mathrm{W\,m^{-2}}$]
L	Obukhov length [m]
M	distribution mean
N	particle number concentration [$\mathrm{m^{-3}}$]
P	probability
Q	saltation flux [$\mu\mathrm{g\,m^{-1}\,s^{-1}}$]
R_i	Richardson number
T	water surface tension [$\mathrm{N\,m^{-1}}$]
T_p	particle response time [s]
U_r	particle-to-fluid relative velocity [$\mathrm{m\,s^{-1}}$]
ΔP	pressure difference between soil water and atmosphere [$\mathrm{N\,m^{-2}}$]
Γ	gamma function
Θ	potential temperature [K]
α	scale parameter in Weibull distributions
α_N, α_{N0}	CTDE model parameter [$\mathrm{m^{-2}}$]
β	shape parameter in Weibull distributions
δ	differential; viscous sublayer thickness in (*Klose and Shao*, 2012) and *Li et al.* (2014)

δD	domain integrated dust load change with time [$\mathrm{M\,T^{-1}}$]
$\delta\,(\,)$	delta function
η	vegetation cover fraction
η_i	particle-size fraction
κ	von Kármán constant
μ	mean value
ν	kinematic viscosity [$\mathrm{m^2\,s^{-1}}$]
ψ_s	saturation capillary pressure head [m]
ρ	air density [$\mathrm{kg\,m^{-3}}$]
ρ_p	particle density [$\mathrm{kg\,m^{-3}}$]
ρ_w	water density [$\mathrm{kg\,m^{-3}}$]
σ	standard deviation
τ_R	Reynolds shear stress [$\mathrm{N\,m^{-2}}$]
τ_f	instantaneous momentum flux [$\mathrm{N\,m^{-2}}$]
τ_c	canopy-surface drag [$\mathrm{N\,m^{-2}}$]
τ_g	grid-scale contribution to τ_f [$\mathrm{N\,m^{-2}}$]
τ_r	pressure drag [$\mathrm{N\,m^{-2}}$]
τ_{sg}	sub-grid contribution to τ_f [$\mathrm{N\,m^{-2}}$]
τ_s	ground surface drag [$\mathrm{N\,m^{-2}}$]
θ	volumetric soil moisture [$\mathrm{m^3\,m^{-3}}$]
θ_r	air-dry soil moisture [$\mathrm{m^3\,m^{-3}}$]
θ_s	saturation soil moisture [$\mathrm{m^3\,m^{-3}}$]
ϑ	coefficient for mean cohesive force [$\mathrm{kg\,s^{-2}}$]
ξ	particle resting angle [°]
d	particle diameter [μm]
d_i	dust particle diameter [μm]
d_s	saltation particle diameter [μm]
f	aerodynamic lifting force [N]
f_g	gravity force [N]
f_i	inter-particle cohesive force; F_i in *Klose and Shao* (2012) [10^{-8} N]
f_t	retarding force [N]
f_{ic}	capillary cohesive force [N]
g	gravitational acceleration [$\mathrm{m\,s^{-2}}$]
m_p	particle mass [kg]
n	particle number flux [$\mathrm{m^{-2}\,s^{-1}}$]
$p, p\,(\,)$	probability density function

p_A	area particle-size distribution
p_M	mass particle-size distribution
r^2	coefficient of determination
u, v, w	wind components in x-, y-, and z-direction [$\mathrm{m\,s^{-1}}$]
u_*	friction velocity [$\mathrm{m\,s^{-1}}$]
u_g, v_g, w_g	grid-scale wind components in x-, y-, and z-direction [$\mathrm{m\,s^{-1}}$]
u_{*t}	threshold friction velocity [$\mathrm{m\,s^{-1}}$]
u_{sg}, v_{sg}, w_{sg}	sub-grid wind components in x-, y-, and z-direction [$\mathrm{m\,s^{-1}}$]
w	weight of lognormal distribution for psd
w_*	convective scaling velocity [$\mathrm{m\,s^{-1}}$]
w_m	combined scaling velocity [$\mathrm{m\,s^{-1}}$]
w_p	particle velocity [$\mathrm{m\,s^{-1}}$]
w_t	particle terminal velocity [$\mathrm{m\,s^{-1}}$]
z	height [m]
z_0	roughness length [m]
z_i	inversion layer height [m]
$\mathrm{W_1}$, $\mathrm{W_2}$	past weather, 3 and 6 h
ww	present weather code
$\overline{(\,)}$	mean value
$(\,)'$	turbulent component
$\lvert(\,)\rvert$	absolute value

Acknowledgments

First of all, I wish to express my gratitude to Yaping Shao, who has been an excellent supervisor for me over many years. He introduced me to aeolian research and its fascination, and he decisively promoted my scientific development. Also, I wish to thank Ina Tegen for agreeing to review this thesis, Frank Schäbitz for chairing my thesis defense and Sabine Lennartz-Sassinek for acting as observer/recorder during the latter.

I am grateful to Nicholas Webb and Karsten Haustein for carefully proofreading my thesis. Additional thanks go to the former for providing me with valuable suggestions and insider information on Australian dust. I wish to thank Stefan Borowski and the Regional Computing Center Cologne (RRZK) for computing time and support to conduct the model runs presented in this thesis. I also thank Harry Butler for making the dust source data and psd assignment available for use in the simulations. Further thanks go to Philipp Schlüter for his assistance in fitting the psd coefficients. I appreciate Christian Willmes' support in getting a doi and license for my dust-LES video.

I am also grateful to my friends and colleagues from the Institute for Geophysics and Meteorology in Cologne. Many of them helped me in various ways during the last years, e.g. Robert Schuster solved some of my programming problems, Sven Ulbrich and Patrick Ludwig supported me with regard to computer network and system issues, and Melanie Karremann had the same thesis deadline and shared my concerns.

My heartfelt thanks go to my family, namely Brigitte, Elke, Marc, and Emil, who are always there for me and help me putting things into the right perspective. This is also in memory to my father Eberhard who would have been very proud of me.

Beitrag zu den Publikationen

In allen in der Dissertationsschrift enthaltenen Publikationen habe ich die Hauptrolle bzw. eine wichtige Rolle übernommen. Die Grundidee zum hier beschriebenen stochastischen Staubemissionsschema entstand im Rahmen meiner Diplomarbeit unter Betreuung von Prof. Y. Shao. Der Artikel *Klose and Shao* (2012) basiert darauf, die Inhalte wurden allerdings während der Promotionszeit überarbeitet sowie erweitert. Die theoretischen Grundlagen in *Klose and Shao* (2012, 2013) und *Klose et al.* (2014a) wurden jeweils unter Betreuung von Prof. Y. Shao entwickelt, von mir weiter ausgearbeitet und numerisch umgesetzt. Die Simulationen und Auswertungen wurden ebenfalls von mir durchgeführt. Mein Beitrag zur Arbeit von *Li et al.* (2014) bestand im Vorbereiten und Zurverfügungstellen des genutzten Staubmodells sowie in der Unterstützung bei der Planung, Durchführung und Auswertung der Simulationen.

Erklärung

Ich versichere, dass ich die von mir vorgelegte Dissertation selbstständig angefertigt, die benutzten Quellen und Hilfsmittel vollständig angegeben und die Stellen der Arbeit – einschließlich Tabellen, Karten und Abbildungen – , die anderen Werken im Wortlaut oder dem Sinn nach entnommen sind, in jedem Einzelfall als Entlehnung kenntlich gemacht habe; dass diese Dissertation noch keiner anderen Fakultät oder Universität zur Prüfung vorgelegen hat; dass sie – abgesehen von unten angegebenen Teilpublikationen – noch nicht veröffentlicht worden ist, sowie, dass ich eine solche Veröffentlichung vor Abschluss des Promotionsverfahrens nicht vornehmen werde. Die Bestimmungen der Promotionsordnung sind mir bekannt. Die von mir vorgelegte Dissertation ist von Prof. Dr. Yaping Shao betreut worden.

Nachfolgend genannte Teilpublikationen liegen vor:

Klose, M., and Y. Shao (2012), Stochastic parameterization of dust emission and application to convective atmospheric conditions, *Atmos. Chem. Phys.*, *12*(12), 7309–7320, doi: 10.5194/acp-12-7309-2012

Klose, M., and Y. Shao (2013), Large-eddy simulation of turbulent dust emission, *Aeolian Research*, *8*, 49–58, doi: 10.1016/j.aeolia.2012.10.010

Klose, M., Y. Shao, X. L. Li, H. S. Zhang, M. Ishizuka, M. Mikami, and J. F. Leys (2014a), Further development of a parameterization for convective turbulent dust emission and evaluation based on field observations, *J. Geophys. Res. Atmos.*, *119*, 10,441–10,457, doi: 10.1002/2014JD021688

Li, X. L., M. Klose, Y. Shao, and H. S. Zhang (2014), Convective Turbulent Dust Emission (CTDE) observed over Horqin Sandy Land area and validation of a CTDE scheme, *J. Geophys. Res. Atmos.*, *119*, 9980–9992, doi: 10.1002/2014JD021572

Köln, im August 2014

(Martina Ruth Klose)